Molecular Beam Epitaxy of Wide Bandgap Al(Ga)N and h-BN for Deep-Ultraviolet Optoelectronics

by

David Laleyan

A dissertation submitted in partial fulfillment
of the requirements for the degree of
Doctor of Philosophy
(Electrical and Computer Engineering)
in the University of Michigan
2020

Doctoral Committee:

Professor Zetian Mi, Chair
Professor Pallab K. Bhattacharya
Assistant Professor Parag B. Deotare
Associate Professor Emmanouil Kioupakis

David Laleyan

dlaleyan@umich.edu

ORCID iD: 0000-0002-3251-6242

© David Laleyan 2020

Dedication

To my parents, for all their love and support.

Acknowledgements

I would like to first and foremost thank my advisor, Prof. Zetian Mi, for all his wisdom, support and guidance from the first day I walked into his office as an undergraduate student back in 2013 looking for a summer research position. I am deeply grateful for the countless opportunities he provided throughout the years to ensure the success of my graduate studies and professional development. His dedication as a mentor has motivated and encouraged me to persevere and develop an ever-growing passion for our field of research. The many insightful discussions in his office and labs have been the inspiration and basis for the work presented in this thesis. It truly has been an exciting adventure, which would not have been possible without him.

I am thankful for the members of my doctoral committee, Prof. Pallab Bhattacharya, Prof. Parag Deotare and Prof. Manos Kioupakis, for their careful review and valuable suggestions for the work in this thesis. It has been a pleasure having them as research collaborators.

Group members who have been crucial mentors early on include Prof. Songrui Zhao, Prof. Hieu Pham Trung Nguyen, Dr. Shaofei Zhang, Dr. Binh Huy Le, Dr. Ashfiqua T. Connie and Dr. Faqrul A. Chowdhury. I am also grateful for past and present group members for sharing the daily joys and frustrations of research with me. They include Dr. Xianhe Liu, Dr. Srinivas Vanka, Dr. Yongjie Wang, Dr. Renjie Wang, Dr. Nhung Hong Tran, Dr. Yong-Ho Ra, Dr. Ping Wang, Dr. Yi Sun, Mr. Yuanpeng Wu, Ms. Roksana T. Rashid, Mr. Ayush Pandey, Mr. Walter Jin Shin, Mr. Eric T. Reid, Mr. Kishwar Mashooq and Mr. Nick Pant. Many of them have in the process become good friends. I hope I am not forgetting anyone.

This work would have also not been possible without the valuable contributions of collaborators. They include Dr. Thomas Frost, Dr. Arnab S. Hazari and Mr. Anthony F. Aiello from Prof. Pallab Bhattacharya's research group, especially in facilitating our move to the University of Michigan in 2016, Prof. Thomas Szkopek and Prof. Hong Guo from McGill University, Dr. Steffi Y. Woo and Dr. Natalia Fernández-Delgado previously from Prof. Gianluigi Botton's research group at McMaster University, Dr. Kelsey A. Mengle formerly in Prof. Manos Kioupakis's research group at the University of Michigan, and Dr. Mo Soltani from Raytheon BBN Technologies.

The experimental work presented in this thesis was performed in several state-of-the-art facilities. They include the Lurie Nanofabrication Facility (LNF) and X-Ray Micro-Analysis Laboratory (XMAL) at the University of Michigan, the McGill Nanotools Microfab (MNM), Facility for Electron Microscopy Research (FEMR), Chemistry Characterization Facility (CCF) and Institute for Advanced Materials (MIAM) at McGill University, and the Laboratoire de caractérisation des matériaux (LCM) at the University of Montreal. I am grateful for all the staff members who provided training and support at these facilities, with particular recognition to Dr. Sandrine Martin, Dr. Pilar Herrera-Fierro, Dr. Lino Eugene, Dr. Lihong Shang, Dr. Samir Elouatik and Ms. Patricia Moraille for their mentorship that extended beyond their guidance in using specific tools.

I would like to highlight the remarkably hard work of Mr. Dennis Schweiger in managing the infrastructure that supports our molecular beam epitaxy (MBE) labs. It has been a wonderful learning experience working with the team at Veeco Instruments Inc. for the configuration, installation and operation of our MBE systems. Many of the practical aspects I learned along the way are from the teachings and extensive experience of Mr. Dan Day, their senior field service

engineer, who became a cherished friend in the process. I am also lucky to have had the opportunity to work and interact with Dr. Mark O'Steen, their impressively knowledgeable and insightful staff scientist.

The funding sources for the work in this thesis include the National Science Foundation (NSF), Army Research Office (ARO), Natural Sciences and Engineering Research Council of Canada (NSERC) and Fonds de recherche du Québec – Nature et technologies (FRQNT). Internal sources of funding as part of my graduate student research assistantship and various travel grants include the Rackham Graduate School and the Electrical Engineering and Computer Science (EECS) Department, as well as support from College of Engineering at the University of Michigan. I must thank the many staff members within the EECS department, including the program coordinators, research managers, administrative assistants, shipping dock attendants and purchasing associates.

Finally, I am grateful to my family and friends for their encouragement, especially my parents, Zaven and Knar, for all their love and support.

Table of Contents

Dedication .... **ii**

Acknowledgements .... **iii**

List of Tables .... **x**

List of Figures .... **xi**

List of Appendices .... **xxiii**

Abstract .... **xxiv**

Chapter 1 Introduction **1**

1.1 Optoelectronic Devices 1

1.2 Bandgaps and Heterojunctions 8

1.3 III-Nitride Materials 12

1.4 Brief History of III-Nitride LEDs 22

1.5 III-Nitride Nanowires 24

1.6 Deep-Ultraviolet Light Emitters 25

1.7 Current Approaches for Growing Wide Bandgap III-Nitrides 38

1.8 Dissertation Overview 41

Chapter 2 Methods **43**

2.1 Overview 43

2.2 Molecular Beam Epitaxy 43

2.3 In Situ Characterization 49

2.4 Structural Characterization 51

2.5 Optical Characterization 54

2.6 Electrical Characterization 57

Chapter 3 Molecular Beam Epitaxy and Characterization of $Al_{0.6}Ga_{0.4}N$ Epilayers 59

3.1 Author Contributions and Copyright Disclaimer 59

3.2 Background and Motivation 59

3.3 Growth of Al-Rich AlGaN Epilayers 62

3.4 Structural Characterization of the AlGaN Epilayers 64

3.5 Optical Characterization of the AlGaN Epilayers 68

3.6 Conclusion 71

Chapter 4 Strain-Free Ultrathin AlN Epilayers Grown Directly on Sapphire by Molecular Beam Epitaxy 73

4.1 Author Contributions and Copyright Disclaimer 73

4.2 Background and Motivation 74

4.3 MBE Growth of AlN Epilayers on Sapphire 75

4.4 Structural Characterization of the Ultrathin AlN Films on Sapphire 78

4.5 Optical Characterization of the Ultrathin AlN Films on Sapphire 82

4.6 Thicker AlN Epilayers on Sapphire 83

4.7 Conclusion 84

Chapter 5 AlN/h-BN Heterostructures for Mg Dopant-Free Deep Ultraviolet Photonics ... 85

5.1 Author Contributions and Copyright Disclaimer 85

5.2 Background and Motivation 86

5.3 Growth of AlN/h-BN Heterojunction Nanowire LEDs 87

5.4 Characterization of the AlN/h-BN Nanowires 89

5.5 Mg Dopant-Free AlN/h-BN Nanowire Light-Emitting Diodes 92

5.6 Conclusion 96

Chapter 6 Effect of Growth Temperature on the Structural and Optical Properties of Few-Layer Hexagonal Boron Nitride by Molecular Beam Epitaxy 98

6.1 Author Contributions and Copyright Disclaimer 98

6.2 Introduction 99

6.3 Growth and Characterization of Few-Layer h-BN 100

6.4 Optical Properties of Few-Layer h-BN Grown by MBE 104

6.5 Theory and Discussion 106

6.6 Conclusion 108

Chapter 7 Hexagonal Boron Nitride Deep Ultraviolet Excitonic Light Emitting Diodes .. 109

7.1 Author Contributions and Copyright Disclaimer 109

7.2 Background and Motivation 109

7.3 Hexagonal Boron Nitride LED Structure 110

7.4 Growth of the LED Structure 111

7.5 Optical Properties of the h-BN 112

7.6 h-BN LED Demonstration 113

7.7 Conclusion 114

Chapter 8 Summary and Future Work 115

8.1 Summary 115

8.2 Further Improvements in the MBE Growth of Al(Ga)N Epilayers 115

8.3 Doping of MBE-Grown AlN Epilayers 117

8.4 Elucidating the Luminescence and Excitonic Properties of h-BN 118

8.5 Towards Wafer-Scale Monolayer h-BN 119

8.6 Hybrid h-BN/Al(Ga)N Heterostructures 120

8.7 Boron Containing III-Nitride Alloys 121

Appendices 125

Bibliography 147

List of Tables

Table 2.1 – Summary of gas molecule properties at various pressure levels, from atmospheric pressure to UHV. (Source: Agilent Technologies) 44

Table 3.1 - Fitted model parameters used in the Cauchy relationship to obtain the refractive index versus wavelength curves of AlGaN and AlN. 69

Table A.1 – Table of calculated $Al_xGa_{1-x}N$ bandgap energy (E_g), PL wavelength and XRD 2Theta-Omega angle for various compositions........ 130

Table A.2 – List of components for Fig. A.3. 132

Table A.3 – List of components for Fig. A.4. 134

List of Figures

Figure 1.1 – Cross-sectional view of a thin film LED. (Source: Wikipedia.org) 2

Figure 1.2 – Simplified LED structure and band diagram. (Source: Wikipedia.org) 3

Figure 1.3 – I-V characteristics of an LED. (Source: Wikipedia.org) 3

Figure 1.4 – Emission spectrum of a phosphor-coated white LED. (Source: Wikipedia.org) 5

Figure 1.5 – Fabrication steps of an LED. (Source: Yole Développement) 7

Figure 1.6 – Schematic of recombination in (left) direct and (right) indirect bandgap semiconductors. (Source: APS.org) 10

Figure 1.7 – Flat-band schematic of the three types of heterojunction interfaces. (Source: Wikipedia.org) 11

Figure 1.8 – Portion of the periodic table showing group-III and group-V materials that are compounded to form III-V semiconductors. (Source: hypnocube.com) 12

Figure 1.9 – Wurtzite crystal structure schematic. (Source: Wikipedia.org) 13

Figure 1.10 – Crystal structure schematic of the polymorphs of BN. (Source: [14]) 15

Figure 1.11 – CL spectrum of h-BN showing a luminescence peak at 215 nm. (Source: [19]) ... 17

Figure 1.12 - Low-temperature PL spectrum of h-BN, highlighting the various phonon-assisted transitions for every observed luminescence peak at around 215 nm. These include acoustic and optical phonons in the longitudinal and transverse directions, as well as an indirect exciton (marked by iX). (Source: [20]) 18

Figure 1.13 – Low-temperature PL spectrum of h-BN, with various S and D series exciton transitions identified with arrows. (Source: [21]) 18

Figure 1.14 – Proposed energy band diagram of h-BN based on PL and photocurrent excitation spectroscopy measurements. The bandgap, and free and bound exciton binding energies are marked as E_g, E_X and E_{BX}, respectively. (Source: [22]) 19

Figure 1.15 – Calculated band structure of varying layers of h-BN. (Source: [24]) 19

Figure 1.16 – Calculated band structures of h-BN showing defect-induced transitions due to carbon impurities, and B, N and BN vacancies obtained from a theoretical study. (Source: [25]).......... 20

Figure 1.17 – Lattice matching between wurtzite AlN and h-BN, showing a 5/4 alignment at the interface. (Source: [16]) 21

Figure 1.18 – (a) Schematic of the first AlN LED device structure. (b) EL spectrum of this AlN LED and an equivalent MIS structure. (c) I-V characteristics of these devices. (Source: [42]) .. 23

Figure 1.19 – (a) Schematic of the AlN nanowire LED on Si substrate. (b) EL spectrum and current dependence of the output power of the LED device. (c) I-V characteristics of the LED device. (Source: [44]) 24

Figure 1.20 – Applications requiring deep-UV light sources. (Source: courtesy of Nick Pant, University of Michigan)... 25

Figure 1.21 – Status of UV LEDs in terms of emission wavelength and quantum efficiency. (Source: [54]) 27

Figure 1.22 – Schematic of a commonly used design for UV LEDs. (Source: [5]) 28

Figure 1.23 – Cross-sectional microscope image of AlGaN grown on SiC, highlighting the dislocations due to lattice mismatch. (Source: [57])... 29

Figure 1.24 - Reduction of the radiative efficiency with an increase in etch pit density acting as dislocations. (Source: [3]) 30

Figure 1.25 – Band structure of wurtzite GaN, showing the splitting of the valence band into the HH, LH and CH bands. (Source: [6]) 31

Figure 1.26 – Degree of polarization P as a function of Al content in AlGaN alloys, showing a transition from predominantly TE to TM polarized light with increasing Al composition. A decrease in P is indicative of stronger TM polarization. (Source: [63]) 32

Figure 1.27 – Schematic of the conduction band of an LED device, highlighting the overflow of injected electrons, and the addition of an electron blocking layer. (Source: [5]) 33

Figure 1.28 – Mg-dopant activation energy in p-doped AlGaN with varying Al composition. (Source: redrawn based on [69]) 34

Figure 1.29 – (a) SEM image of free-standing AlN nanowires on Si substrate. (Source: [44]) (b) TEM image focusing on a single AlN nanowire, with the arrow showing the growth direction. (Source: [44], [70]) 35

Figure 1.30 – PL spectra of AlGaN nanowire samples grown using different substrate temperatures. (Source: [74]) 36

Figure 1.31 – Schematic of an AlGaN quasi-film structure formed by coalescing nanowires grown by selective area epitaxy. It is found that the dislocations from the lattice mismatch can be terminated with the lateral broadening and coalescence of the nanowires. (Source: [79]) 37

Figure 1.32 – Schematic of the growth steps of AlN on sapphire by MOCVD in order to achieve lower dislocation densities. (Source: [58]) 39

Figure 1.33 – Schematic of the various techniques used for the synthesis of h-BN monolayers and/or thin films. (Source: constructed using figures from [91]–[93]) 40

Figure 1.34 – Flat-band energy diagram of an AlN and h-BN heterojunction. (Source: [16]) 40

Figure 2.1 – Illustration of the various adatom behaviors and surface interactions during the growth process. (Source: Technische Universität Kaiserslautern) ... 45

Figure 2.2 – (a) Schematic of the growth chamber of an MBE system. (Source: Wikipedia.org) (b) Schematic of an effusion source for MBE. (Source: Veeco Instruments Inc.) (c) Schematic of an e-beam evaporator. (Source: University of Cambridge) ... 46

Figure 2.3 – Photographs of the Veeco GEN 930 (left) and GENxplor (right) systems used to conduct the sample growths as part of this thesis. ... 47

Figure 2.4 – Photograph of a UV-optimized PL setup. The labels identify the major components. A number of optical components such as mirrors and lenses are used to direct the optical path. 55

Figure 2.5 – Schematic of the setup to experimentally measure polarization-resolving PL. (Source: [125]) ... 56

Figure 3.1 – (a) Photograph of the sustained streaky RHEED pattern during AlGaN growth. (b) 2Theta-Omega XRD scan of the $Al_{0.6}Ga_{0.4}N$ sample, showing peaks at 35.4° and 36°. The latter corresponds to the AlN template peak. ... 65

Figure 3.2 – STEM images of the sample cross-section, with the yellow arrow defining the growth direction in every case. (a) STEM-BF image at 200k× magnification, displaying the AlN template, AlN buffer and AlGaN epilayer regions, as well as the threading dislocations originating from the template and propagating into the grown film. Labeled on the figure are regions of interest highlighting the bending of the dislocations reaching the AlGaN superlattice (1), convergence of dislocations leading to their annihilation (2), termination of propagating dislocations partly through the AlGaN (3), and grouping of several threading dislocations (4). Shown in the inset is an EDS line scan of the AlGaN superlattice, showing an Al/Ga compositional variation at the

nanometer scale and under similar N presence. (b) STEM-DF image at 1.2M× magnification showing the periodic superlattice formed in the AlGaN film (boxed in blue in (a)) during growth. The periodic spacing is of ~7 nm. (c) High-magnification HAADF image (30M×) displaying the atomic-resolution stack interface of the superlattice (boxed in red in (b)). From the crystalline stacking, the interruptions during growth lead to sub-nanometer compositional variations in the AlGaN film. 66

Figure 3.3 – SEM images of the sample surface taken at magnifications of 700× (a) and 200k× (b). (c) AFM height image of the sample surface of 1 μm^2. The inset above it is a section analysis of the terraces (identified by the blue line) showing height variations corresponding to atomic steps. 68

Figure 3.4 – Refractive index versus wavelength curves for $Al_{0.6}Ga_{0.4}N$ (in solid blue) and AlN (in dashed black) obtained by spectroscopic ellipsometry. 70

Figure 3.5 – (a) Variable excitation power PL spectra of the $Al_{0.6}Ga_{0.4}N$ sample at room temperature, showing a single dominant peak centered at ~284 nm. (b) Temperature dependence of the integrated PL intensity (normalized to 1). The inset shows the changes with temperature. 71

Figure 4.1 – (a) Schematic of the growth sequence of AlN on sapphire substrate: (I) initial AlN buffer growth using a MEE process, (II) high-temperature annealing of the grown ultrathin film, (III) repeated growth and annealing steps to improve the buffer layer quality, and (IV) epitaxy of high-quality AlN epilayers using an interruption-assisted process. (b) Photographs of the RHEED patterns observed during growth: (I) spotty and segmented pattern during the initial stage of growth, (II) streakier pattern during the buffer stages, (III) broadened and brighter pattern during the annealing stages, and (IV) narrow streaky pattern during the epilayer growth stage. 78

Figure 4.2 – (a) STEM cross-section image of the ~100-nm-thick AlN sample on sapphire substrate. The yellow arrow indicates the growth direction. (b) High-magnification STEM image of the AlN and sapphire interface. The red arrow highlights an atomic step height mismatch at the interface. (c) ε_{xx} strain map (in the direction contained in the growth plane) obtained during the analysis, with the strain values (taking sapphire as the zero reference) in the included color scale bar. (d) Strain profile taken along the map in (c) denoted by the blue arrow. 80

Figure 4.3 – XRD rocking curves (in red) of the (a) symmetrical (002) and (b) asymmetrical (102) reflections of the ~100-nm-thick AlN layer grown on sapphire substrate. The dotted blue curves are the Lorentz fitting of each curve, used to obtain a FWHM of 126 arcsec and 1387 arcsec for (a) and (b), respectively. (c) Comparison of AlN XRD (002) rocking curve linewidths reported in literature and that of this work (in red). 81

Figure 4.4 – (a) Normalized temperature dependence of the integrated PL intensity of the ~100-nm-thick AlN sample. The inset shows the emission spectra under constant excitation power at various temperatures. (b) Comparison of the PL intensity of the same sample (in red) and a commercial AlN epitaxial template that is ~10 times thicker (in black). The inset shows the estimated IQE of ~30% of the sample from this study. 83

Figure 4.5 – (a) Low-magnification SEM image of the ~1-µm-thick sample surface. The intentional scratch mark on the top left corner was used to properly focus on the sample surface. An optical image is included as the inset. (b) High-magnification AFM image of the sample surface topology. (c) PL spectrum of the sample at room (in red) and cryogenic (in blue) temperatures. (d) Comparison of the PL intensity of the same sample (in red) and the commercial AlN epitaxial template from Fig. 4.4(b) (in black).. 84

Figure 5.1 – MBE growth of the AlN/h-BN nanowire array. (a) Schematic of the AlN nanowires (n-doped in green, undoped in blue) grown on a GaN nanowire template (in yellow) on a Si substrate (in gray), with a thin layer of h-BN on top (in red). (b) SEM image of such an as-grown nanowire array. 89

Figure 5.2 – Structural characterization of a single nanowire. (a) STEM-BF and (b) HAADF images of an AlN/h-BN nanowire, highlighting the GaN template, AlN, and h-BN segments. (c) High-magnification HAADF image of the AlN/h-BN region, and inset (boxed in red) detailed views of the crystalline lattice within the h-BN layer (circled in yellow). Additional inset shows a bandpass filtered image of the region boxed in orange to emphasize contrast in the crystalline layers. (d) Detailed view of the h-BN layer from another area (boxed in green in b) in the same nanowire. (e) STEM-EELS elemental map of the region in c, extracted from the Al $L_{2,3}$ and B K-edges, showing conformal h-BN coverage on the top and sidewall facets of the AlN segment. (f) Core-loss EELS spectra of the N K, and B K-shell ionizations from the h-BN layer showing both π^* and σ^* components labeled that correspond to sp^2 hybridization in hexagonal BN. 91

Figure 5.3 – PL and optical properties of the nanowires. (a) Room-temperature PL spectrum of the AlN/h-BN nanowire sample at various excitation powers. (b) Estimated IQE at these excitation powers. Inset shows the PL spectrum centered at 210 nm at 20 K (in solid red) and 300 K (in dashed black). 92

Figure 5.4 – Electrically injected AlN/h-BN nanowire LEDs. (a) Schematic of the fabricated LED structure, which includes thin Ni/Au p-metal contacts and the heavily n-doped Si substrate as the n-contact. (b) I-V curve of a 300 μm × 300 μm LED device at room temperature, with a photograph of said device as the inset, which is characteristic of a diode rectification behavior. (c) Variation

of Hole mobility and concentration of an equivalent h-BN layer grown on a SiO_x/Si substrate as a function of temperature. 94

Figure 5.5 – EL properties of the AlN/h-BN nanowire LED. (a) EL spectrum of this LED device at ~210 nm for various injection currents, measured at room temperature. (b) Light output as a function of injection current, showing a near-linear increase and saturation at higher current densities. The black squares show the same measurement results for an equivalent AlN p-i-n homojunction LED. The black dashed line is a linear extrapolation of the output power at higher current densities. (c) Relative EQE as a function of the injection current density for this LED device, showing an increase up to a maximum efficiency, followed by a droop at higher injection currents. 96

Figure 6.1 – (a)-(c) Snapshots of RHEED patterns during the growth of h-BN at 500 °C (Sample A), 1200 °C (Sample B) and 1300 °C (Sample C), respectively. The RHEED pattern transitions from polycrystalline rings to continuous streaks with samples growing at higher temperature. (d)-(f) SEM images of the same three sample surfaces. 102

Figure 6.2 – XPS high-resolution spectrum of B 1s (a) and N 1s (b) for the h-BN Sample C. Micro-Raman spectrum of: (c) Sample A (in solid blue) as compared to the bare Ni substrate (in dotted black). The h-BN sample shows peaks at ~1365 and 1600 cm^{-1}, corresponding to theoretical frequencies of 1394 (Raman-active; E_{2g}) and 1627 cm^{-1} (IR-active LO mode; E_{1u}); (d) Sample C, showing a strong and narrow Raman peak at 1360 cm^{-1} (FWHM of 13 cm^{-1}). A secondary weak peak at 800 cm^{-1} is also present. Symmetry-breaking at the surface could turn the theoretically calculated mode at 747 (IR-active; A_{2u}) or 818 cm^{-1} (IR- and Raman-forbidden; B_{1g}) into a Raman-active mode. 104

Figure 6.3 – Room-temperature PL spectra of three h-BN Samples A (in blue), B (in green) and C (in red). As growth temperature is increased, the short-wavelength emission is enhanced, and the longer-wavelength defect emissions are suppressed. The inset shows the PL spectrum measured at cryogenic temperature of Sample C. 105

Figure 6.4 – Schematic band structure of BN near the band extrema. Although the bandgap is indirect, the phonon-assisted matrix element S is similarly strong to direct optical transition, and hence BN luminesces as a direct-gap material. 107

Figure 6.5 – (a) Room-temperature PL emission of Sample C (in red) as compared to a commercial AlN epilayer template on sapphire (in black). (b) Integrated PL intensity of both samples measured at various laser excitation powers. 108

Figure 7.1 – Schematic of the LED structure consisting of a p-i-n AlN stack on h-BN on Ni substrate. The substrate acts as the p-contact, while thin Ti/Au metal pads act as n-contacts on top of the n-AlGaN contact layer. 111

Figure 7.2 – SEM images of the h-BN/Ni surface before (top) and after (bottom) the AlN regrowth. The h-BN features remain noticeable and unchanged under relatively thick AlN. 112

Figure 7.3 – (a) Integrated PL intensity at ~220 nm of h-BN/Ni at various excitation powers at cryogenic and room temperatures. (b) Estimated IQE of h-BN/Ni of ~50% at various excitation powers. (c) Polarization-resolving PL spectra of h-BN/Ni, showing predominantly TE polarized light being emitted. 113

Figure 7.4 – (a) I-V curve of a 1 mm × 1 mm LED device, with a photograph of the device being probed as the inset. (b) Room-temperature EL spectrum of the device (in red) in the deep UV wavelength range, as compared to the low-temperature PL emission peaks (in blue) from a h-BN/Ni sample 114

Figure 8.1 – PL spectra of AlGaN epilayer samples grown with (in red) and without (in black) in situ annealing in the MBE chamber. (Source: courtesy of Ayush Pandey, University of Michigan) 116

Figure 8.2 – (a) XRD (102) rocking curves of AlN films annealed at different temperatures, showing a reduction in linewidth compared to the as-grown sample. (b) Normalized PL spectra of AlN annealed at different temperatures, showing stronger intensities with increasing annealing temperature. (Source: courtesy of Eric T. Reid, University of Michigan) 117

Figure 8.3 – EL spectrum of the h-BN LED presented in Chapter 7. Circled in green is the emission range that is consistent with the luminescence properties of h-BN. The red arrows highlight additional lower-energy peaks previously unseen from luminescence of h-BN or AlN. 118

Figure 8.4 – (a) Flat-band schematic of the h-BN/AlN interface, showing the formation of an indirect exciton between an electron in h-BN and hole in AlN. (b) Illustration of possible polarons in the h-BN lattice from phonon-exciton coupling. 119

Figure 8.5 – SEM image of h-BN on Ni grown at unintendedly high temperature, showing a spread of the nucleation domains and more complete surface coverage. 120

Figure 8.6 – SEM images at low (left) and high (right) magnifications of the mechanically delaminated material grown on Ni. 121

Figure 8.7 – (a) Schematic of the layer stacking of the grown samples (not to scale). (b-c) Top: RHEED pattern during the growth of the topmost layer; bottom: SEM surface image of the samples post-growth for B compositions of (b) 0% (AlGaN-only) and (c) ~1%. 123

Figure 8.8 – (a) XPS survey scan of the sample with a B composition ~1%. The inset shows the high-resolution scan of the B 1s peak with a binding energy of ~195 eV. (Source: courtesy of Ping Wang, University of Michigan) (b) XRD scans around the (0002) peak for the AlGaN and BAlGaN

samples. The common peak at 36° corresponds to the AlN template the samples were grown on. (Source: courtesy of Ayush Pandey, University of Michigan) (c) Room-temperature PL spectrum of the MBE-grown BAlGaN sample with ~1% B composition. The peak at ~240 nm is consistent with that of the underlying AlGaN, while the peak ~300 nm emerges from the BAlGaN layer. (Source: courtesy of Ayush Pandey, University of Michigan) 123

Figure A.1 – Illustration of the electromagnetic spectrum. (Source: Wikipedia.org) 126

Figure A.2 – Bandgap and Lattice Constant Relation of the III-Nitride Materials. (Source: [3]) 129

Figure A.3 – Schematic of the PL setup for UV measurements. Table A.2 lists the components. For temperature-dependent PL, the sample needs to be loaded into the cryostat, pumped down and then cooled down using a closed-loop helium compressor and temperature controller. 131

Figure A.4 – Schematic of the EL setup for UV LED measurements. Table A.3 lists the components. 133

Figure A.5 – (a) Schematic of the AlN/h-BN nanowire heterostructure, with the growth direction denoted by the black arrow. (b) Flat energy band diagram of this heterostructure, highlighting the band alignment between the different layers along the growth direction denoted by the black arrow. E_c, E_v, E_F and E_g are the conduction band minima, valence band maxima, Fermi level and bandgap energies, respectively. 135

Figure A.6 – Energy diagram of the optical processes observed from the impurity emission lines of the h-BN reported in this study, which match the energy levels theoretically attributed to boron vacancies. Eg is the bandgap energy, and CB and VB are the conduction and valence band edges, respectively. 137

Figure A.7 – Low-loss EELS spectrum from the BN layer in the AlN/h-BN heterostructure ... 137

Figure A.8 – (a) STEM-HAADF image of the h-BN layer grown on a SiO_x/Si(001) substrate. (b) EELS elemental mapping of the distribution of B and Si at the h-BN/SiO_x interface using the B K and Si $L_{2,3}$-edges, respectively. (c) Core-loss EELS spectra of the B K-edge from the BN layer showing both π^* and σ^* components, confirming h-BN. 138

Figure A.9 – (a) Room-temperature PL spectrum centered at 210 nm of the AlN/h-BN nanowire sample (in solid red) and an identical AlN nanowire sample without h-BN (in dashed black). (b) Extended-range PL spectra highlighting the band-edge and defect-related emissions of two AlN/h-BN nanowire samples with h-BN growth temperatures of 400 °C (in blue) and 800 °C (in red). The spectrum of an equivalent AlN nanowire sample without h-BN is included (in black) for comparison. (c) PL spectrum of h-BN grown on a SiO_x/Si(001) substrate, showing the dominance of boron-vacancy related transition. 139

Figure A.10 – I-V curve of the same device shown in Fig. 5.4(b) in semi-log scale. 140

Figure A.11 – Absorbance spectrum of a bare sapphire substrate (in dashed black), h-BN on sapphire substrate (in solid blue) and GaN on sapphire substrate of equivalent thickness (in solid red). 141

Figure A.12 – Transmittance curves of GaN and h-BN derived from the absorbance spectra in Fig. A.11 using Beer's law and subtracting the absorbance spectrum of the bare sapphire substrate as a baseline. 141

List of Appendices

Appendix A Illustration of the Electromagnetic Spectrum 126

Appendix B Fabrication Steps of UV LEDs 127

Appendix C Bandgap and Lattice Constant Relation of the III-Nitride Materials 129

Appendix D Useful Lookup Table of $Al_xGa_{1-x}N$ Properties 130

Appendix E Schematics of Measurement Setups 131

Appendix F Supporting Information for Chapter 5 135

Appendix G List of Abbreviations 142

Abstract

Al-rich AlGaN is required for light-emitting diodes (LEDs) and lasers operating in the deep-ultraviolet (UV) spectral range, solar-blind photodetectors, integrated UV photonics, and future high-power electronic devices. For many of these applications, it is essential that AlGaN with atomically smooth surface and with a minimal level of defects and dislocations can be epitaxially grown on foreign lattice-mismatched substrates, which are of lower cost, larger size and more widely available than bulk GaN or AlN substrates. In this work, with the use of molecular beam epitaxy (MBE), superior quality AlN and Al-rich AlGaN grown on sapphire are demonstrated. For AlN epilayers grown directly on sapphire, the X-ray diffraction (XRD) (002) rocking curve peak is significantly narrower than that previously reported for samples of comparable thicknesses. By employing a careful sequence of cycled in situ high-temperature annealing, many of the dislocations and stacking faults generated at the AlN/sapphire interface are reduced within the first 50 nm of growth. The photoluminescence (PL) emission is twice as strong as commercial AlN epitaxial templates that are over 10 times thicker, without the presence of defect-related emissions. With increasing thicknesses, the (002) and (102) rocking curve peak widths are among the best reported for AlN epitaxially grown on sapphire. Furthermore, a detailed study of Al-rich AlGaN epilayers was conducted. A method was developed to precisely control the alloy composition by tuning the Al flux and N flow rate. Under optimized conditions, $Al_{0.6}Ga_{0.4}N$ epilayers exhibit a surface roughness <0.4 nm, and strong PL emission at room temperature. Despite the lattice mismatch between AlGaN, AlN and sapphire, the formation and propagation of dislocations is significantly suppressed. This work presents important insights into

obtaining superior-quality wide-bandgap Al(Ga)N epilayers on lattice-mismatched substrate without the limitations of thick buffer layers, in order to break the efficiency bottleneck of deep-UV optoelectronics.

Hexagonal boron nitride (h-BN) has shown tremendous promise when used alongside other two-dimensional (2D) materials such as graphene, and as a wide-bandgap semiconductor for deep-ultraviolet optoelectronics and quantum photonics. Owing to its large bandgap energy comparable or higher than Al(Ga)N, h-BN can be used to form heterostructures to address some of the critical challenges of Al(Ga)N-based systems. In this context, dislocation-free AlN/BN nanowire heterostructures were grown directly on Si substrate. AlN/BN deep-UV LEDs, exhibiting a relatively low turn-on voltage (<7 V) and strong electroluminescence (EL) emission at ~210 nm at room temperature were demonstrated for the first time. The epitaxy of h-BN was then studied. Using high-temperature MBE, domains of exceptional crystalline quality were obtained on Ni substrate, with strong excitonic PL emission. It was theoretically and experimentally demonstrated that, even though the energy gap of h-BN is indirect, it luminesces as strongly as direct-gap materials, because of unusually strong phonon coupling. The luminescence intensity (~220 nm) of such a h-BN sample was 10 to 100 times stronger than that of commercially grown direct-bandgap AlN, demonstrating the extraordinary potential of epitaxial h-BN for deep-UV optoelectronics and quantum photonics. By forming a p-i-n structure using this high-quality h-BN as the active region, the current-voltage (*I-V*) and EL characteristics of a h-BN deep-UV LED is reported for the first time.

Chapter 1 Introduction

1.1 Optoelectronic Devices

1.1.1 Light-Emitting Diodes

Physical principles

The basis of optoelectronic devices is a conversion process between electrical and optical energies. A light-emitting diode (LED) is a semiconductor device that converts electricity into light. It builds off another electronic device, the diode. The simplest structure of a diode is the p-n junction, which is formed by layering p-type and n-type semiconductor materials. A p-type semiconductor is doped with acceptor impurities, thus enabling the presence of holes (positive charges) flowing in the material. Conversely, an n-type semiconductor is doped with donor impurities, such that its carriers are electrons (negative charges). In an LED, at the interface of these two layers, an active layer is formed where the light emitting properties occur. In a practical device, these layers rest on a substrate and include positive and negative metal contacts, as shown in Fig. 1.1.

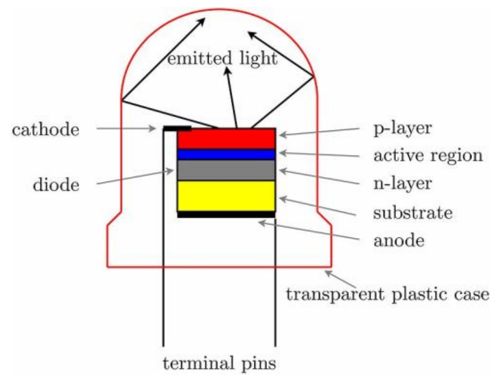

Figure 1.1 – Cross-sectional view of a thin film LED. (Source: Wikipedia.org)

A practical way to understand the operating principles of an LED is to refer to the band theory of solids [1], [2]. In the case of a semiconductor, two distinct bands are formed: the valence band at a lower energy level and the conduction band at a higher energy level. Free electrons flow in the conduction band while free holes are in the valence band. Between these two regions is a band gap, where no charge carriers should be found. Furthermore, in the case of a p-n junction, due to the misalignment in energies of the two regions, band bending is present at the interface. The movement of charge carriers given an applied forward voltage and the band structure of an LED are shown in Fig. 1.2. When electrons and holes reach the active region and are correctly aligned, the electron in the conduction band can recombine with the hole [3]. When recombination occurs, energy is released. In most semiconductor devices, including standard diodes, this energy is dissipated in the form of heat (lattice vibrations), which is referred to as nonradiative recombination. However, in the case of LEDs, radiative recombination can also occur, releasing a photon (light). The electrical properties of an LED are very similar to those of a diode. The current-voltage (I-V) characteristics are reviewed in Fig. 1.3. When a forward voltage is applied and the turn-on voltage of the device is reached, an exponentially increasing current starts flowing through the device. In terms of the band theory, a forward voltage reduces band bending enabling the

charges to move from one region to the other. The current passing through the device injects free electrons (and holes) causing some of them to radiatively recombine and generate light. However, when a reverse voltage is applied, by inverting the polarity of the source for example, band bending is increased, and the charge carriers do not have enough potential energy to overcome this barrier and cannot move from one region to the other. In other words, there is no current that flows through the device apart from a small constant leakage current. Lastly, if too high reverse voltage is applied, it will cause the device to break down.

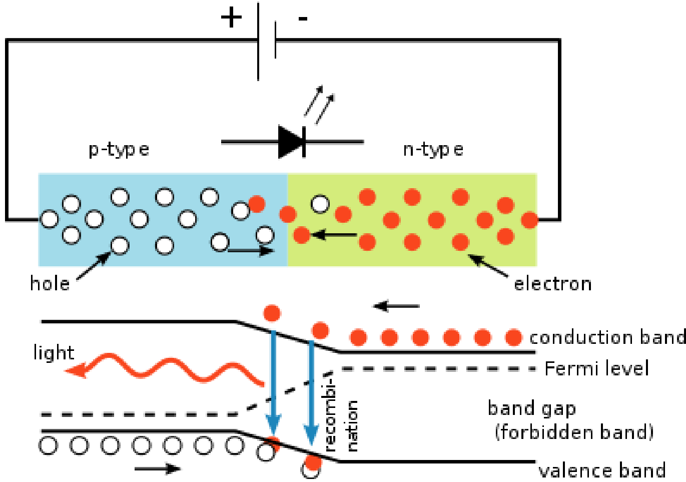

Figure 1.2 – Simplified LED structure and band diagram. (Source: Wikipedia.org)

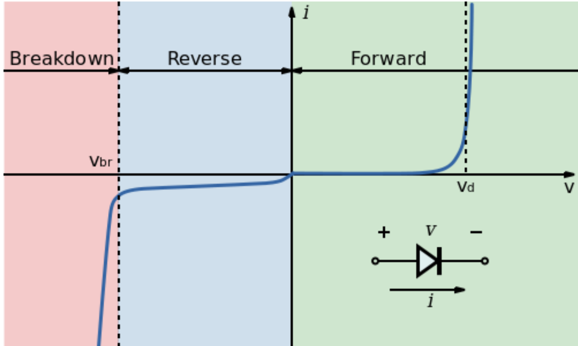

Figure 1.3 – I-V characteristics of an LED. (Source: Wikipedia.org)

Some of the fundamental optical properties of the LED can also be understood from band theory. A first property is the wavelength of light that is emitted (λ), also equivalent to the photon energy (E_{photon}) and frequency (v). Indeed, these are directly related to the bandgap energy of the semiconductor (E_g), by relating to the Plank constant (h) and speed of light (c), as expressed in Equation 1.1 [3].

$$E_g \approx E_{photon} = \frac{hc}{\lambda} = h\nu \qquad \text{(Equation 1.1)}$$

Since the bandgap energy is characteristic of the semiconductor that is used, different wavelengths can be obtained by using different materials. For example, gallium arsenide (GaAs), having a low bandgap energy, is therefore used for infrared (IR) applications [4]. The electromagnetic spectrum is included in Appendix A.

Solid-state lighting

One of the most promising applications of the LED is solid-state lighting [3]. This term refers to any type of lighting technology that makes use of solid-state devices. While it has been seen that LEDs can emit virtually any color of the electromagnetic spectrum, white light is desired for general lighting purposes. A first method involves the combination of red, green and blue LEDs in order to perceive white light. These wavelengths can be obtained using gallium nitride (GaN) and indium gallium nitride (InGaN) materials. The second method that is the most widely used today is the combination of a blue LED and a phosphor [3]. A phosphor is a luminescent chemical substance that can absorb some of the blue light from the LED and re-emit it at longer wavelengths, such as green and red colors, leading to the perception of white light. An example of such a spectrum is shown in Fig. 1.4. The dominant peak is at the frequency of blue light (~460 nm) with the presence of a broader emission due to the phosphor, Ce:YAG in this case. In this technology, the blue LED is preferred for its very high efficiency. There is however an energy loss in the

photon energy down-conversion process by the phosphor, referred to as Stokes shift [3], impacting the overall efficiency of the white LED.

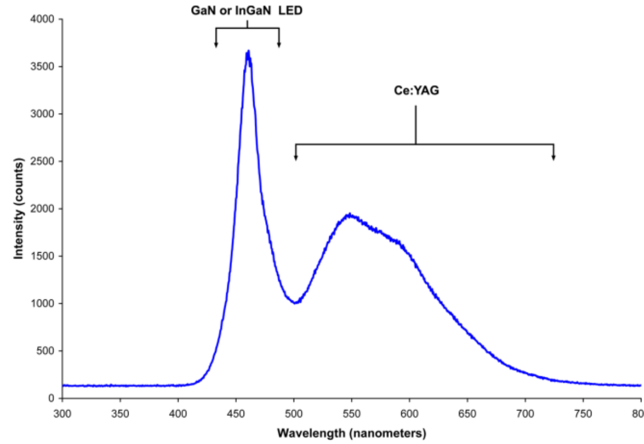

Figure 1.4 – Emission spectrum of a phosphor-coated white LED. (Source: Wikipedia.org)

Performance metrics

There are several efficiency metrics that characterize an LED. The first is the internal quantum efficiency (*IQE*), relating the number of photons that get generated in the active region and the number of electrons that were injected into the LED [3]. This is shown in Equation 1.2.

$$IQE = \frac{P_{int}/h\nu}{I/e} \qquad \textit{(Equation 1.2)}$$

In this equation, P_{int} is the optical power, I is the injected current and e is the elementary charge constant (1.602×10^{-19} C). *IQE* can also be defined based on the *ABC* model, as shown in Equation 1.3 [5], which takes the ratio of the radiative recombination rate and the rate of all recombination.

$$IQE = \frac{Bn^2}{An+Bn^2+Cn^3} \qquad \textit{(Equation 1.3)}$$

In this equation, n is the carrier concentration, and A, B and C are the Shockley–Read–Hall (SRH), radiative and Auger recombination coefficients, respectively. The two main nonradiative processes are SRH recombination due to traps (localized energy states) created within the bandgap by

dopants or defects in the crystal lattice, and Auger recombination, a higher order process involving three carriers [6]. For a typical InGaN/GaN quantum-well-based LED, reported values of A, B and C are 10^7 s^{-1}, 10^{-10} $cm^3 \cdot s^{-1}$ and 5×10^{-29} $cm^6 \cdot s^{-1}$, respectively [7].

As light is produced in the active region, it does not necessarily mean this light will escape into the surrounding environment. It can for example reflect and get reabsorbed due to total internal reflection (TIR). The light extraction efficiency (*LEE*) is defined as the ratio of the number of photons emitted in free space versus the number of photons generated in the active region of the LED [3], as shown in Equation 1.4, where P_{opt} is the optical power of light emitted into free space.

$$LEE = \frac{P_{opt}}{P_{int}} \quad \textit{(Equation 1.4)}$$

Furthermore, not all injected carriers will make it to the active region to potentially recombine and generate a photon. For this reason, the carrier injection efficiency (*CIE*) is also considered. The external quantum efficiency (*EQE*) is thus the product of these three factors [3], as shown in Equation 1.5.

$$EQE = IQE \times LEE \times CIE \quad \textit{(Equation 1.5)}$$

Lastly, commercial devices are rated by their power efficiency or wall-plug efficiency (WPE), which relates the optical power to the electrical power [3], as shown in Equation 1.6.

$$WPE = \frac{P_{opt}}{IV} \quad \textit{(Equation 1.6)}$$

Most commercial LEDs have their WPE specified in lumens/watts (lm/W) instead of percentages, where the maximum efficiency (100%) is defined to be ~330 lm/W for a white LED. To get a feel for numbers, currently sold LEDs are rated to be ~100 lm/W.

LEDs provide many advantages compared to other technologies such as incandescent and fluorescent lighting [3]. First, they are much more efficient, and therefore require only a fraction of electrical power to operate. They can also be tuned into a variety of colors, made much smaller,

resist to external shock and last for decades, much longer than the lifetime of any other technology. Their on/off time is also very short, meaning that LEDs can have interesting applications in communications, such as Li-Fi technology, and smart lighting, where lights can be dynamically turned on or off depending on the location of someone in a given room [8].

Device fabrication

As shown in Fig. 1.5, several major steps are required to form an LED device. The first is the growth of the p-n junction structure onto a substrate. Standard microfabrication techniques [9] are then used to mainly define the individual devices on the wafer and add metal contacts. These include photolithography, deposition and etching. Photolithography uses ultraviolet (UV) light to imprint the pattern of a mask onto the wafer coated with a cured photosensitive resist. Deposition is adding a layer of material, such as a metal, on the surface of the wafer. Lastly, etching is selectively removing an exposed layer of material. The steps for fabricating a simple LED are listed in Appendix B. Due to the scale of the structures and their sensitivity to humidity and contaminants such as dust, the fabrication process is performed in a cleanroom environment. The individual devices can then be diced, and the chips are packaged based on the desired application. It is worth noting that device packaging designs are often optimized for light extraction and thermal management.

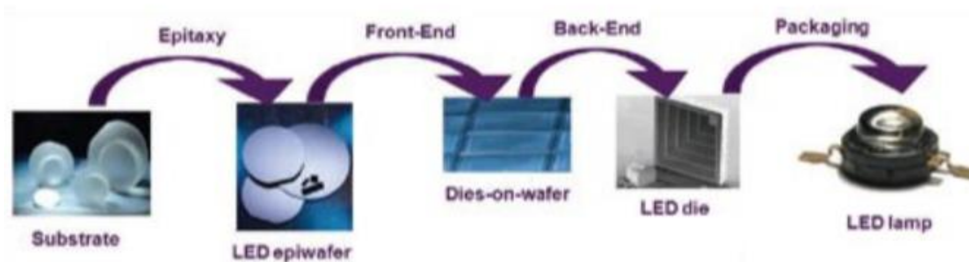

Figure 1.5 – Fabrication steps of an LED. (Source: Yole Développement)

1.1.2 Laser Diodes

The laser diode (LD) is another type of semiconductor optoelectronic device [4], [6]. The LD is pumped with electrical current similar to the LED, but lasing conditions are achieved to produce stimulated emission. The generated light is therefore of the same wavelength, coherence and phase. Radiative recombination in the LED results in spontaneous emission, where the photons are emitted randomly. To achieve the lasing conditions, higher bias currents are required to reach threshold optical gain, and the LD structure needs to include an optical cavity for feedback.

1.1.3 Photodiodes

Photodetectors convert light into electrical current [6]. Similar to the LED, the photodiode is a p-n junction, but operating in reverse bias, such that an impinging photon with sufficient energy will create an electron-hole pair. The electric field applied on the depletion region will cause the holes and electrons to separate and move towards the anode and cathode, respectively, resulting in a photocurrent. A p-i-n structure is often used to increase the depletion region, resulting in faster response time by promoting the absorption process. While photodiodes are optimized for light detection and sensing, solar cells are based on a similar principle to convert the absorbed light into electrical energy.

1.2 Bandgaps and Heterojunctions

1.2.1 Overview

Based on the electronic band structure theory of solids, electrons in semiconductors and insulators are confined in the valence band and when enough energy is provided can transition to the conduction band. As was mentioned, the forbidden region between the valence and conduction bands is referred to as the bandgap. The bandgap is important for optoelectronic materials, as it

dictates the charge carrier and photon interactions and transitions. For example, in LEDs, the energy of the emitted photons will correspond to the bandgap of the semiconductor material in the active region. Typically, insulators have a larger bandgap than semiconductors, such that the transition for electrons to the conduction band, thus allowing current conduction, is difficult. This however does not truly distinguish these two classes of materials. Materials that have a large bandgap (greater than a few eV of energy), but with tunable conductive properties by for example doping, are known as wide-bandgap semiconductors.

1.2.2 Varshni's Empirical Equation

The bandgap energy of a semiconductor varies with temperature, and can be described by Varshni's empirical equation, shown in Equation 1.7 [10].

$$E_g(T) = E_g(0) - \frac{\alpha T^2}{T+\beta} \qquad \textit{(Equation 1.7)}$$

T is the temperature (K), $E_g(T)$ is the bandgap energy at a given temperature (eV), $Eg(0)$ is the bandgap energy at 0 K (eV), and α and β are the Varshni coefficients (in eV/K and K, respectively). From this equation, it is possible to see that the bandgap energy decreases with increasing temperature. The constants $Eg(0)$, α and β are material dependent. Values for these parameters for the III-Nitrides have previously been reported [10]–[12]. For example, in the case of GaN, values for α range from 0.84 to 1.28 meV/K, β ranges from 737.9 to 1190 K, and $Eg(0)$ ranges from 3.458 to 3.57 eV. Varshni's equation can also be used to determine the temperature of a semiconductor when the bandgap energy is known or measured by solving for temperature.

1.2.3 Direct and Indirect Bandgap Semiconductors

In looking at the band structure of semiconductors, an important distinction that is made is whether they have a direct or indirect bandgap. If the momentum of the highest energy state of the valence band aligns with the lowest energy state in the conduction band, then then material has a

direct bandgap. This distinction is made in Fig. 1.6. Given that recombination requires conservation of both energy and momentum to be satisfied, a direct bandgap material is favored for optoelectronics. Radiative recombination can occur in indirect bandgap materials but requires the absorption or emission of a phonon with momentum matching the difference between that of the electron in the conduction band and hole in the valence band. Because of the need for the right phonon, the radiative recombination process is slower and is less likely to occur before nonradiative recombination, which is why direct bandgap materials are almost always used for semiconductor light-emitting devices. This is less of an issue for light-absorbing devices as long as the impinging photos have sufficiently high energy to achieve a band-to-band transition.

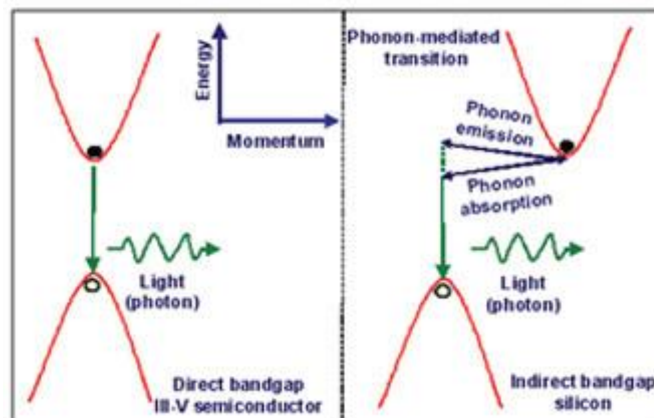

Figure 1.6 – Schematic of recombination in (left) direct and (right) indirect bandgap semiconductors. (Source: APS.org)

1.2.4 Optical and Electronic Bandgaps

Another distinction between bandgaps relevant for semiconductor optoelectronics is that of the optical versus electronic bandgap. The difference is negligible for most inorganic semiconductors, where the interaction between the electrons and holes is little. However, when the exciton (bound electron-hole pair) binding energy of the material is large, as can be the case for

wide-bandgap semiconductors, the optical bandgap energy corresponds to that of a photon and the exciton that is created. The electronic bandgap considers the additional energy required to separate the electron and hole, allowing for charge transport to occur.

1.2.5 Heterojunctions

A heterojunction is formed when two semiconductor materials with unequal bandgaps are paired. Heterojunctions can be advantageous in many solid-state device applications, leading to the development of room-temperature LDs, quantum-well-based LEDs and high-frequency transistors. Heterostructures can be formed by combining multiple heterojunctions. Quantum dot-based devices are an example of nanoscale heterostructures. Heterojunctions can also exhibit interface effects that can be engineered, enabling the development of devices based on two-dimensional (2D) layered materials and van der Waals heterostructures. The behavior of the heterojunction will depend on the alignment of the energy bands at the interface. The three types are illustrated in Fig. 1.7, corresponding to a straddling gap (Type I), staggered gap (Type II) and broken gap (Type III).

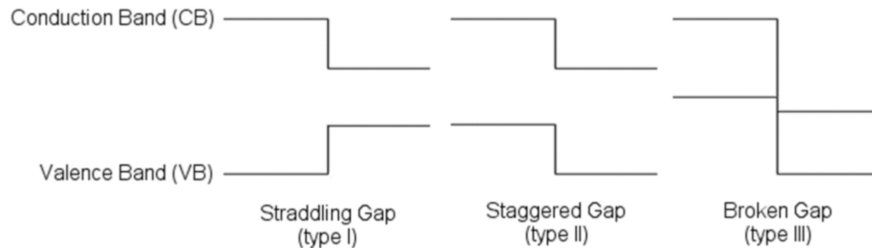

Figure 1.7 – Flat-band schematic of the three types of heterojunction interfaces. (Source: Wikipedia.org)

1.3 III-Nitride Materials

1.3.1 Overview

Although silicon (Si) is the most commonly used semiconductor in electronics, for optoelectronic devices, compound semiconductors, such as from the III-V groups as shown in Fig. 1.8, are preferred. A subset of the III-V semiconductors are the III-Nitrides, where nitrogen (N) is used as the group-V element. GaN, the most commonly used III-Nitride material, has gained great interest due to many advantages for electronic and optoelectronic applications [13]. These benefits include its direct, wide bandgap of 3.4 eV, useful for LEDs in the visible and UV spectral range, and high-power electronics.

Figure 1.8 – Portion of the periodic table showing group-III and group-V materials that are compounded to form III-V semiconductors. (Source: hypnocube.com)

The crystal structure of GaN is wurtzite, depicted in Fig. 1.9. Indium nitride (InN) has the lowest bandgap of the III-Nitrides at ~0.65 eV. Aluminum nitride (AlN) has a large bandgap energy of ~6-6.2 eV, making it very relevant for deep-UV applications.

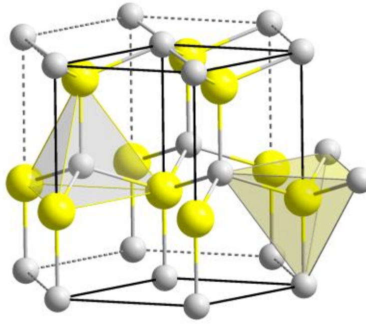

Figure 1.9 – Wurtzite crystal structure schematic. (Source: Wikipedia.org)

1.3.2 Alloying

A distinct advantage of the III-Nitride compound semiconductors is the possibility to form alloys, allowing for bandgap engineering over a span ranging from the near infrared to the deep ultraviolet. For example, in the case of aluminum gallium nitride (AlGaN), the ternary alloy of AlN and GaN, its bandgap can be tuned between 3.4 and 6 eV by varying the composition of aluminum. The figure in Appendix C shows this dependence for $Al_xGa_{1-x}N$ and other alloys in the III-Nitride family. This figure also shows the inverse relation between the bandgap energy of a material and its lattice constant. Vegard's law is a useful empirical equation to describe the lattice constant (*a*) of the resulting alloy based on the composition *x*, as shown in Equation 1.8.

$$a_{A_{(1-x)}B_x} = (1-x)a_A + xa_B \qquad \textit{(Equation 1.8)}$$

Taking the weighted mean is however insufficient in determining the bandgap energy of the resulting alloy, even as an approximation, and requires accounting for a second order bowing term. The table in Appendix D is a useful lookup chart relating AlGaN alloy concentration, bandgap energy (E_g) calculated taking into account the bowing effect [6], wavelength (λ) based on Equation 1.9 where *c* is the speed of light [6], and XRD angle based on Vegard's law.

$$\lambda = \frac{hc}{E_g} \approx \frac{1240\ nm}{E_g(eV)} \qquad \textit{(Equation 1.9)}$$

1.3.3 Boron Nitride

Boron nitride (BN) is the last of the III-Nitride family and has in recent years become a material of great interest because of its unique physical properties and potential to enhance the performance and functionality of other material systems and structures. BN can be found in various polymorphs [14], as shown in Fig. 1.10. The hexagonal polymorph (h-BN) consists of a stacking of boron and nitrogen atoms, where the different layers are bonded by weak van der Waals forces. h-BN is therefore a 2D material and has a very similar structure as graphite, which is why BN is often referred to as "white carbon". The cubic polytype (c-BN) is therefore equivalent to diamond. Rhombohedral BN (r-BN) is similar to h-BN, but the stacking between the different layers is disorganized (random). w-BN has a wurtzite structure, but is a rarer polymorph of BN.

The synthesis of commercially produced h-BN involves using a boric oxide or acid and a nitrogen-containing compound. Following this reaction, an annealing procedure is required to remove any residual oxide and to crystallize the obtained amorphous BN. The production of c-BN and w-BN involves treating h-BN at high pressure and temperature. c-BN is therefore produced in a similar manner as synthetic diamond. The low-pressure thin film growth of c-BN has been demonstrated, but with mixed results. As mentioned, w-BN is more difficult to obtain and often contains a mix of h-BN and w-BN. BN has high thermal conductivity but low electrical conductivity, due to the partly ionic bonds that reduce covalency. This rare characteristic, as well as its strong chemical stability (resistance to most acids and wetting from metals) and thermal stability (at temperatures >1000 °C), make BN a very attractive material for many applications [14]. h-BN, due to the mechanical interlayer interactions, is used in cosmetics and as a lubricant in extreme environments such as in space. It can also be pressed and shaped in the form of crucibles

for high-temperature applications. c-BN, which has a mechanical hardness comparable to diamond, is used as an abrasive and in cutting tools. It has also been widely considered as the next-generation material for high-power and high-frequency electronics.

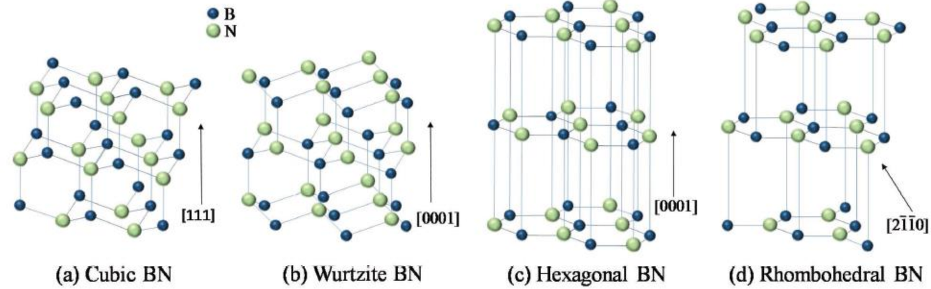

Figure 1.10 – Crystal structure schematic of the polymorphs of BN. (Source: [14])

1.3.4 Hexagonal Boron Nitride

Fundamental properties

Many uncertainties still exist in the fundamental material properties of h-BN. Its bandgap energy remains under debate, with reports spanning from 5.9 to 6.5 eV. There is also strong controversy as to whether h-BN has a direct or indirect bandgap. Some questions also arise when discussing h-BN as an insulator in some cases, but as a semiconductor in others. However, regardless of these uncertainties that will be discussed throughout this thesis, many characteristics of this material are well established based on a variety of methods.

Transport properties

A recent study of the transport properties of a thin film of h-BN concluded that it is a space-charge limited conduction mechanism [15]. A room-temperature mobility is reported of up to 0.01 $cm^2 \cdot V^{-1} \cdot s^{-1}$. This work also mentions that electric fields of up to 100 $kV \cdot cm^{-1}$ were used in this measurement without any dielectric breakdown. As such, h-BN shows favorable electronic

properties as a dielectric substrate. In other studies related to the use of h-BN for optoelectronic devices, where n- and p-type conduction are necessary, Hall effect measurements are performed on Si- and Mg-doped h-BN [16], [17]. Using Mg as the dopant, a room-temperature resistivity of ~2 Ω·cm, hole mobility of 2-26 $cm^{2}\cdot V^{-1}\cdot s^{-1}$ and hole concentration of 10^{18}-10^{19} cm^{-3} are reported. This value of resistivity is six orders of magnitude lower than that of Mg-doped AlN, and the Mg activation energy is found to be 30 meV, compared to ~0.5 eV in the case of AlN. Using Si as the dopant, n-type properties were however only observed at temperatures above 700 K. In this temperature range, a resistivity of ~12 Ω·cm, electron mobility of ~48±24 $cm^{2}\cdot V^{-1}\cdot s^{-1}$ and electron concentration of ~10^{16} cm^{-3} are reported. There have also been reports of p-type conduction in Be-implanted h-BN films obtained by sputtering method [18].

Optical properties

The first evidence of h-BN as a suitable light-emitting material was in 2004, when Watanabe, et al. demonstrated cathodoluminescence (CL) at 215 nm [19], as shown in Fig. 1.11. The authors attributed this peak to an S-like free exciton absorption and proposed that h-BN therefore has a direct bandgap of 5.971 eV. Furthermore, they showed that above a threshold electron-beam excitation, the luminescence spectrum of this material starts showing resonance peaks similar to a laser.

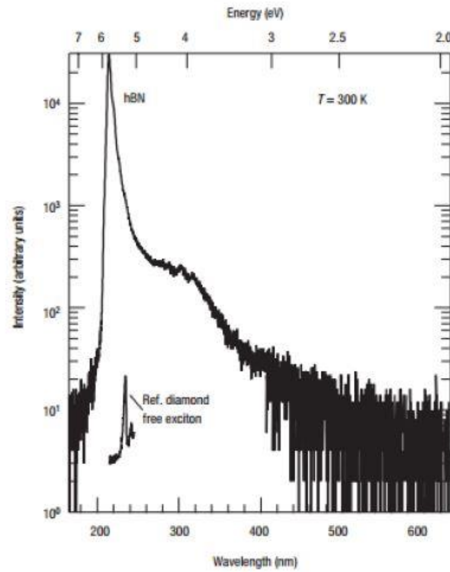

Figure 1.11 – CL spectrum of h-BN showing a luminescence peak at 215 nm. (Source: [19])

Twelve years later, in 2016, Cassabois, et al. demonstrated photoluminescence (PL) at 215 nm, but attributed the mechanism to phonon-assisted transitions, as outlined in Fig. 1.12 [20]. They attributed all the PL peaks obtained at low temperature to optical and acoustic phonon replicas and an indirect exciton. They reported an exciton binding energy ~130 meV by phonon-assisted two-photon absorption and concluded that h-BN has an indirect bandgap of 5.955 eV. Later in 2016, researchers from Texas Tech University published results also from low-temperature PL studies (Fig. 1.13), but in this case found that the various short-wavelength peaks match expected excitonic transitions in h-BN [21]. As shown in the figure, some of these peaks are attributed to S-series free exciton transitions, and the others to D-series impurity-bound (trapped) exciton transitions. Furthermore, they added contacts to their material and conducted photocurrent excitation spectroscopy measurements [22]. They identify three peaks at 5.39, 5.69 and 6.42 eV at room temperature, and correlate with their PL results to construct the energy band diagram shown in Fig. 1.14. According to these results, h-BN should therefore have a direct bandgap of 6.42 eV with

a free exciton binding energy and bound exciton binding energy ~0.73 eV and 0.20 eV, respectively. Other theoretical and recent experimental reports propose an indirect to direct bandgap crossover for monolayer (ML) BN [14], [23], [24]. The variations of the calculated band structure of h-BN showing this direct bandgap crossover is shown in Fig. 1.15.

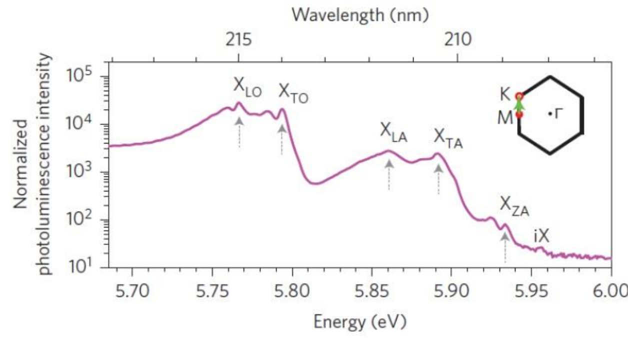

Figure 1.12 - Low-temperature PL spectrum of h-BN, highlighting the various phonon-assisted transitions for every observed luminescence peak at around 215 nm. These include acoustic and optical phonons in the longitudinal and transverse directions, as well as an indirect exciton (marked by iX). (Source: [20])

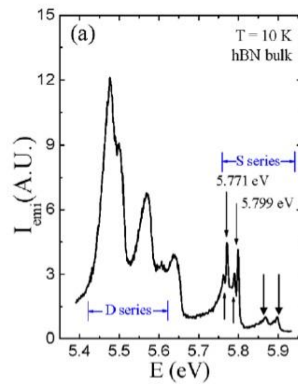

Figure 1.13 – Low-temperature PL spectrum of h-BN, with various S and D series exciton transitions identified with arrows. (Source: [21])

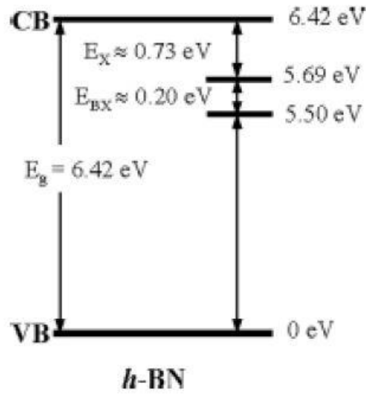

Figure 1.14 – Proposed energy band diagram of h-BN based on PL and photocurrent excitation spectroscopy measurements. The bandgap, and free and bound exciton binding energies are marked as E_g, E_X and E_{BX}, respectively. (Source: [22])

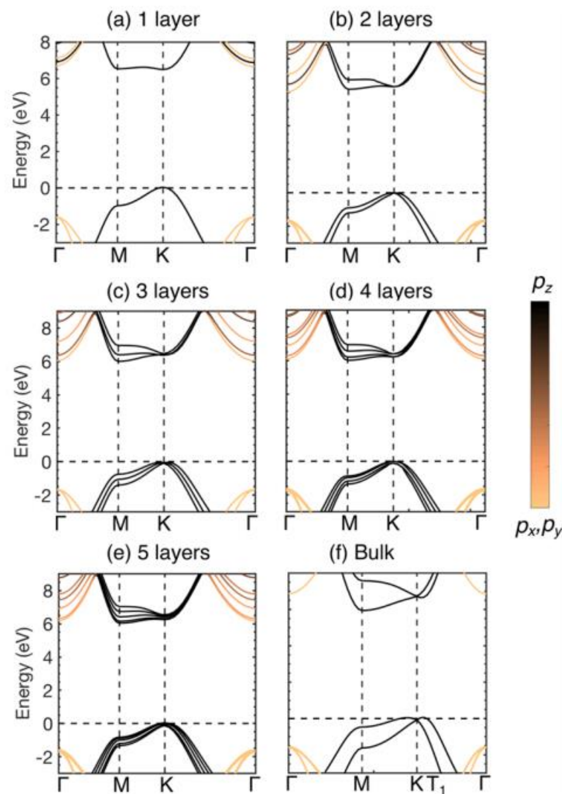

Figure 1.15 – Calculated band structure of varying layers of h-BN. (Source: [24])

Defect-induced transitions have also been studied in h-BN. Attaccalite, et al. have modeled the effect of point defects in h-BN [25], and Fig. 1.16 shows the different predicted defect-induced transitions. Growth-related defects can lead to such transitions. For example, the commonly observed 5.3 eV luminescence peak in h-BN has been attributed to a quasi-donor-acceptor pair transition, from a nitrogen vacancy level near the conduction band minimum to the acceptor level above the valence band maximum [26].

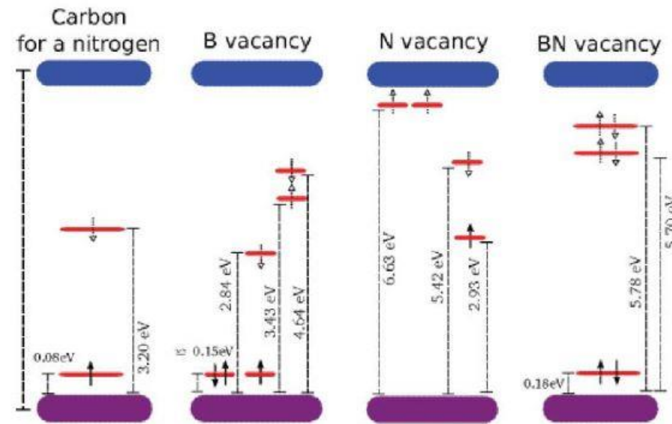

Figure 1.16 – Calculated band structures of h-BN showing defect-induced transitions due to carbon impurities, and B, N and BN vacancies obtained from a theoretical study. (Source: [25])

Relevant applications

Due to its crystalline structure, h-BN can be the perfect 2D insulator with an atomically smooth surface. This property makes it suitable for van der Waals epitaxy [20], [27] and as a substrate for the growth of other 2D materials such as graphene [28]–[30].

h-BN as a wide-bandgap semiconductor has many promising applications in deep-UV photonics. In particular, owing to its large bandgap energy comparable or higher than Al(Ga)N, h-BN can be used to form heterostructures to address some of the critical challenges of Al(Ga)N-based systems, allowing for better device performance and efficiency. Indeed, h-BN is compatible

with (wurtzite) Al(Ga)N (both III-Nitride materials), has a band alignment and separation that favor carrier injection and confinement, and is reported to have a lower acceptor energy and higher free hole concentration [16], [17]. Regarding lattice matching with AlN, as shown in Fig. 1.17, while there is a mismatch of ~20% along the *a*-direction, four *a*-lattice constants of AlN is very close to five *a*-lattice constants of h-BN. As such, a 5/4 alignment can occur at the interface, reducing to an effective lattice mismatch to ~0.6% [16].

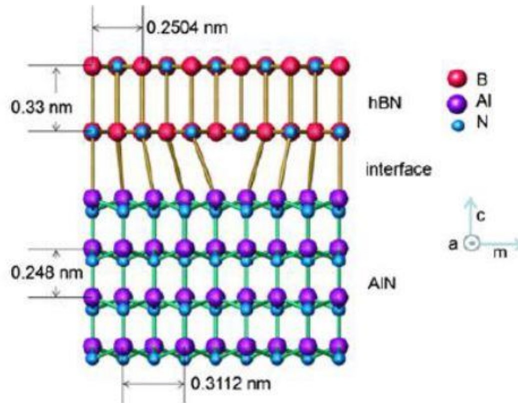

Figure 1.17 – Lattice matching between wurtzite AlN and h-BN, showing a 5/4 alignment at the interface. (Source: [16])

To make use of h-BN thin films for either 2D heterostructures or deep-UV applications, the controllable growth of this material on a wafer scale becomes necessary. In that regard, to elucidate some of the important questions around this material, it becomes critical to understand, control and possibly even engineer the defects in these h-BN thin films. Moreover, a different research avenue has been to explore ternary compounds of BN, GaN and AlN to form BGaN and BAlN. Currently, only very low compositions of B can be used for the alloy not to be compromised by strain-induced defects, and segregation and phase separation effects [31], [32]. Lastly, there has been research on zero-dimensional (0D) h-BN quantum dots [33]–[35] and one-dimensional (1D) nanotubes as well [36]–[38].

1.4 Brief History of III-Nitride LEDs

Early development of epitaxial GaN began in the 1970s and 1980s [39], [40]. By the 1990s, revolutionary GaN LED improvements were achieved by Akasaki and Amano at Nagoya University, and high-brightness InGaN LEDs were demonstrated by Nakamura then at Nichia Corporation. These three scientists were awarded the 2014 Nobel Prize in Physics "for the invention of efficient blue light-emitting diodes which has enabled bright and energy-saving white light sources" [41]. Since then, several breakthroughs were made in the field of III-Nitride LEDs. In 2006, researchers at NTT Corporation demonstrated the first AlN deep-UV LED emitting at ~210 nm [42]. Shown in Fig. 1.18 are (a) the structure, (b) electroluminescence (EL) spectrum and (c) *I-V* characteristics of the LED and an equivalent metal-insulator-semiconductor (MIS) device. The device structures were grown on a thick AlN buffer layer on silicon carbide (SiC) substrate. It can be noticed that an AlN/AlGaN superlattice (SL) contact layers were included to form the ohmic contacts. These are however only semitransparent and will absorb some of the photons emitted from the AlN active region. Other than the near-band-edge emission at ~210 nm, a peak at ~230 nm is measured from the LED and is attributed to emission from the Mg impurity level in the p-type AlN layer. The authors also report a broad emission peak ~400 nm attributed to the Si impurity level in n-type AlN. Importantly, while the device exhibits the diode rectification behavior, the turn-on voltage is greater than 20 V. This value is unusually high, considering that the bandgap energy of AlN is ~6 eV, and is due to the poor doping characteristics of AlN epilayers, resulting in poor electrical efficiency. The output power at ~210 nm was reported to be ~20 nW at a current of 40 mA [42].

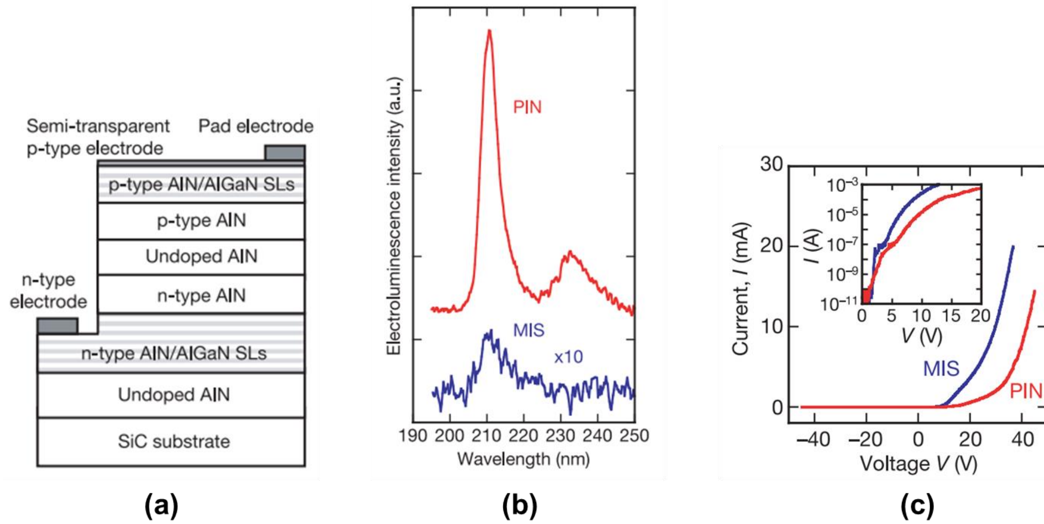

Figure 1.18 – (a) Schematic of the first AlN LED device structure. (b) EL spectrum of this AlN LED and an equivalent MIS structure. (c) I-V characteristics of these devices. (Source: [42])

More recently, III-Nitride nanostructures such as nanowires (nanocolumns) have been a topic of research. The first InN near-IR LED was demonstrated in 2014 by my predecessors while at McGill University [43]. Our group also demonstrated the first AlN LED by using nanowires in 2015 [44]. Shown in Fig. 1.19 are (a) the structure, (b) emission spectrum and (c) *I-V* characteristics of this AlN nanowire LED. As can be seen, these nanowires are grown on Si substrate. In order to promote the formation of AlN nanowires, a GaN nanowire template is first grown. EL at ~210 nm is measured, similar to the planar LED device. However, in this case the turn-on voltage is ~6 V, which is much lower than that of the planar LED device, and only limited by the bandgap energy of AlN. As such, the electrical efficiency of this device is much higher.

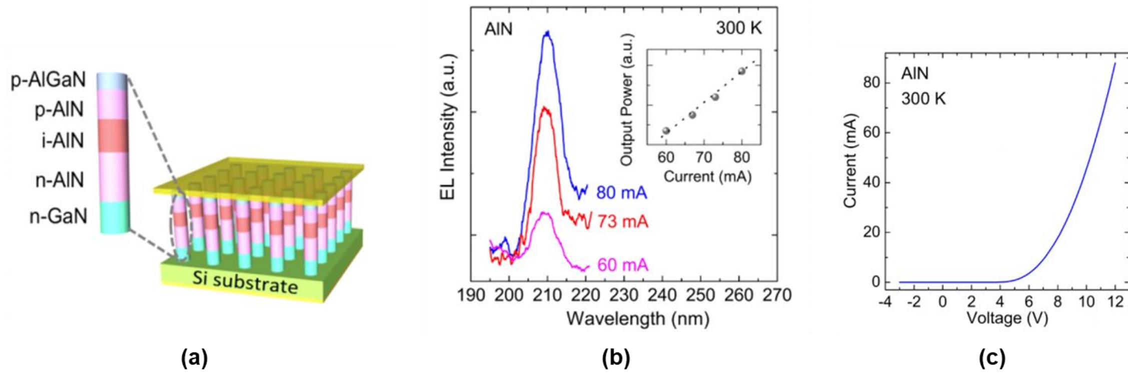

Figure 1.19 – (a) Schematic of the AlN nanowire LED on Si substrate. (b) EL spectrum and current dependence of the output power of the LED device. (c) I-V characteristics of the LED device. (Source: [44])

1.5 III-Nitride Nanowires

As their name states, nanowires are structures with at least one dimension (typically the diameter) in the nanoscale (10^{-7} to 10^{-9} meters). Given the nearly-1D nature of nanowires, as well as the advancement of their growth processes resulting in high-quality structures, nanowires are generally considered to be dislocation-free [45]. Due to lateral strain relaxation, a significant advantage is that they can therefore accommodate large lattice mismatches, even allowing direct growth on desirable substrates such as Si [46]. The concept of critical layer thickness that limits thin-film growth is not nearly as significant in the case of nanowires. Nanowires can be formed using either top-down or bottom-up approaches [46]. In the former case, a pattern is defined, and a selective etching process is used to define the desired nanostructures from a planar structure. In the latter, the nanowires are grown directly on a substrate by either using a catalyst or by controlling their nucleation. The bottom-up approach is used for the work presented in this thesis.

A very important advantage of nanowires for light emitting applications is improvements in terms of light extraction, owing to the large surface-to-volume ratio of the structures [47]. Kuo

et al. have performed detailed studies on the effect of the nanowire diameter on the LEE [48]. They report a high LEE of ~80% for a device emitting at 460 nm, without using a back reflector or thin films.

Due to these benefits, both the IQE and LEE of the nanowires can be higher than their planar counterparts. A significant issue however is the low CIE due to pronounced nonradiative surface recombination. This can be successfully addressed by forming a core-shell structure, where the shell consists of a wider-bandgap material that can effectively passivate the nanowire lateral surface [49].

1.6 Deep-Ultraviolet Light Emitters

1.6.1 Applications

As shown in Fig. 1.20, deep-UV light sources are important for a broad range of applications [50]. This includes disinfection of harmful microorganisms such as bacteria and viruses from surfaces and for water purification, sterilization of medical equipment, fluorescence for bio and chemical sensors, spectroscopy for scientific research, high-density optical storage, and improvements in photolithography as part of the microfabrication process.

Figure 1.20 – Applications requiring deep-UV light sources. (Source: courtesy of Nick Pant, University of Michigan)

The current technologies that are used to generate deep-UV light are mercury-vapor lamps and excimer lasers, which are however costly, bulky, inefficient and toxic. They also suffer from short lifetimes and instability. The development of solid-state deep-UV light sources is therefore highly attractive, as these are the only alternative to displacing these current technologies. Developing a solid-state alternative would also enable new technologies other than UV LEDs and LDs, including solar-bling photodetectors, integrated UV photonics and high-power electronics [51].

1.6.2 Al(Ga)N-Based Devices

The UV range can be subdivided into UV-A (315-400 nm), UV-B (280-315 nm), UV-C (100-280 nm), up until the extreme UV range approaching X-rays [3]. Wavelengths below 300 nm are considered to be in the deep-UV range [52]. Many of the mentioned applications require emissions in the deep UV, making it crucial to develop LEDs with emissions in the 200-nm range. To get deep-UV emission, semiconductor materials with a wide bandgap must be used, including AlGaN with high Al composition, with the extreme case being AlN.

Significant progress has been made in the development of AlGaN-based LEDs emitting in the UV-A and UV-B spectral ranges [51], [53]. However, as can be seen from Fig. 1.21, the quantum efficiency of the reported devices drops drastically <250 nm [54].

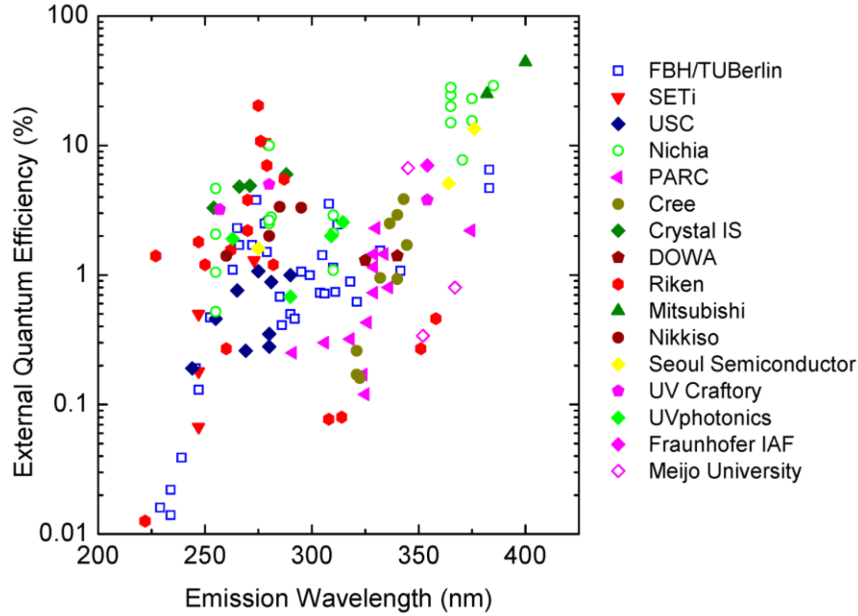

Figure 1.21 – Status of UV LEDs in terms of emission wavelength and quantum efficiency. (Source: [54])

Figure 1.22 is a schematic of the AlGaN-based UV LED fabricated at Riken, which is representative of the currently adopted design for short-wavelength UV LEDs [5]. It consists of a thick (~4 µm) undoped AlN buffer layer grown on sapphire, followed by a thick (~2 µm) Si-doped n-AlGaN buffer. The active region is formed by AlGaN multiple quantum wells (MQW) with higher Al composition in the barriers (~7 nm) than in the wells (~1-2 nm) for effective carrier confinement, similar to InGaN/GaN MQW LEDs in the visible spectral range [3]. The quantum wells are kept thin to suppress effects from piezoelectric fields [3]. The active region is then capped with an undoped AlGaN barrier (~20 nm) and a Mg-doped electron blocking layer (EBL) of ~15 nm. A thin (~10 nm) Mg-doped p-AlGaN layer and a ~20-nm-thick p-GaN contact layer are on top. Metal contacts are added to the p-GaN and n-AlGaN layers.

It is worth noting that a flip-chip configuration is often used for UV LEDs, such that the emission is collected through the substrate [5]. Reasons include to avoid absorption of the photons

by the p-GaN contact layer, and to prevent the metal contacts from blocking the light. However, it can be expected that some photons will be lost in the lower-quality and thick AlGaN and AlN buffer layers, and from TIR. Furthermore, because of challenges in Mg doping and poor hole transport (discussed in the subsequent section), the p-layers need to be kept thin, which leads to an asymmetry in the structure, resulting in poor electrical properties [55]. Because these limitations become increasingly severe with higher Al composition, the UV LED EQE decreases with shorter wavelengths as was shown in Fig. 1.21.

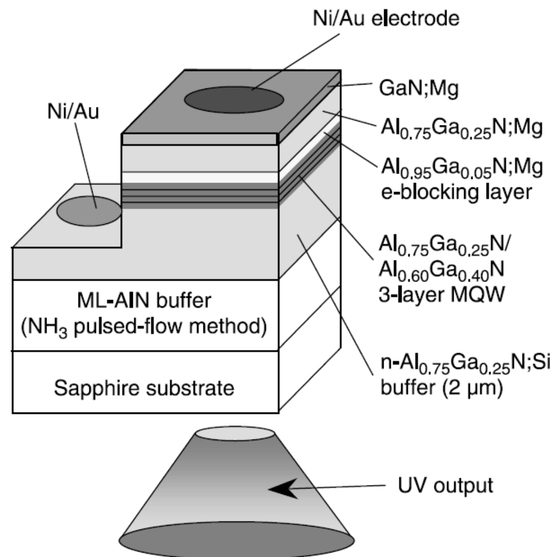

Figure 1.22 – Schematic of a commonly used design for UV LEDs. (Source: [5])

1.6.3 Challenges

Large dislocation densities

A primary cause of dislocations in III-Nitride materials originates from the lack of cost-effective and large-scale bulk substrates, requiring the use of lattice mismatched sapphire or SiC

[3]. This results in strained layers that lead to dislocations when relaxed above a critical thickness [56], as shown in Fig. 1.23.

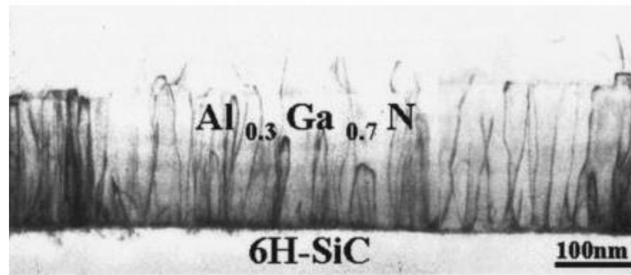

Figure 1.23 – Cross-sectional microscope image of AlGaN grown on SiC, highlighting the dislocations due to lattice mismatch. (Source: [57])

Dislocation densities have the effect of decreasing device efficiency, specifically the IQE, as shown in Fig. 1.24 [3]. While GaN is more tolerant to an increase in dislocation densities compared to III-As and III-P materials, as shown in this figure, the radiative efficiency is nevertheless reduced.

Techniques such as patterned substrates and thick buffer layers to promote epitaxial lateral overgrowth (ELO) [58] have been successful in mitigating some of the issues, resulting in a record UV LED EQE ~20% at 275 nm. The growth of AlGaN with high Al compositions remains a challenge.

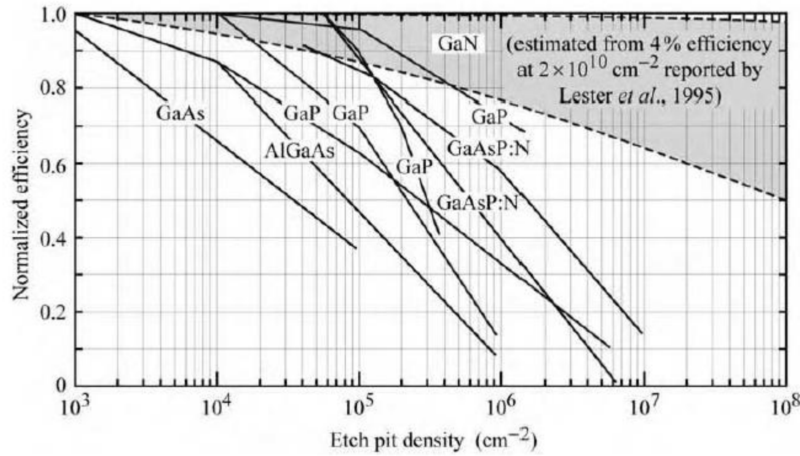

Figure 1.24 - Reduction of the radiative efficiency with an increase in etch pit density acting as dislocations. (Source: [3])

Poor light extraction

As was discussed, the LEE is one of the contributing factors of EQE. While the two-band model of a semiconductor is useful, it is an oversimplification of the actual band structure and neglects certain effects. In the case of GaN, for example, a more accurate visualization of the energy bands is shown in Fig. 1.25. While the conduction band (C) remains similar, the valence band separates into the heavy hole (HH), light hole (LH) and crystal-field split-off bands (CH) [6].

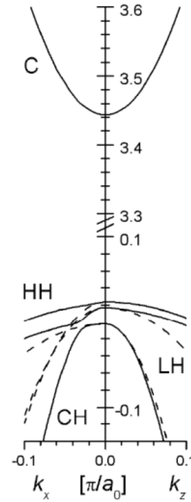

Figure 1.25 – Band structure of wurtzite GaN, showing the splitting of the valence band into the HH, LH and CH bands. (Source: [6])

The light that is emitted from GaN is mainly transverse-electric (TE) polarized [59]. This means that the electrical field vector is perpendicular to the *c*-axis, therefore light propagates in the vertical direction and can escape through the substrate or surface of the device [60], [61]. In the case of AlN, the band structure is different since the HH and CH band cross over and the CH band becomes closer to the conduction band [62]. This effect is also true for AlGaN with increasing Al mole fractions [50], as shown in Fig. 1.26 [63]. This rearrangement is significant, because it changes the polarization of emitted light from TE to transverse-magnetic (TM). TM polarized light means that it is the electric field is now parallel to *c*-axis, with the light mainly propagating in the lateral direction. TM polarized light is therefore harder to emit from the surface escape cone, which would cause the LEE of the LED to decrease [60]. This change in the optical polarization of emitted light is especially problematic for deep-UV LEDs, which use AlGaN with high Al composition.

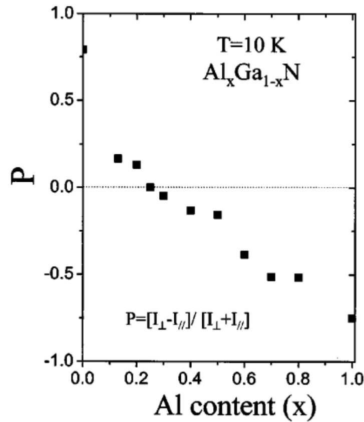

Figure 1.26 – Degree of polarization P as a function of Al content in AlGaN alloys, showing a transition from predominantly TE to TM polarized light with increasing Al composition. A decrease in P is indicative of stronger TM polarization. (Source: [63])

Lack of heterostructures

Electron overflow is an undesired process where the injected electrons escape the active region, or never enter it altogether, and go straight into the p-region. Then, even if they recombine, it will most likely be nonradiative [64]. Electron leakage and overflow have been identified as leading causes of efficiency droop [65]. Efficiency droop is a phenomenon where the efficiency of the LED drops significantly at high injection currents. This issue severely limits the fabrication of efficient high brightness LEDs that require high injection currents. For InGaN LEDs, a wider bandgap AlGaN electron blocking layer has shown to dramatically reduce carrier leakage and overflow [66]. This is shown in Fig. 1.27. However, for AlGaN devices, especially with higher Al compositions, an even wider bandgap material is unavailable to form this EBL.

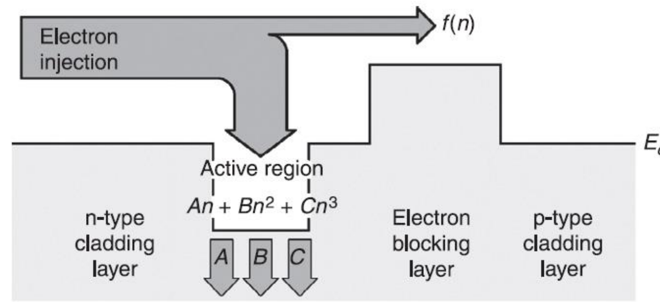

Figure 1.27 – Schematic of the conduction band of an LED device, highlighting the overflow of injected electrons, and the addition of an electron blocking layer. (Source: [5])

It is worth noting that in the case of nanowires, the lack of heterostructures raises the issue of surface recombination. Even though the IQE of a nanowire LED can be much higher than its planar counterpart, due to a reduction in defect densities, the poor CIE becomes a major bottleneck. This efficiency can be very low for nanowire LEDs (<10%) while it is near unity for conventional quantum well devices [49]. Low carrier injection is due to the large surface-to-volume ratio of nanowires, causing significantly enhanced surface recombination, which is mainly a nonradiative process. Due to the lost carriers at the surface, there are less carriers available in the active region for radiative recombination. This has previously been successfully mitigated for InGaN-based nanowire LEDs by employing a core-shell structure to effectively passivate the nanowire surface [49]. The shell material needs to have a larger bandgap to avoid absorbing the generated photos. This once again becomes difficult or impossible when the active region is already composed of a wide-bandgap material.

Inefficient p-type doping and hole transport

Compared to electrons, the transport of holes is especially problematic for two reasons. First, the concentration of holes is generally lower because of issues related to p-doping the material. In the case of GaN, even if high concentrations of Mg are achieved, the mobility of the

carriers will severely decrease due to impurity scattering [5]. Second, holes have a lower mobility than electrons, due to their increased effective mass [6]. This asymmetry between the transport properties of electrons and holes is identified as an important source for electron leakage and overflow [67], [68].

Additional challenges arise with p-type AlGaN, since the acceptor energy level of Mg increases with Al composition [69], as shown in Fig. 1.28, making it a much less efficient dopant at room temperature. Mg also becomes increasingly difficult to incorporate when growing Al(Ga)N at higher growth temperatures, given that Mg is a high vapor pressure material that will therefore desorb easily before incorporating into the structure [5], [51].

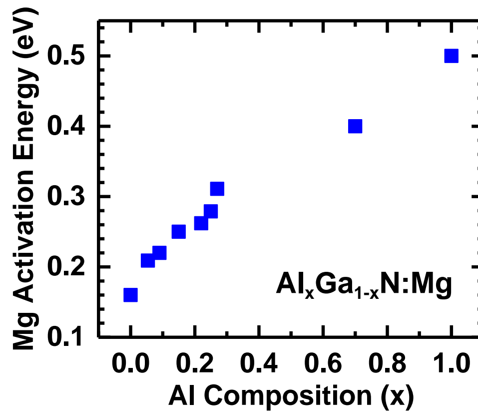

Figure 1.28 – Mg-dopant activation energy in p-doped AlGaN with varying Al composition. (Source: redrawn based on [69])

From a device perspective, forming an ohmic p-contact to a wide-bandgap material is yet another challenge. Deep-UV LEDs are therefore designed to include a lower composition (Al)GaN p-contact layer [42]. This facilitates carrier injection but causes some of the emitted photons to be absorbed.

1.6.4 Al(Ga)N Nanowires

Taking the case of the AlN nanowires as an example, the scanning electron microscope (SEM) image in Fig. 1.29(a) shows a forest of free-standing axial nanowires grown on Si substrate. Transmission electron microscopy (TEM) studies of these nanowires reveal that they are nearly strain and dislocation free (Fig. 1.29(b)) [70]. As such, a high IQE is expected. This is supported by the relatively strong PL intensity of such nanowires at a wavelength ~210 nm [71]. Furthermore, it is found that although the emitted light is TM polarized, it is predominantly emitted from the top surface of the sample due to strong light scattering effects, resulting in a high LEE [72].

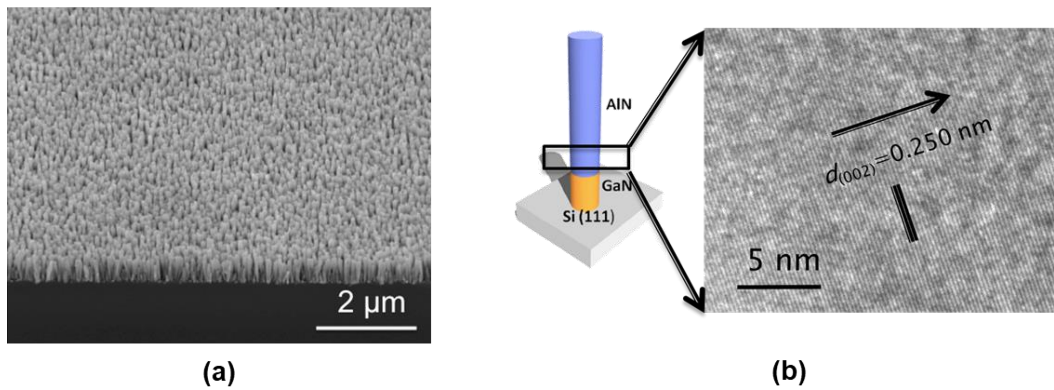

Figure 1.29 – (a) SEM image of free-standing AlN nanowires on Si substrate. (Source: [44]) (b) TEM image focusing on a single AlN nanowire, with the arrow showing the growth direction. (Source: [44], [70])

In terms of p-type doping, free hole concentrations up to 6×10^{17} cm^{-3} have been measured at room temperature in Mg-doped AlN, as compared to ~10^{10} cm^{-3} for AlN epilayers [73]. The derived Mg-dopant activation energy in these nanowires is determined to be 20-200 meV, which is lower than that reported for AlN epilayers (500-600 meV). It is determined that these effects stem from efficient hope hopping conduction in the Mg impurity band that is formed in p-type AlN nanowires [73].

Using a similar approach, AlGaN nanowires have also been achieved with tunable deep-UV emission by controllably varying the growth parameters [74]. Figure 1.30 shows the PL spectrum of such self-organized AlGaN nanowire samples with emission spanning the entire UV range by varying the substrate temperature during growth. From there, AlGaN nanowire LEDs have been demonstrated with tunable emission [74], including tunnel-junction nanowire LEDs operating in the UV-C band with enhanced output power [75]. Furthermore, electrically injected AlGaN nanowire UV lasers have also been demonstrated based on a similar approach [76]–[78].

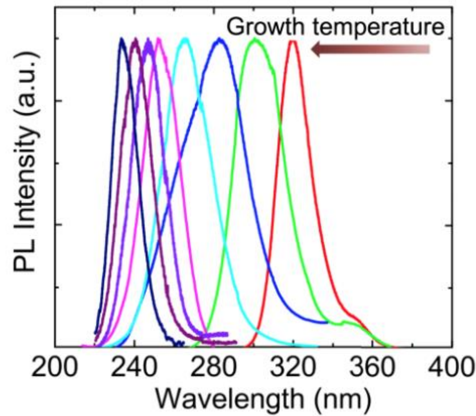

Figure 1.30 – PL spectra of AlGaN nanowire samples grown using different substrate temperatures. (Source: [74])

Moreover, through the controlled coalescence of AlGaN nanowire arrays grown using a selective area epitaxy approach on a pattered GaN template on sapphire substrate, a nearly-dislocation-free planar (quasi-film) surface can be achieved [79]. This is shown in Fig. 1.31.

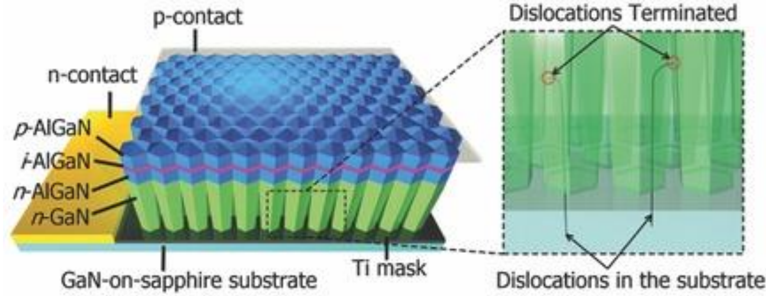

Figure 1.31 – Schematic of an AlGaN quasi-film structure formed by coalescing nanowires grown by selective area epitaxy. It is found that the dislocations from the lattice mismatch can be terminated with the lateral broadening and coalescence of the nanowires. (Source: [79])

1.6.5 h-BN-Based Light Emitters

As discussed, h-BN has unique properties that make it very promising for UV light emitting devices. It is the thinnest insulating material with a large bandgap energy ~6 eV. It can be synthesized with atomically smooth surface with minimal dangling bonds and charge traps, which is why it has been used as a substrate for other 2D materials. It can be used to form heterostructures with Al(Ga)N. There have been reports of CL and PL, demonstrating that it is a good light emitter. In that regard, it is even expected that the emitted light would be TE polarized, minimizing light extraction issues. While theoretical calculations give it an indirect bandgap, such that luminescence occurs from phonon-assisted transitions, recent reports indicate that monolayer BN may have a direct bandgap.

To date, however, the growth of high-quality, wafer-scale h-BN remains elusive. Some hybrid h-BN/Al(Ga)N structures have been previously reported [16], but without success in achieving EL from these structures.

1.7 Current Approaches for Growing Wide Bandgap III-Nitrides

1.7.1 AlN Substrates

Ideally, single-crystalline bulk AlN substrates would be used for building UV LED structures to minimize the lattice mismatch concerns. While the bulk growth of AlN has been developed and commercialized [80]–[83], resulting in 10^4 to 10^6 times fewer dislocations, their usability is limited by very high costs and small diameters. Furthermore, although the structural quality of this material is excellent, the optical properties are found to be lacking, including poor UV transparency. This is attributed to point defects and impurities being introduced during the physical vapor transport (PVT) process to grow AlN, where a heated solid source is sublimated at extreme temperatures (>2000 °C) onto a colder seed crystal [84], [85]. An alternative approach would be hydride vapor phase epitaxy (HVPE) [86], similar to how bulk GaN wafers are grown [87].

1.7.2 Growth of Al(Ga)N

In terms of epitaxial growth, where crystalline layers are grown over a similarly crystalline underlayer with a preservation of long-range order, most Al(Ga)N work has been achieved by metal-organic chemical vapor deposition (MOCVD). This technique is sometimes also called metal-organic vapor phase epitaxy (MOVPE). In this process, metalorganic precursors chemically react with the heated substrate to achieve growth [88]. This is a scalable process suitable for large area substrates. However, because of the growth on lattice mismatched substrates such as sapphire, thick buffer layers are required to reduce threading dislocation densities. This is shown in Fig. 1.32. Other techniques include the growth on patterned sapphire substrates (PSS) using ELO, such that the initial islands coalesce into a film [51], [89]. The control of doping, requiring the activation of Mg dopants, and unwanted impurities and second secondary reactions in the chamber have

become limiting factors of this process, particularly for Al-rich AlGaN. Nonetheless, due to the current limitations and infancy of other techniques such as molecular beam epitaxy (MBE) for the growth of wide bandgap III-Nitrides, MOCVD is at this time the technique used to achieve the highest efficiency AlGaN LEDs [53], [58], including the 275 nm emitting device with an EQE higher than 20% [90].

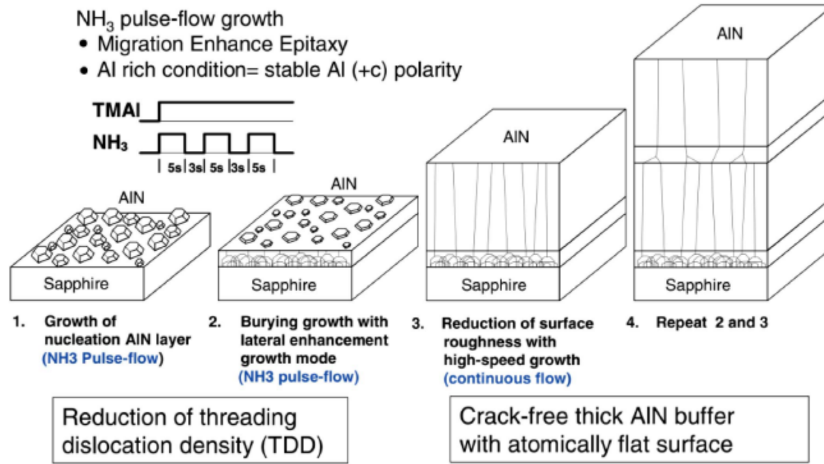

Figure 1.32 – Schematic of the growth steps of AlN on sapphire by MOCVD in order to achieve lower dislocation densities. (Source: [58])

1.7.3 Synthesis of h-BN

Most of the research involving h-BN as a 2D material is realized by exfoliation, where high quality flakes are thinned down either mechanically or chemically and transferred onto a carrier wafer. This process is however not scalable. Other reported methods include sputtering, chemical vapor deposition (CVD) and MOCVD [91]–[93]. This is shown in Fig. 1.33. Sputtering requires a subsequent annealing step to crystallize the deposited h-BN, and lacks controllability in thickness and nucleation of the material. CVD has been a promising method for the synthesis of single and few layers of h-BN on a variety of substrates. This technique is however not well suited for the growth of the other III-Nitride materials, such that heterostructures and devices cannot be

achieved. While h-BN growth has been demonstrated by MOCVD, there are similar challenges as for AlGaN. Furthermore, defects such as nitrogen vacancies and carbon impurities limit the h-BN material quality grown by MOCVD [26]. As such, while h-BN/Al(Ga)N heterojunctions have been demonstrated using this method (see Fig. 1.34) [16], including diodes, EL from such heterostructures has yet to be achieved [17], [94].

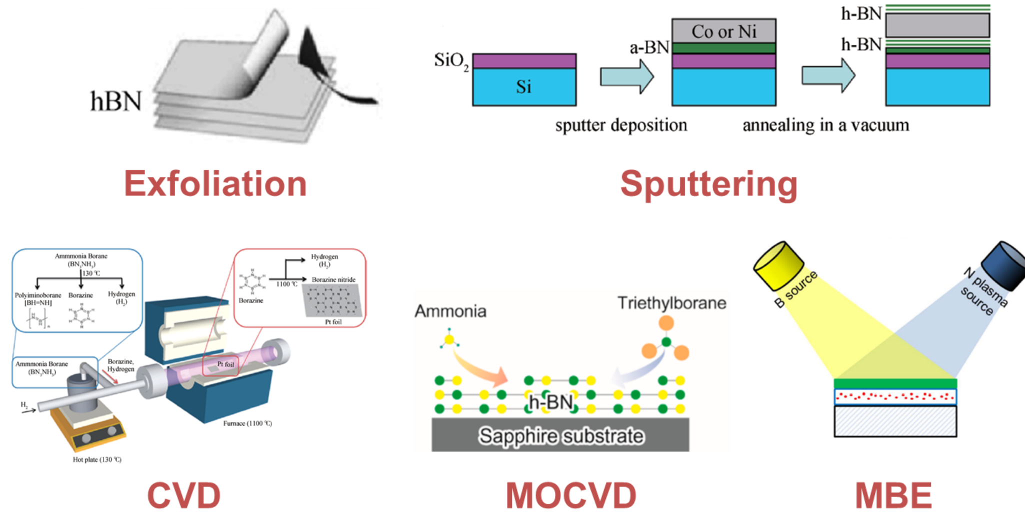

Figure 1.33 – Schematic of the various techniques used for the synthesis of h-BN monolayers and/or thin films. (Source: constructed using figures from [91]–[93])

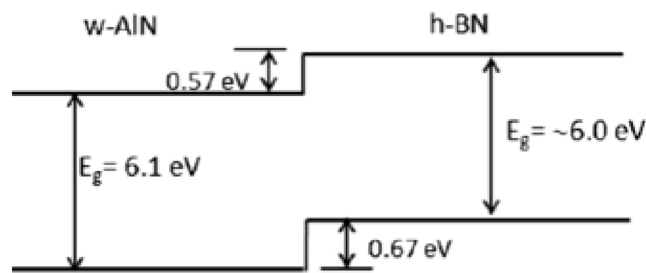

Figure 1.34 – Flat-band energy diagram of an AlN and h-BN heterojunction. (Source: [16])

1.7.4 Thermal Annealing

In order to improve the crystalline quality of wide-bandgap semiconductors, thermal annealing of samples post-growth is sometimes performed. This process causes a recrystallization of the epilayers and the rotation of the different grains to achieve longer-range ordering [95], [95], [96]. However, this process can become less effective for thicker films. Furthermore, this high-temperature annealing process can at the same time degrade certain material properties, for example by causing surface roughening [97].

1.8 Dissertation Overview

The objective of the work presented in this thesis is to develop platforms for the next generations of deep-UV optoelectronic devices, by attempting to answer and address the challenges described in this first chapter. **Chapter 2** is an overview of the growth and characterization methods that were employed to conduct the experiments presented in the subsequent chapters. Improving the growth process of AlGaN with higher Al compositions to obtain superior material quality is the outcome of **Chapter 3**. This work was published in the Journal of Crystal Growth [98]. In conducting that work, it was found that the underlying AlN template quickly became a bottleneck. As such, **Chapter 4** presents a novel AlN on sapphire growth approach using a cycled in situ annealing process. At the time of writing, this work has been just accepted for publication in Applied Physics Letters. Based on the previously developed AlN nanowire homojunction LED, and the promising characteristics of BN as a deep-UV transparent p-type material, **Chapter 5** is the first demonstration of an Al(Ga)N/h-BN heterojunction LED with enhanced device performance. This work was published in Nano Letters [99]. Given these promising results of h-BN, it was then decided to look into the high-quality wafer-scale growth of this material. Its structural and optical characteristics were compared to

theoretical calculations to help understand some of its fundamental properties, as detailed in **Chapter 6**. This work was published in Optics Express [100]. **Chapter 7** expands on the studies of the material grown in the previous chapter, resulting in the first LED with h-BN electroluminescence. Finally, **Chapter 8** proposes future work extending from the results of this thesis. This includes means to further optimize Al(Ga)N epilayers for high-efficiency deep-UV LEDs, the next steps for MBE grown h-BN, and looking into incorporating B in AlGaN.

Chapter 2 Methods

2.1 Overview

A variety of methods are required for the growth and characterization of wide bandgap III-Nitrides. This chapter provides an outline of the experimental techniques that were used in the subsequent chapters of this thesis. The benefits and reasons for selecting these methods are highlighted. It is worth noting that many of these techniques are not limited to III-Nitride thin films and nanostructures, but the discussions focus on these specific uses.

2.2 Molecular Beam Epitaxy

2.2.1 Working Principle

In MBE, molecular/atomic beams from heated sources are directed towards a substrate in ultra-high vacuum (UHV). The 10^{-3} to 10^{-6} Torr pressure range is considered high vacuum, and the 10^{-9} to 10^{-12} Torr range is UHV. Table 2.1 outlines the physical properties at these different pressure ranges. The main need for UHV in MBE is to obtain a sufficiently long mean free path so that the individual molecular beams only interact once converged onto the substrate. A secondary but desired reason is to eliminate unwanted impurities and residual gases that can deposit on the substrate during the growth process, resulting in the highest purity materials.

Table 2.1 – Summary of gas molecule properties at various pressure levels, from atmospheric pressure to UHV. (Source: Agilent Technologies)

Pressure (torr)	Molecular Density (molecules/cm^3)	Molecular Incidence (molecules/cm^2/sec)	Mean Free Path (cm)	Monolayer Formation Time (sec)
760	2.47×10^{19}	3.14×10^{23}	6.7×10^{-6}	2.9×10^{-9}
1	3.25×10^{16}	4.13×10^{20}	5.1×10^{-3}	2.2×10^{-6}
10^{-3}	3.25×10^{13}	4.13×10^{17}	5.1	2.2×10^{-3}
10^{-6}	3.25×10^{10}	4.13×10^{14}	5.1×10^{3}	2.2
10^{-9}	3.25×10^{7}	4.13×10^{11}	5.1×10^{6}	2.2×10^{3} (37 min)
10^{-12}	3.25×10^{4}	4.13×10^{8}	5.1×10^{9}	2.2×10^{6} (25.5 days)

Unlike MOCVD where a chemical reaction occurs, MBE is a physical deposition method where the crystal growth takes place on the heated substrate through an interplay of thermodynamics and surface kinetics, as illustrated in Fig. 2.1 [101]. While MBE is not in thermodynamic equilibrium, the miscibility of various materials, such as dopants, and whether alloys can grow without phase separation are part of the thermodynamic considerations [102], [103]. Since MBE effectively occurs one atomic layer at a time, the surface effects of the adatoms, such as nucleation, diffusion, adsorption and desorption therefore dictate how the layers are grown.

The three primary modes of epitaxial growth are Frank-van der Merwe, Stranski–Krastanov and Volmer-Weber [104]. In the Frank-van der Merwe mode, adatoms attach to the surface such that the growth is layer-by-layer (2D), which is the ideal mechanism for thin films. The Volmer-Weber mode forms isolated islands, since the interactions between adatoms are stronger than with the surface. This three-dimensional (3D) growth process is useful to form nanowires. The Stranski–Krastanov mode is an intermediary layer-plus-island process that begins with a wetting layer that is strained and above the critical thickness will transition to an island-based growth. Semiconductor quantum dots form through this mechanism [105].

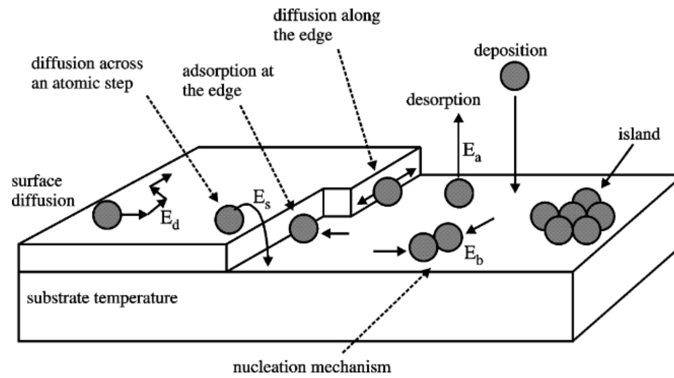

Figure 2.1 – Illustration of the various adatom behaviors and surface interactions during the growth process. (Source: Technische Universität Kaiserslautern)

2.2.2 System Configuration

A schematic of a typical MBE growth chamber is shown in Fig. 2.2(a). The primary components include the substrate heater (up to ~1000 °C), which as mentioned is necessary for crystalline growth, the substrate manipulator that continuously rotates in the azimuthal direction (CAR) to promote uniform temperature and growth, and a reflection high-energy electron diffraction (RHEED) system for in situ monitoring that will be described in a following section. Other than the UHV pumps, such as cryopumps and ion pumps, the chamber is surrounded by cryopanels filled with liquid nitrogen that provide cooling, both to eliminate thermal crosstalk between sources and act as a pump for residual gasses in the chamber. Ionization Gauges are used to measure the low pressure (high vacuum) inside the chamber. In order to maintain the UHV integrity, samples are loaded and baked (~200 °C) in a separate load-lock, and then further outgassed (~600 °C) in the preparation chamber prior to being transferred to the growth module. Importantly, the sources are equipped with individually controlled shutters that can blank the beam from each source. The shutter actuation time is less than 1 second, which is on the same order or faster than the growth time of a monolayer.

For the growth of III-Nitrides, the group-III materials (Al, Ga, In) and dopants (Si, Mg) are each loaded in their high-purity (99.9999% or higher) elemental form into the crucible of a Knudsen cell, shown in Fig. 2.2(b), which is an effusion evaporator. The crucibles are almost always made of pyrolytic boron nitride (PBN), a high-temperature and chemically resistant ceramic. Each effusion cell can be controllably heated until the material sublimates forming the molecular or atomic beam. A higher source temperature will increase the beam flux, with the ranges varying based on the vapor pressure of the specific materials. Because nitrogen is stable in the form of N_2 gas, the MBE systems used in this work are radio-frequency (RF) plasma assisted. They are equipped with a plasma source, which takes in ultra-high-purity N_2 gas (6N purity) and generates active radicals (N*) that can contribute to the growth reaction.

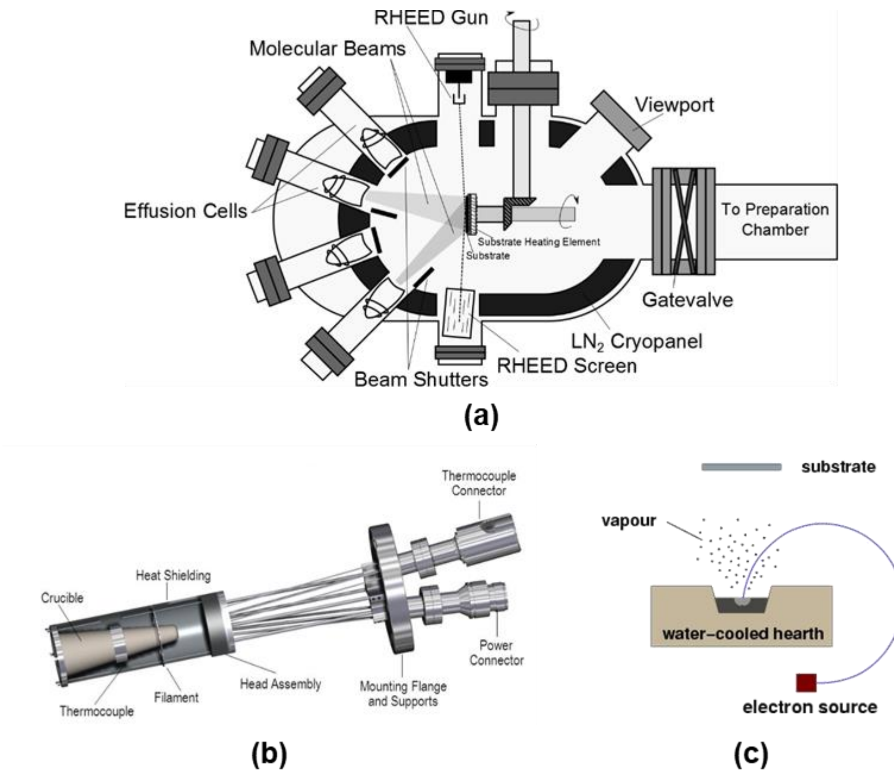

Figure 2.2 – (a) Schematic of the growth chamber of an MBE system. (Source: Wikipedia.org) (b) Schematic of an effusion source for MBE. (Source: Veeco Instruments Inc.) (c) Schematic of an e-beam evaporator. (Source: University of Cambridge)

The two commercial MBE systems used for the works presented in this thesis are the Veeco GEN 930 and Veeco GENxplor, pictured in Fig. 2.3. The former is a traditional plasma-assisted system for III-Nitride growth. The latter is additionally equipped with an ultra-high temperature (UHT) substrate heater (rated up to 1850 °C) and an integrated e-beam evaporator (see Fig. 2.2(c)) as a source for high-temperature materials such as B that are incompatible for use in traditional effusion cells. Unlike the resistive heater of the effusion cell, an e-beam evaporator focuses an electron beam onto a target material causing it to locally heat up to high temperatures and evaporate or sublimate.

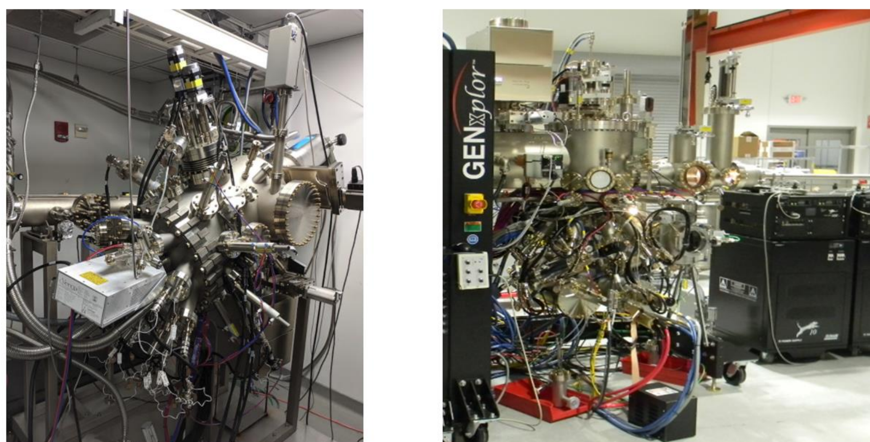

Figure 2.3 – Photographs of the Veeco GEN 930 (left) and GENxplor (right) systems used to conduct the sample growths as part of this thesis.

2.2.3 Growth Parameters

As mentioned, the substrate temperature (also referred to as the "growth" temperature) is essential for crystalline growth. Otherwise, the materials would simply deposit onto the substrate in polycrystalline or amorphous form. The UHT heater adds the possibility of annealing the grown materials while in the chamber. The nitrogen flow and RF power of the plasma source define the contribution of active nitrogen at the substrate surface. The beam fluxes, controlled by the

temperature of the effusion cells or the e-beam emission current, define the rate of the other atoms reaching the substrate. As such, it is possible to control whether the growth is N-rich, metal-rich or close to stoichiometric. Lastly, the growth duration maps to layer thickness based on a calibrated growth rate under given conditions. It is therefore important to realize that only a handful of parameters can be varied in MBE growth.

2.2.4 Benefits of MBE

Based on the working principles of MBE, several benefits of using this method become apparent especially for the growth of wide-bandgap semiconductors. The UHV environment and high purity sources produce materials with the least amount of unwanted impurities. These can result in trap states leading to nonradiative or defect-related transitions between the conduction and valence bands. The vacuum environment also allows for in situ monitoring, such that certain growth parameters can even be dynamically adjusted as the growth progresses. The relatively slower growth rates and shutter actuation times allow for atomic layer precision, useful in forming abrupt or controlled interfaces. MBE has also had better results in the p-type doping of Al-rich AlGaN. MBE is a scalable process, where recipes can be transferred from research-grade chambers to production systems that can handle larger substrates and have multi-wafer throughput. Last, in the case of III-Nitride growth, none of the source materials are toxic, nor are there any hazardous residues from the growth reaction. For these reasons, MBE should in principle be an ideal method for the growth of Al(Ga)N and BN.

2.2.5 Challenges of MBE

While MBE growth promises superior material quality, thus far this has not been the case for the wide bandgap III-Nitrides. Limitations include the conventional substrate heater temperature capabilities [97] and difficulty in evaporating B for controlled BN growth [106]. With

comparatively slower growth rates, it is also more challenging to grow thick buffer layers on lattice mismatched substrates. The growth of wide bandgap AlGaN [107] and h-BN [108] by MBE has also not been as extensively studied compared to MOCVD and CVD, respectively.

2.3 In Situ Characterization

2.3.1 Reflection High-Energy Electron Diffraction

As mentioned, the MBE growth chamber can be equipped with a RHEED system, consisting of an electron gun and phosphor screen on the opposing end. The gun is oriented at a very shallow glancing angle with respect to the sample, making RHEED a very sensitive surface monitoring technique [109]. The high-energy (~15 keV) electrons reflect off substrate surface and strike the screen displaying the diffraction pattern that is indicative of the surface crystallinity. For example, a crystalline surface will form a well-defined pattern, while a polycrystalline surface will result in arcs because of the random grain orientations. In the extreme case of an amorphous surface, a haze will appear instead of a diffraction pattern. The RHEED patterns also provide useful feedback of the surface morphology before, during and after growth. If the surface is smooth, the patterns appear streaky [5], and certain surface reconstruction patterns can be observed. If the surface is rough, the streaks will be broadened and spotty.

2.3.2 Beam Flux Monitor

The beam flux monitor (BFM) is an ionization gauge that can be placed at the substrate growth position to get a measurement of the beam fluxes in beam equivalent pressure (BEP). This is achieved by subtracting the pressure values read by the BFM gauge when a source shutter is opened and closed. This is then repeated at various source temperatures and for all the sources. Although the measured units are not of true atomic flux but of pressure (Torr), BFM measurements

are an extremely convenient and reliable technique to monitor the health of the effusion cells and flux repeatability between growths. Although not perfect, as the BFM configuration can vary, it is also useful when transferring flux conditions between different systems.

2.3.3 Electron Impact Emission Spectroscopy

In the case of the e-beam evaporator, electron impact emission spectroscopy (EIES) is used to measure and adjust or maintain the deposition rate by tuning the emission current of the e-beam filament. As a material is being evaporated, some of the vapor flux passes through the window of the sensor head and is excited by electrons generated by a filament inside the sensor [110]–[112]. The electron collisions lead to the emission of photons with wavelengths corresponding to the atomic emission lines of the evaporated material. By focusing on a wavelength unique to that material using a narrow bandpass optical filter, the intensity measured by a sensitive photodetector can then be calibrated to an evaporation rate. Compared to a quartz crystal monitor (QCM) traditionally used for this purpose, the EIES sensor is more sensitive to low deposition rates, is compatible with co-deposition processes, and does not require breaking vacuum to regularly replace the quartz crystal.

2.3.4 Optical Pyrometry

The substrate heater temperature is measured by a thermocouple. Because of the vacuum environment, however, the thermocouple reading may not be directly representative of the substrate surface temperature, since they are not in direct contact with each other. As a secondary validation of substrate temperature, an optical pyrometer is installed at a viewport normal to the substrate to measure its temperature based on the thermal radiation being emitted [113], [114]. While there are several limitations to this technique that one needs to be cautious of, it is

nonetheless useful in measuring and compensating for thermocouple offsets that can occur between growths, ensuring better repeatability between samples.

2.3.5 Residual Gas Analyzer

The residual gas analyzer (RGA) is a small mass spectrometer that is sensitive to lower mass atoms such as gases [115]. It is therefore able to identify the constituent residual gases present in the growth chamber. While not used during growth, the RGA can validate beforehand that all the impurity gases such as oxygen (for a nitride system) are below a certain acceptable limit, typically 10^{-12} Torr. It is also useful in finding possible vacuum leaks in the chamber.

2.4 Structural Characterization

2.4.1 Optical Microscopy

Optical microscopes (OMs) are useful to magnify onto the sample surface to see features such as Ga or Al droplets or cracks that cannot be seen by eye. It is also useful during the device fabrication steps to ensure the lithography and contact metallization steps are successful.

2.4.2 Scanning Electron Microscopy

The SEM produces an image of the sample by focusing and raster scanning a beam of electrons, and in the most general case detecting the secondary electrons emitted by the atoms being excited by the electron beam. Based on the secondary electron intensity, an image can be generated. Compared to the optical microscope, the electron microscope is not as diffraction limited and can therefore resolve features at much higher magnification, while still providing a good depth of field.

Energy dispersive X-ray spectroscopy (EDS) can be performed on a sample in SEM for chemical microanalysis, such as elemental composition, if a system is equipped with a suitable

detector. This technique consists in detecting X-rays that are emitted from the sample being bombarded by the electron beam. A spectrum or mapping of specific elements can be measured.

2.4.3 Scanning Transmission Electron Microscopy

As opposed to SEM, in scanning transmission electron microscopy (STEM) images are formed by electrons passing through the sample. This however requires the sample to be sufficiently thin. By focusing the electron beam to a very fine spot and additional aberration correction, STEMs can produce atomic-resolution images, which can provide highly beneficial information about the epitaxial layers and interfaces. STEM systems are also capable of spectroscopy. By measuring the energy loss by some of the electrons passing through the sample due to inelastic scattering, electron energy loss spectroscopy (EELS) enables chemical and elemental mapping [116].

2.4.4 Atomic Force Microscopy

Atomic force microscopy (AFM) in tapping mode is based on the interaction of a sharp tip at the end of an oscillating cantilever interacting with the sample surface. Depending on the forces acting on the tip when it is interacting with the surface, the cantilever oscillations will change [117]. This is measured by detecting and tracking an aligned laser beam reflecting off the cantilever. AFM is therefore useful in producing a topology image of the sample surface with sub-nm height resolution. These images can then be used to quantitatively characterize properties such as step heights and surface roughness.

2.4.5 X-Ray Diffraction

Because a crystalline lattice consists of regular arrays of atoms, a beam of incident X-rays will scatter and create diffraction spots at the detection end, and the diffraction curves (X-ray

intensity versus angle) can be obtained by rotating the sample and/or the detector [118]. For the purpose of thin films, the rocking curve (intensity versus the Omega angle) peaks are useful in characterizing the crystalline quality of the material by looking at the peak width. The coupled scan (intensity versus Omega-2Theta) is useful in determining the composition of an alloy such as AlGaN based on the peak angle between that of GaN and AlN. It is worth noting that the X-ray beam has a penetration depth on the order of microns. As such, X-ray diffraction (XRD) is useful in characterizing the bulk structural properties of the sample.

2.4.6 Raman Spectroscopy

This technique allows the determination of vibrational modes of the molecules constituting the sample. By shining a laser onto the sample, the photons will interact with the phonons or other excitations and therefore undergo Raman scattering [119]. As a result, the photon energy will be shifted up or down and a spectrum can be obtained of the Raman shifts (in cm^{-1}). This can be useful in for example identifying the different polymorphs of BN, as well as characterizing material properties such as strain and crystallinity. Combined with a microscope and movable stage, micro-Raman can be used to form a map of the sample.

2.4.7 X-Ray Photoelectron Spectroscopy

X-ray photoelectron spectroscopy (XPS) is achieved by exciting the sample surface with single energy X-rays (such as from an Al k-α source) in UHV, causing photoelectrons to be emitted. The binding energy of these photoelectrons can be measured, and the peak positions and intensities can be used for element identification, composition analysis and chemical state analysis [120]. Since photoelectrons only escape from the very top surface, the analysis depth for this technique is ~5 nm.

2.4.8 Auger Electron Spectroscopy

Auger electron spectroscopy (AES) is a similar technique as XPS in providing elemental and chemical state analysis of the sample surface but using a focused electron beam to excite the sample, causing Auger electrons to be emitted from the sample's top surface [121]. Quantitative elemental analysis can then be performed based on the kinetic energy and intensity of the Auger peaks. Unlike XPS, because the electron beam can be tightly focused, AES has the additional capability of surface mapping.

2.4.9 Secondary Ion Mass Spectrometry

Secondary ion mass spectrometry (SIMS) consists in bombarding the sample surface with a primary ion beam and collecting and analyzing the ejected secondary ions from the sample itself using a mass spectrometer. By calibrating the tool based on standards, it is possible to quantitatively analyze the elemental composition of the surface [122]. While SIMS is a destructive method, because the primary ions are effectively sputtering the surface, this can be used beneficially to obtain a depth profile of the sample.

2.5 Optical Characterization

2.5.1 Photoluminescence Spectroscopy

PL measurements consist in optically exciting a light-emitting sample and measuring its emission spectrum. Since the excitation energy needs to be greater than the bandgap of the sample, for the wide-bandgap samples in this work, a 193 nm ArF excimer laser was used, along with UV-grade optics and a UV-sensitive charge-coupled device (CCD) detector [123]. An advantage of this technique is that it can be performed on an as-grown sample without additional processing.

Power-dependent measurements, by varying the excitation laser power, are useful in characterizing changes in the sample's light-emitting properties.

Similarly, by loading the sample into a cryostat, temperature-dependent measurements can be performed from room temperature down to ~20 K using for example a closed-loop helium compressor. At cryogenic temperatures, broadening effects are reduced such that the spectral linewidth of the peaks is reduced, allowing to characterize localized states, excitonic states, coupling effects and carrier transport processes [124]. In addition, by assuming a near-unity IQE at 20 K due to the suppression of nonradiative states and defects, the IQE of the sample can be estimated by taking a ratio of PL intensities at room and low temperatures. While this method is known to be inaccurate, it remains useful in comparing the relative IQE between different samples. Fig. 2.4 is a photograph of the UV-optimized setup used for most of the PL measurements in this thesis. Appendix E includes additional setup schematics.

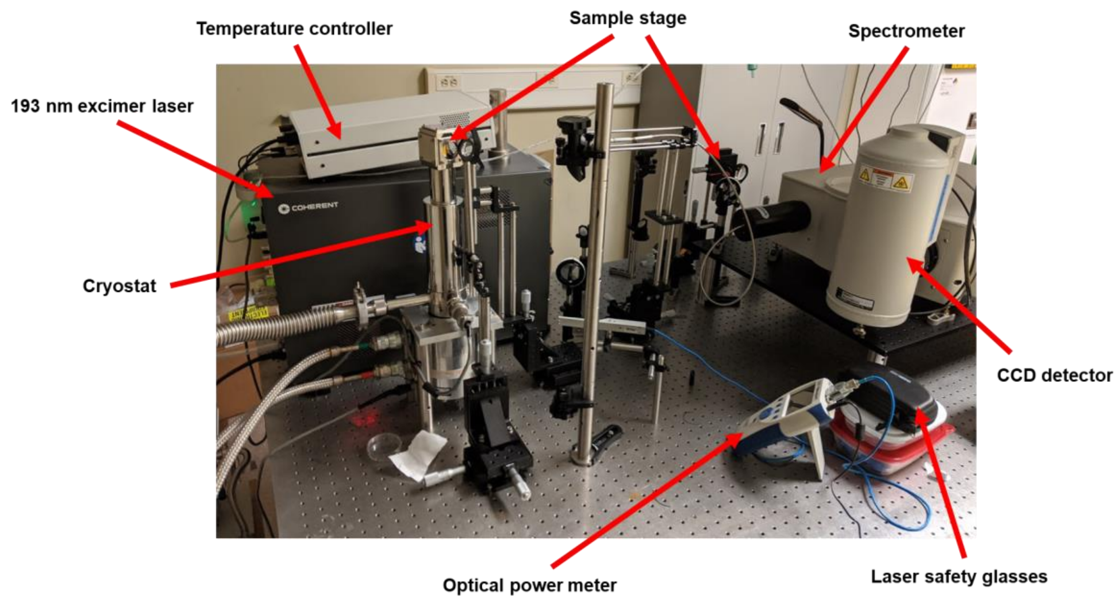

Figure 2.4 – Photograph of a UV-optimized PL setup. The labels identify the major components. A number of optical components such as mirrors and lenses are used to direct the optical path.

Polarization-resolving PL consists in collecting the in-plane emission from the sample (i.e. from the side facet) and measuring the intensity after passing it through an optical polarizer [60], [125], [126]. This is schematically shown in Fig. 2.5. The polarizer is mounted on a rotation stage such that the PL intensity can be measured at various angles, where 0° and 180° would only capture TE polarized light, and 90° and 270° for TM polarized light. This setup should first be calibrated by using an unpolarized light source and a second polarizer with known properties. To compensate for misalignments of the optical components, the spectra intensities can then be corrected with cosine functions. The degree of polarization (*P*) is calculated using Equation 2.1, by relating the TE and TM intensities (*I*).

$$P = \frac{I_{TE}-I_{TM}}{I_{TE}+I_{TM}} \quad \textit{(Equation 2.1)}$$

A value of *P* of 0, 1 and -1 are indicative of unpolarized, purely TE and purely TM polarized light, respectively.

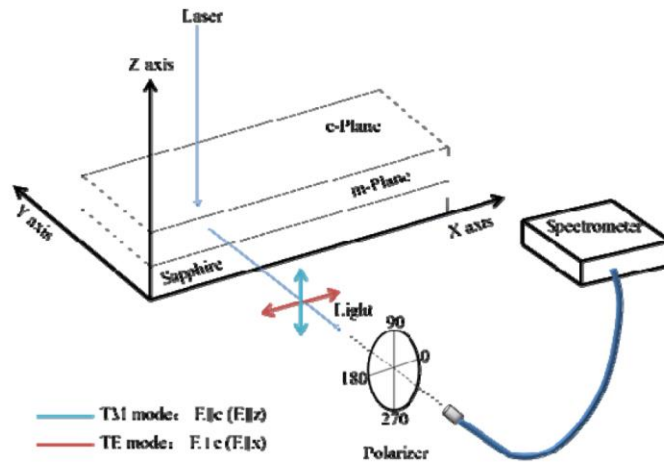

Figure 2.5 – Schematic of the setup to experimentally measure polarization-resolving PL. (Source: [125])

2.5.2 Spectroscopic Ellipsometry

This technique reflects elliptically polarized light off the sample and measures the polarization changes as an amplitude ratio and phase difference [127]. Spectroscopic ellipsometry measures these parameters over a continuous range of wavelengths. Based on this measurement, film thicknesses and optical constants such as refractive index can be extracted. This is achieved by fitting the data to an empirical model constructed using for example Cauchy's equation.

2.5.3 Ultraviolet–Visible Spectroscopy

Ultraviolet-visible (UV-Vis) consists in passing a broadband light beam through the sample to measure its absorbance (or equivalently transmittance) by comparing the light intensity at every wavelength before and after it passes through the sample. In the case of thin films on sapphire substrate for example, the obtained absorbance spectrum needs to be baseline corrected with that of bare sapphire. This measurement is useful in determining below what wavelength a layer will start becoming absorptive, which can also then be related to the optical bandgap.

2.6 Electrical Characterization

2.6.1 Hall Effect Measurement

Hall effect measurements consist in having a current flow (j_x) through a piece of semiconductor in the x direction and applying a perpendicular magnetic field (B_z) in the z direction. This causes the electrons (or holes) to deflect towards one edge, resulting in an electric field (E_y) in the y direction [1]. The van der Pauw method consists in placing four ohmic contacts and measuring the resistivity and Hall coefficient (defined in Equation 2.2) [128]. From there, the resistivity of the material, doping type, majority charge carrier density and mobility of the majority carrier can be calculated. As a reminder to the reader, the relation between conductivity (σ) is the

product of elemental charge (q), carrier concentration (n) and carrier mobility (μ). Resistivity (ρ) is $1/\sigma$.

$$R_H = \frac{E_y}{j_x B_z} \qquad \textit{(Equation 2.2)}$$

2.6.2 Current–Voltage Characteristic

As its name states, this measurement consists in sweeping the bias voltage of the device and measuring the electric current. In the case of an LED device, the *I-V* curve validates whether the device is exhibiting the rectification characteristic of a diode. From the *I-V* curve, the leakage current in reverse bias, turn-on voltage and breakdown voltage can be determined. The ideal diode equation (Equation 2.3) gives the *I-V* characteristic of an idealized diode [129].

$$I = I_0\left(e^{\frac{qV}{kT}} - 1\right) \qquad \textit{(Equation 2.3)}$$

I is the current flowing through the diode, I_0 is the leakage current, V is the applied (bias) voltage, q is elementary charge, k is Boltzmann's constant and T is temperature.

2.6.3 Electroluminescence Spectroscopy

This technique is comparable to PL spectroscopy, but instead of optical excitation, an electric current is injected into the device. For this, the sample needs to have ohmic contacts. The setup used for the measurements presented in this thesis includes a source meter used to apply the bias voltage and measure the current, and the devices are probed on wafer using micromanipulators and needle tips. A UV-transmissive optical fiber is used to collect the light emission from the device. The other end of the fiber is directed into the same spectrometer used for PL measurements equipped with the UV-sensitive CCD detector. Appendix E includes a schematic of this setup.

Chapter 3 Molecular Beam Epitaxy and Characterization of $Al_{0.6}Ga_{0.4}N$ Epilayers

3.1 Author Contributions and Copyright Disclaimer

The contents of this chapter were published in Elsevier's Journal of Crystal Growth in February 2019 [98], for which I retain the right to include it in this thesis/dissertation, provided it is not published commercially. The co-authors were Xianhe Liu, Ayush Pandey, Walter Jin Shin, Eric T. Reid, Kishwar Mashooq and Zetian Mi from the University of Michigan, and Mohammad Soltani from Raytheon BBN Technologies. X. L. has a joint affiliation with McGill University. I designed, conducted and authored most of the work. X. L. and A. P. contributed to the material growth process. W. J. S. conducted the PL measurements. E. T. R. and K. M. contributed to some of the other characterization. The work was supervised by Z. M., who contributed to the design of the experiments with M. S. as part of a collaboration. M. S. further collaborated with the Harvard University Center for Nanoscale Systems for assistance with TEM characterization of the samples. This work was supported by the Office of the Director of National Intelligence (ODNI), Intelligence Advanced Research Projects Activity (IARPA), via Raytheon BBN Technologies Corp. contract number 2017-17063000002. D. A. Laleyan received financial support by the Natural Sciences and Engineering Research Council of Canada (NSERC) with award PGSD3-502905-2017.

3.2 Background and Motivation

Al-rich AlGaN, with Al compositions varying from ~50-90% are required for LEDs and lasers operating in the UV-B (280-315 nm) and UV-C (100-280 nm) bands, solar-blind avalanche

photodiodes and phototransistors, and integrated UV photonics [53], [58], [89], [130]–[132]. Al-rich AlGaN also possesses a significantly larger breakdown field than GaN [133], and is promising for future high-power electronic devices. For many of these applications, it is essential that relatively thick AlGaN layers (>0.5 μm) with atomically smooth surface and with a minimal level of defects and dislocations can be epitaxially grown on foreign lattice-mismatched substrates, which are lower cost, larger size and more widely available than bulk GaN or AlN substrates [134]–[136]. To date, most studies on the epitaxy of Al-rich AlGaN have been performed by MOCVD [53], [89], [137]–[144]. There have been few reports on the demonstration of high quality, Al-rich AlGaN epilayers by MBE, which offers unique advantages, including reduced impurity (carbon, oxygen) incorporation, more efficient p-type dopant (Mg) incorporation [145], [146], and a precise control of the alloy composition [147]–[149].

Much progress has been made in the past decade in obtaining UV LED devices in the 210-400 nm range with external quantum efficiencies between 1 and 10% most significantly due to an improvement in AlGaN material quality [53], [89], [150], [151]. This was achieved by utilizing buffer layers to reduce threading dislocation densities (TDDs), annealing the sample, employing more advanced growth techniques such as epitaxial lateral overgrowth, pulsed and migration-enhanced epitaxy, multistep buffers, and superlattice structures acting as dislocation filters [53], [58]. Such techniques can however cause alloy clustering, affecting the composition of the AlGaN epilayers, which is already an issue due to Al segregation around dislocations [57]. Moreover, the conventional MOCVD process is often limited by parasitic reactions between Al-metalorganic precursors and the nitrogen gas source (NH_3) [53], [140]. More generally, the larger sticking coefficient and lower surface mobility of Al adatoms make AlGaN epilayers more difficult to grow in a smooth layer-by-layer manner, instead causing the formation of islands, step bunching and

hillocks [58], [152], [153]. As such, while atomically smooth root mean square (RMS) roughness has been reported for AlN and GaN (0.2 nm) [153], [154], this value is closer to 1 nm for AlGaN [141], [149], [152], [153]. Employing higher growth temperatures (>1100 °C for MOCVD) enhances Al adatom migration and inherently improves material quality [141], [155], but also causes Ga adatom desorption and film decomposition, reducing the growth rate and making alloy composition tuning less controllable [140], [156]. The growth kinetics of MBE pose a similar issue due to the stronger bonding energy of Al-N versus Ga-N, such that Al is completely incorporated in the film, whereas Ga acts as a surfactant and its incorporation depends on the remaining N atoms [107], [147], [157]. However, by growing in slightly Ga-rich conditions, the thin liquid-metal layer at the surface promotes lateral adatom migration, such that smooth high-quality nitride films can be obtained without requiring excessively high growth temperatures [107], [157]. Although the MBE growth of AlGaN films with low [158], medium [147], [159] and high [148], [149] Al composition have been reported in the past, there are few studies on the optimal conditions for high-quality Al-rich AlGaN films, effects of the different growth parameters, and resulting structural and optical characteristics.

In this work, we report a detailed study of the MBE growth and characterization of relatively thick Al-rich AlGaN epilayers on AlN templates on sapphire substrate. We have demonstrated that the alloy composition can be precisely controlled by tuning the Al flux and N flow rate, and an atomically smooth surface morphology can be achieved by carefully controlling Ga flux and growth temperature. Under optimized conditions, the AlGaN epilayers (>0.5-μm thick) exhibit a surface roughness <0.4 nm, and strong PL emission at room temperature. High resolution TEM studies further suggest that, despite the lattice mismatch between AlGaN and AlN [152], the formation and propagation of dislocations is significantly suppressed by incorporating

superlattices with sub-nm thicknesses. The refractive index of $Al_{0.6}Ga_{0.4}N$ is further measured to be ~2.20 at the 400 nm wavelength. The realization of high-quality Al-rich AlGaN offers the distinct opportunity for developing efficient mid and deep UV optoelectronic devices, integrated UV photonics, and high-power electronics.

3.3 Growth of Al-Rich AlGaN Epilayers

Al-rich AlGaN epilayers were grown on commercial 1-μm thick wurtzite AlN template on *c*-plane sapphire substrate (DOWA Electronics Materials Co., Ltd.) using a Veeco GEN 930 RF nitrogen plasma-assisted MBE system equipped with Al and Ga SUMO effusion sources. The AlN template wafer was diced into 1 cm^2 pieces, which underwent a standard solvent degreasing procedure prior to loading into the MBE chamber. To allow for efficient and repeatable heat conduction in vacuum, the wafer backside was metallized with molybdenum, and the substrate pieces were mounted onto a 3-inch Si carrier wafer using indium solder. It was confirmed by optical pyrometry that the substrate temperature was uniform across the carrier wafer, remained constant throughout the growth, and was similar between growth runs. Prior to initiating the growth, the substrate was ramped up 100 °C higher than the AlGaN growth temperature for thermal cleaning of the surface and soaked with the nitrogen plasma. Under these conditions, a thin, 20 nm AlN buffer layer was grown to promote a better growth interface between the AlN template and subsequent AlGaN film. The Al-rich AlGaN films were grown at an effective surface temperature of 700 °C, calibrated using the 7×7 to 1×1 surface reconstruction of Si(111). A low nitrogen flow rate of 0.3 sccm was used at a constant RF plasma forward power of 350 W. The Al and Ga fluxes in beam equivalent pressure were kept at 3×10^{-8} and 1×10^{-7} Torr, respectively. Under these conditions, a growth rate of 80 nm/hour is achieved. The growth of AlGaN was conducted under slightly metal-rich conditions. The buildup of excess metallic Ga in the form of droplets can

be minimized, or avoided, by carefully monitoring the RHEED pattern and adjusting the growth conditions accordingly, either through periodic interruptions of the source-metal beam fluxes [147], or by fine tuning the Ga flux dynamically. In both cases, it is essential to maintain a streaky pattern, shown in Fig. 3.1(a), which is indicative of two-dimensional epitaxial growth [160]. In this study, we focus on the characterization of AlGaN epilayers that incorporated periodic interruptions of the source-metal beam fluxes. The modulation sequence for these samples includes ten seconds of interruption of the Al and Ga beams for every five minutes of growth. With shorter interruptions, an increase in intensity of the streaky RHEED pattern, correlated to the clearing of excess metal buildup at the surface, was not observed. It was noticed that interruptions with longer durations could induce transition the growth to an unwanted nitrogen-rich regime.

We have first performed extensive studies on the MBE growth of AlGaN with various growth parameters. It is observed that the growth rate scales with Al flux. Keeping a set Al flux, the nitrogen plasma acts as the driver that most significantly impacts the surface morphology and Al composition of the $Al_xGa_{1-x}N$ films, with x increasing as the nitrogen flow rate is reduced. As is the case for other GaN-based epilayers, a nitrogen-rich growth regime results in a spotty RHEED pattern and increased surface roughness. More importantly, for a given nitrogen flow and fixed Al flux, the Al composition is pinned: increasing the Ga flux only increases the density of Ga droplets on the sample surface, while decreasing the Ga flux forms AlGaN patches rather than a continuous film along the entire surface, due to the shortage of Ga, instead of the formation of lower Al composition AlGaN epilayers. It was found that during the growth of higher Al composition AlGaN by reducing the nitrogen flow rate, the Ga flux had to be *increased* to maintain a smooth surface, likely due to the enhanced Ga adatom desorption from reduced Ga incorporation as the nitrogen active species are primarily bonding with Al at the relatively high AlGaN growth

temperature [107], [157]. As for the substrate temperature, from a systematic study we determined that it needed to be sufficiently high to sustain high-crystalline quality AlGaN growth, validated by PL and XRD characterization, but further increasing the substrate temperature only enhances Ga desorption from the surface with equivalent effects as reducing the Ga flux. Above a critical limit, ~100 °C higher than the optimal growth temperature, we see a Ga shortage even with excessively high Ga fluxes, leading to a roughened surface and degradation of crystalline quality.

3.4 Structural Characterization of the AlGaN Epilayers

Using the aforementioned conditions, ~500-nm thick $Al_{0.6}Ga_{0.4}N$ samples were grown and the bulk structural properties were characterized by XRD and TEM. XRD was performed using a Rigaku SmartLab system aligned for thin film diffraction, with the 2Theta-Omega spectrum shown in Fig. 3.1(b). The two well-defined peaks of comparable intensity at 35.4° and 36.0° correspond to AlGaN and AlN, respectively. Knowing the AlN (36°) and GaN (34.5°) peak positions, Vegard's law was used to obtain an Al content of x = 0.6 for this $Al_xGa_{1-x}N$ sample [141], [148], [158], [161], [162]. The validity of this interpolation was confirmed by the Al/Ga atomic ratio measured by SIMS analysis (EAG Laboratories) for a different sample where the different stacked layers had compositions of $x \approx 0$, 0.6, 0.7, 0.8 and 1, demonstrating the controllability and tunability of the growth conditions in this regime. Complete strain relaxation is assumed given the thickness of the AlGaN film and the lattice mismatch with the AlN substrate layer for this Al composition. The full width at half maximum (FWHM) of the AlGaN XRD peak is 0.12°, as compared to 0.07° for the AlN peak, which is indicative of a high-quality ternary alloy [141], [142], [163] with minimal phase separation, clusters and formation of sublayers [58], [164]. Significantly, from SIMS analysis, the carbon, silicon and hydrogen impurity incorporation are less than 3×10^{16} cm^{-3} (approaching the detection limit of the SIMS tool), 5×10^{16} cm^{-3} and 1×10^{17} cm^{-3}, respectively,

which are 1-2 orders of magnitude lower than that reported in films grown by MOCVD [156], [165], [166], and can be further reduced with more careful surface preparation and further thermal annealing.

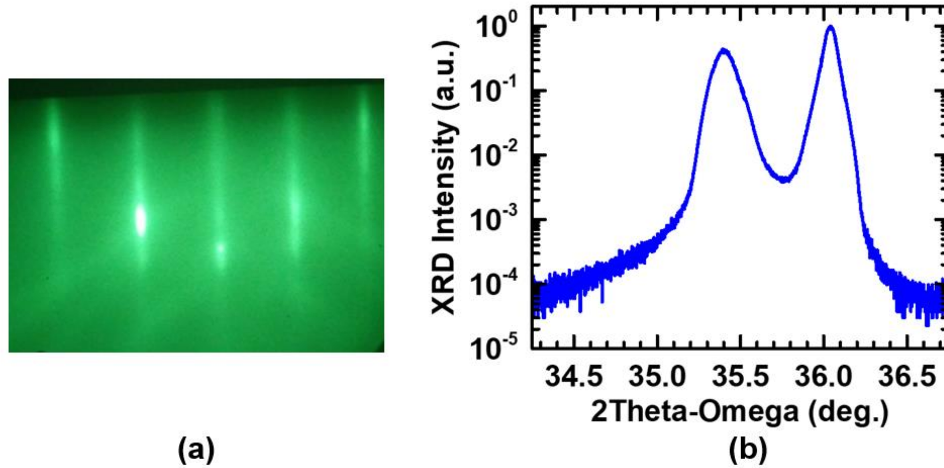

Figure 3.1 – (a) Photograph of the sustained streaky RHEED pattern during AlGaN growth. (b) 2Theta-Omega XRD scan of the $Al_{0.6}Ga_{0.4}N$ sample, showing peaks at 35.4° and 36°. The latter corresponds to the AlN template peak.

The AlGaN film was further investigated using a JEOL ARM 200F STEM operated at 200 kV. The TEM sample was prepared following standard focused ion beam (FIB) lift-out procedures using an FEI Helios 660 Nanolab FIB/SEM, followed by surface cleaning using a Fischione Nanomill 1040 Ar-ion mill operated at 500 V, to remove surface damage and Ga contamination. The STEM bright-field (BF) image at 200k× magnification of the AlN and AlGaN layer cross-section is shown in Fig. 3.2(a). The dislocations originating in the AlN template propagate in the growth direction into the AlN buffer and AlGaN layers. However, as labeled in the figure, upon reaching the AlGaN film, there is a bending of the dislocation lines [167], which in some cases leads to their convergence, grouping and annihilation, and termination; thus, leading to regions in the AlGaN film where the dislocation density is reduced with respect to the underlying AlN

template, in spite of the lattice mismatch between AlGaN and AlN [168]. The inset of this figure shows the EDS line scan taken at 200 kV accelerating voltage using an EDAX Octane windowless 100 mm detector, overlaid on the dark-field (DF) image of the AlGaN film at higher magnification, showing an Al/Ga compositional variation at the stacking interfaces caused by the interruptions during growth. It is worth noting that these interfaces have lower Al content, but are too thin to quantitatively determine their exact composition. Figure 3.2(b) is a STEM-DF image at 1.2M× magnification focusing on the AlGaN film, and showing the periodic stacking of the epilayers forming a superlattice with respect to the interfaces formed by the brief growth interruptions. The high-angle annular dark-field (HAADF) image at high magnification (30M×) and atomic resolution of Fig. 3.2(c) focuses on one of the stack interfaces in the AlGaN superlattice. It can be seen that the growth interruptions lead to a compositional variation that is limited to a sub-nanometer thickness.

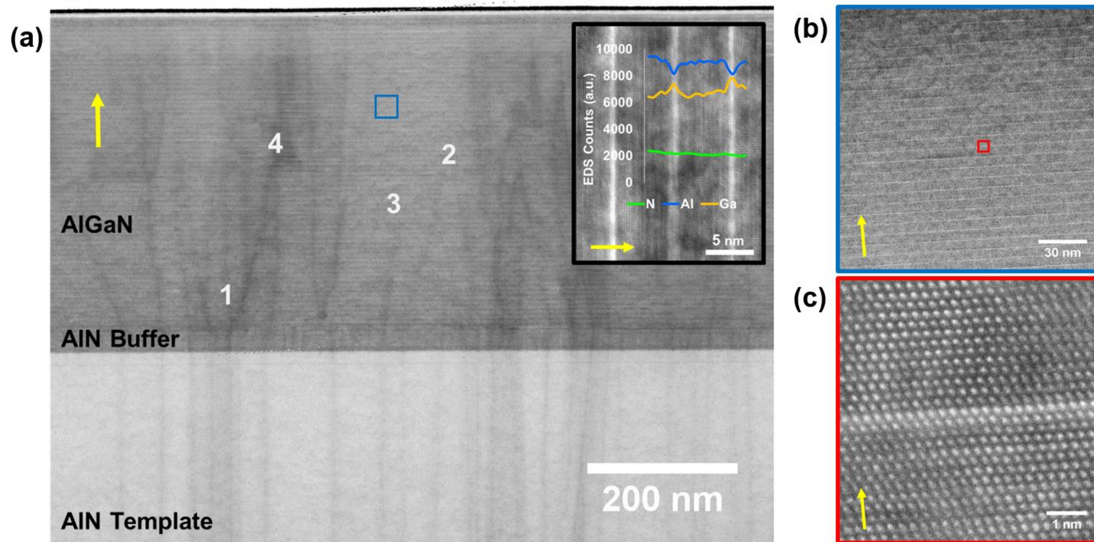

Figure 3.2 – STEM images of the sample cross-section, with the yellow arrow defining the growth direction in every case. (a) STEM-BF image at 200k× magnification, displaying the AlN template, AlN buffer and AlGaN epilayer regions, as well as the threading dislocations originating from the template and propagating into the grown film. Labeled on the figure are regions of interest highlighting the bending of the dislocations reaching the AlGaN superlattice (1), convergence of dislocations leading to their annihilation (2), termination of propagating

dislocations partly through the AlGaN (3), and grouping of several threading dislocations (4). Shown in the inset is an EDS line scan of the AlGaN superlattice, showing an Al/Ga compositional variation at the nanometer scale and under similar N presence. (b) STEM-DF image at 1.2M× magnification showing the periodic superlattice formed in the AlGaN film (boxed in blue in (a)) during growth. The periodic spacing is of ~7 nm. (c) High-magnification HAADF image (30M×) displaying the atomic-resolution stack interface of the superlattice (boxed in red in (b)). From the crystalline stacking, the interruptions during growth lead to sub-nanometer compositional variations in the AlGaN film.

The surface properties of this sample were investigated using SEM and AFM. A Hitachi SU8000 SEM was used with an acceleration voltage of 5 kV, and the sample was loaded at a 45° angle to better resolve the surface topology. Figure 3.3 shows the SEM images at low (a) and high (b) magnification. A uniform and smooth surface can be seen over a large area, with an absence of ripples or cracks commonly seen after the growth of lattice mismatched layers due to strain. The single scratch line seen in Fig. 3.3(a) was intentionally made to properly focus on and resolve the smooth surface. A Bruker Dimension Icon AFM was used in tapping mode in air to obtain the 1×1 μm^2 topology (Fig. 3.3(c)). From a section analysis (inset of Fig. 3.3(c)), the observed terraces are of atomic steps corresponding to the top 1 or 2 epitaxial monolayers that did not fully form at the end of growth [153], [169]. These also account for the surface contrast observed from SEM at high magnification. The RMS roughness of a 5×5 μm^2 area is only ~0.4 nm. These excellent surface characteristics make this AlGaN film suitable for UV photonics.

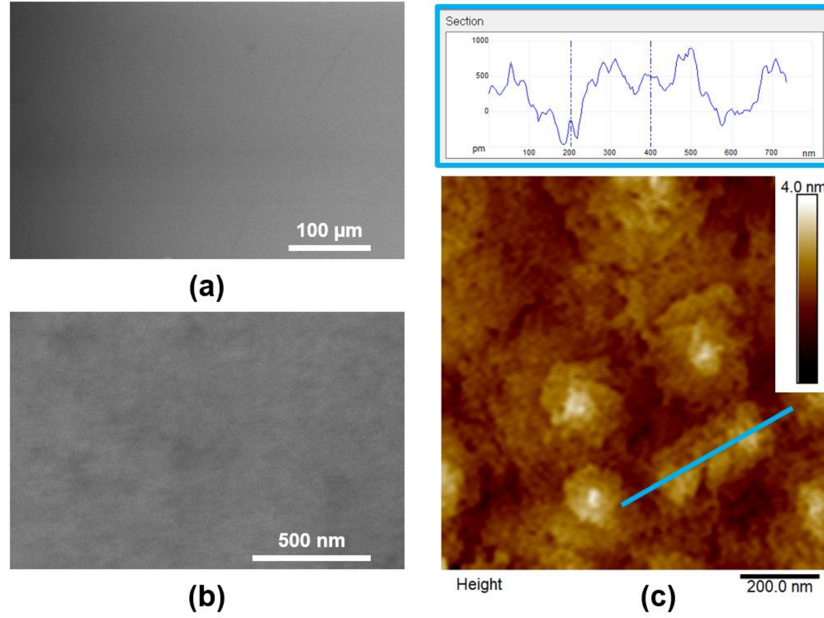

Figure 3.3 – SEM images of the sample surface taken at magnifications of 700× (a) and 200k× (b). (c) AFM height image of the sample surface of 1 µm². The inset above it is a section analysis of the terraces (identified by the blue line) showing height variations corresponding to atomic steps.

3.5 Optical Characterization of the AlGaN Epilayers

A Woollam M-2000 spectroscopic ellipsometer with high speed CCD detector covering a spectral range of 300-1683 nm was used to determine the in-plane refractive index of this AlGaN film in contrast to that of the underlying AlN. The structure model was fitted using the Cauchy relationship [170] first starting with pieces of bare sapphire and AlN template on sapphire to establish the empirical model. The expression for the Cauchy relationship to obtain the refractive index (n_r) as a function of wavelength (λ) is given in Equation 3.1, and the fitted A, B and C coefficients for the different layers are summarized in Table 3.1.

$$n_r(\lambda) = A + \frac{B}{\lambda^2} + \frac{C}{\lambda^4} \qquad \textit{(Equation 3.1)}$$

Table 3.1 - Fitted model parameters used in the Cauchy relationship to obtain the refractive index versus wavelength curves of AlGaN and AlN.

Layer	A	B	C
AlGaN	2.101	0.00961	0.00128
AlN	2.016	0.01345	0.00033165
Sapphire	1.754	0.00686	0

The fitting of the AlGaN layer had an *A* coefficient of 2.1, derived thickness of ~460 nm, consistent with the expected growth rate, and a mean squared error (MSE) of 15.2. In contrast, an *A* coefficient of 2.016 was obtained from AlN (MSE of 11.5). From Fig. 3.4, at a 400 nm wavelength, these correspond to refractive indices of ~2.20 and 2.11 for $Al_{0.6}Ga_{0.4}N$ and AlN, respectively. The curves obtained in Fig. 3.4 do not match exactly those reported in the past for AlGaN films with similar Al content gown by MOCVD or MBE [149], [161], [171], [172]. In one case, our $Al_{0.6}Ga_{0.4}N$ refractive indices are closer to that reported for $Al_{0.675}Ga_{0.325}N$ grown by MBE on Si substrate [149]. In another case where MOCVD was used, the reported refractive index contrast between AlN and $Al_{0.6}Ga_{0.4}N$ is similar to ours, but their values of n_r are 0.04 higher [172]. It is worthwhile mentioning that these previous reports indicated uncertainties in the Al compositions of $Al_xGa_{1-x}N$. In addition, the refractive index is affected by the presence of defects, strain, and alloy inhomogeneities. Given the optimized AlGaN growth and the many methods used here to characterize and validate alloy composition, the measured n_r for AlN and $Al_{0.6}Ga_{0.4}N$ in this study will serve as an important reference for the design of both deep UV light emitters and photonic circuit elements such as waveguides [173].

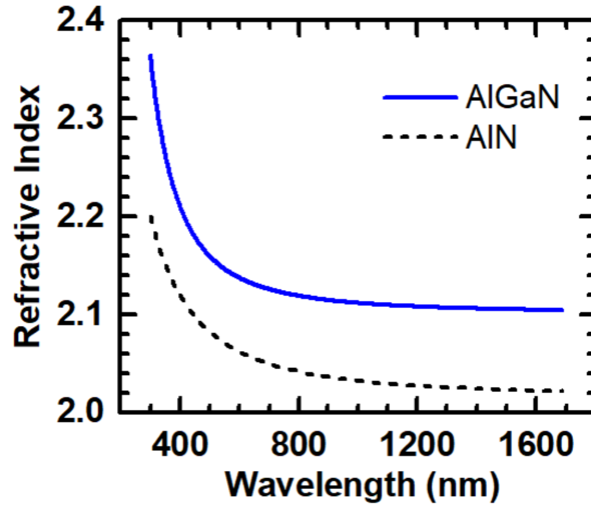

Figure 3.4 – Refractive index versus wavelength curves for $Al_{0.6}Ga_{0.4}N$ (in solid blue) and AlN (in dashed black) obtained by spectroscopic ellipsometry.

Optical properties of this sample were also characterized using variable excitation power PL spectroscopy with a 193 nm ArF excimer laser as the excitation source. The emitted photons from the samples were spectrally resolved by a Horiba iHR550 spectrometer and detected using a low-noise Symphony II CCD detector. The obtained room-temperature PL spectrum in Fig. 3.5(a) shows a single dominant peak at ~284 nm for a broad range of excitation powers. A redshift of these peaks is not observed with increasing excitation powers, indicating that there are no significant heating effects occurring in the sample, for example due to strong nonradiative recombination [174]–[176]. The FWHM of the spectrum measured at 100 μW excitation is ~14 nm, suggesting excellent optical quality [139]. It is worth noting that the emission wavelength is longer than the expected PL peak for $Al_{0.6}Ga_{0.4}N$ based on bandgap-composition relationships of AlGaN alloys [139], [142], [148], [162], [171], which may be attributed to donor-acceptor pair recombination [158] or Stokes shift [142] as observed in previous reports, or partly related to the presence of sub-nm interfaces. Figure 3.5(b) shows the temperature dependence of the integrated

PL intensity, normalized to 1, and plotted against inverse temperature. An estimated IQE of ~50% is obtained, defined as the ratio of integrated PL intensities at room and low temperatures [177], [178]. The inset of Fig. 3.5(b) is the temperature dependence of the PL spectrum under constant excitation power showing a blueshift of the dominant peak by ~1.5 nm, and the stronger prevalence of a shoulder peak at ~277.5 nm.

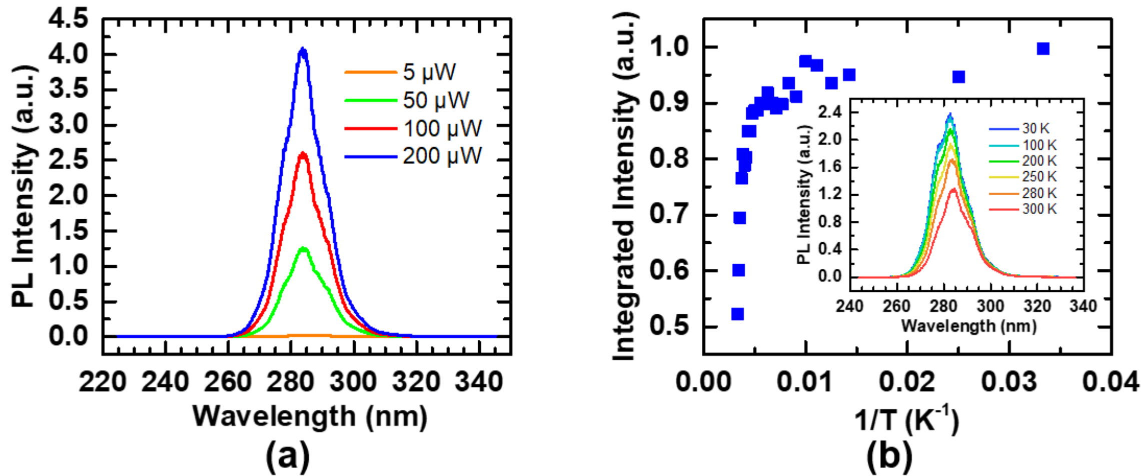

Figure 3.5 – (a) Variable excitation power PL spectra of the $Al_{0.6}Ga_{0.4}N$ sample at room temperature, showing a single dominant peak centered at ~284 nm. (b) Temperature dependence of the integrated PL intensity (normalized to 1). The inset shows the changes with temperature.

3.6 Conclusion

In conclusion, we have performed a detailed study of the MBE growth of Al-rich AlGaN, with a focus on an Al composition ~60%. By optimizing the growth conditions, $Al_{0.6}Ga_{0.4}N$ epilayers with excellent structural and optical properties can be achieved on AlN buffer on sapphire substrate. It was observed that dislocation propagation originating from the substrate layers can effectively be reduced or terminated within the stacked AlGaN epilayers with sub-nm interfaces. Further studies also suggest that AlGaN epilayers grown by MBE without such sub-nm interfaces can exhibit excellent surface morphology and optical properties, if a slightly metal-rich condition

is consistently maintained during epitaxy. These studies will contribute to the development of high efficiency mid and deep UV light emitters and integrated UV photonics.

Chapter 4 Strain-Free Ultrathin AlN Epilayers Grown Directly on Sapphire by Molecular Beam Epitaxy

4.1 Author Contributions and Copyright Disclaimer

At the time of writing, the contents of this chapter have been accepted for publication in AIP's Applied Physics Letters journal. The co-authors are Eric T. Reid, Ping Wang, Ayush Pandey and Zetian Mi from the University of Michigan, Natalia Fernández-Delgado from the University of Cádiz, and Gianluigi A. Botton from McMaster University with joint affiliation at Canadian Light Source. I designed, conducted and authored most of the work. P.W. and A. P. contributed to the material growth process. E. T. R. contributed to the sample characterization work. The work was supervised by Z. M., who contributed to the design of the experiments. N. F.-D. and G. B. performed the STEM measurements and contributed to the discussions. This work was supported by the Army Research Office (ARO) (W911NF-17-1-0109). D. A. L. received financial support by the Natural Sciences and Engineering Research Council of Canada (NSERC) with award PGSD3-502905-2017. N. F.-D. received support from Junta de Andalucía (PAI research group TEP-946) and the University of Cádiz (Promotion of Research Activity). Part of the microscopy work was carried out at the Canadian Centre for Electron Microscopy, a national facility supported by the Canada Foundation for Innovation under the Major Science Initiative program, NSERC and McMaster University.

4.2 Background and Motivation

High-quality AlN epitaxially grown on sapphire substrate is of critical importance for a broad range of applications, including mid and deep-UV optoelectronics and high power/frequency electronics [58], [89]. Also, with its wide bandgap and transparency down to ~0.2 μm wavelengths, AlN on sapphire has emerged as the material of choice for integrated UV, visible and quantum photonics, enabling a broad range of classical/non-classical applications in photonics [179]. Moreover, for high-power photonic applications, an ultrawide bandgap material such as AlN is essentially required to avoid nonlinear absorption [180]. To date, however, the quality of AlN on sapphire is severely limited by large densities of defects and dislocations [181], and undesired impurity incorporation (e.g., carbon and oxygen) [182], [183]. Currently established growth methods of AlN on sapphire, mainly by MOCVD, require the use of relatively thick buffer layers [184], [185], and techniques such as epitaxial lateral overgrowth and patterned substrates to reduce the formation of dislocations and obtain a usable AlN epitaxial template [186]–[189]. Yet, for many applications such as AlN waveguides and micro-ring resonators operating in the UV spectra, a very thin AlN epilayer is often required. Recently, with the use of ultrahigh-temperature annealing, significantly improved quality was reported for AlN deposited on sapphire by employing a sputtering method [96]. Such high-temperature annealing, however, may degrade the surface morphology and negatively impact the dopant distribution in optoelectronic and electronic devices [97], [190], [191]. MBE provides unique advantages for the epitaxy of AlN and Al-rich AlGaN, including more controlled nucleation [192], [193] and Al incorporation [98], efficient Mg dopant activation [194], and reduced impurity incorporation. To date, however, reports of high-quality AlN epilayers by MBE are lacking, largely due to the limited growth temperature of conventional systems [97], [192], [195], [196]. Recent advances in MBE substrate heater

technology, with reports of the growth of high-temperature materials such as BN [100], [108], [197], present an exciting opportunity to overcome these challenges.

This chapter reports on the molecular beam epitaxy and characterization of high-quality ultrathin AlN epilayers grown directly on sapphire. Multiple-cycle in situ high-temperature annealing was performed during the initial stage. It is observed that, with the use of in situ high-temperature annealing, the dislocation densities are significantly reduced. For ~0.1-μm-thick AlN grown directly on sapphire, the (002) linewidth measured by XRD is less than 150 arcsec, which is comparable to, or better than, epilayers grown directly on AlN substrate. Significantly, the (102) linewidth is substantially reduced from over 4000 arcsec to less than 1400 arcsec with the use of in situ high-temperature annealing. Through detailed temperature-dependent PL measurements, a luminescence efficiency ~30% is measured at room temperature. Detailed STEM studies suggest the propagation of dislocations is largely suppressed in the thin AlN epilayers grown directly on sapphire, and that the AlN layer is grown fully-strain-relaxed. Significantly improved results are further measured for AlN epilayers with increased thicknesses using this same approach.

4.3 MBE Growth of AlN Epilayers on Sapphire

AlN samples were grown on *c*-plane sapphire substrate using a Veeco GENxplor RF nitrogen plasma-assisted MBE system equipped with an Al SUMO effusion source and a NOVA ultrahigh-temperature substrate heater (up to 1850 °C). The sapphire wafer backside was metallized with molybdenum to allow for efficient heat conduction in vacuum. As schematized in Fig. 4.1(a), Stage I of growth consists of an ~80 nm-thick buffer layer using a modified migration-enhanced epitaxy (MEE) [198] approach to promote AlN nucleation and a smooth interface directly over the lattice-mismatched sapphire. The growth temperature was ~950 °C. An Al flux of 8×10^{-8} Torr in BEP, and a low nitrogen flow rate of 0.3 sccm at a constant RF plasma forward

power of 350 W were used. This corresponds to a slightly nitrogen-rich condition at this growth temperature. The shutter sequence was 1 min of Al (i.e., forcing a metal-rich surface coverage) followed by 4 min of both Al and N (i.e., nearly stochiometric AlN growth with a thin liquid-metal surface). This sequence was determined to be optimal by careful monitoring of the RHEED pattern. As highlighted in Fig. 4.1(b), in the first minutes of growth, the RHEED pattern becomes segmented and spotty due to the lattice-mismatched nucleation (Pattern I), but quickly starts recovering to a streakier pattern, indicative of two-dimensional epitaxial growth [192], [196] within the third modulation loop. The RHEED pattern is streaky by the end of this first buffer stage (Pattern II), during the sixth modulation loop. Afterwards, as Stage II of growth, the substrate temperature is gradually raised to ~1550 °C and the sample is in situ annealed for 30 min under the same nitrogen plasma environment. It was found that this annealing step is critical for promoting a recrystallization of the buffer layer and obtaining significantly higher quality AlN epilayers in the later stages of growth. During this high-temperature annealing process, there is decomposition of the AlN buffer even in the presence of the nitrogen plasma, and a broadening of the RHEED pattern is seen (Pattern III). Higher annealing temperatures promote recrystallization, leading to superior material properties, but increase the decomposition and roughening of the grown film. As part of our optimization of this process, we carefully determined our growth and decomposition rates to ensure this annealing step does not entirely decompose the grown thin films. Based on these extensive calibration studies, each growth/annealing cycle results in at least 10 nm of the AlN buffer layer thickness remaining. This is consistent with the observations from the detailed STEM studies of the AlN thin film cross section (shown in Fig. 4.2). When reinitiating the growth following the annealing stage, the RHEED pattern shows inverted V-shaped chevron features consistent with facets having formed at the surface [199], [200]. Stages I (buffer) and II

(annealing) are repeated to further improve the quality of the AlN template. After three such cycles, the thickness of AlN buffer layer is ~30 nm. Studies were also performed with increased number of cycles, which yielded similar results as those with three cycles of growth/annealing. Afterwards, a final buffer (Stage III) is grown in a similar manner as Stage I to help recover and smoothen the faceted surface. Finally, the remainder of the AlN sample (Stage IV) is grown in a more conventional manner [97], [192], [196]: keeping the plasma parameters unchanged, the Al flux is increased to 1.1×10^{-7} Torr to shift the growth into slightly metal-rich conditions. Periodic interruptions of the source-metal fluxes are utilized to help with this process, such that the streaky RHEED pattern (Pattern IV) can be maintained without the buildup of excess metallic Al [98]. Under these conditions, a growth rate of ~180 nm/hour is achieved. Using this growth process, samples with varying AlN thickness, between 0.1 to 1 µm, are achieved by adjusting the duration of this final stage of growth.

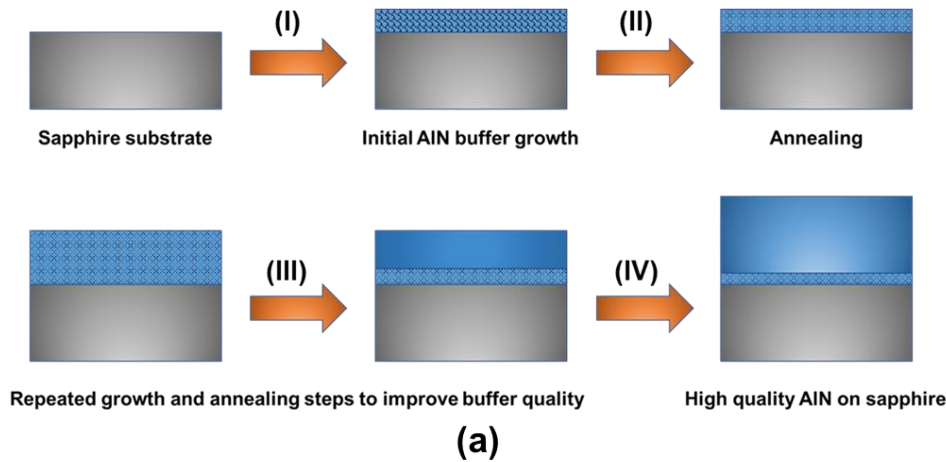

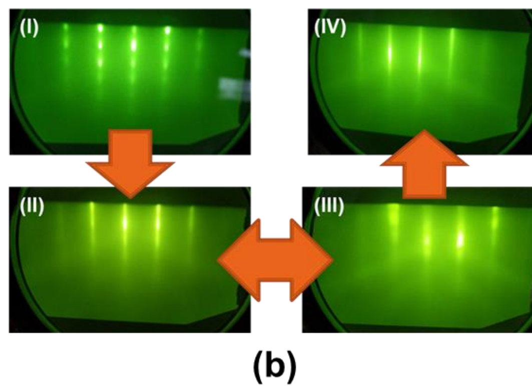

Figure 4.1 – (a) Schematic of the growth sequence of AlN on sapphire substrate: (I) initial AlN buffer growth using a MEE process, (II) high-temperature annealing of the grown ultrathin film, (III) repeated growth and annealing steps to improve the buffer layer quality, and (IV) epitaxy of high-quality AlN epilayers using an interruption-assisted process. (b) Photographs of the RHEED patterns observed during growth: (I) spotty and segmented pattern during the initial stage of growth, (II) streakier pattern during the buffer stages, (III) broadened and brighter pattern during the annealing stages, and (IV) narrow streaky pattern during the epilayer growth stage.

4.4 Structural Characterization of the Ultrathin AlN Films on Sapphire

Of most interest for this study are the thinner samples, since they are the most challenging to obtain in high crystalline quality irrespective of method used. The bulk structural properties of such samples were characterized by electron microscopy and XRD. A thin AlN sample grown directly on sapphire was investigated using a FEI Titan Cubed 80-300 STEM equipped with CEOS

correctors on both the probe and image forming lens systems, operated at an accelerating voltage of 200 kV. Peak pair analysis (PPA) software was used to study the local lattice parameter distribution in the structure [201]. Electron-transparent specimens of AlN/sapphire were prepared for STEM analysis by FIB using a Zeiss NVision 40 dual-beam instrument operating at 30 keV. Figure 4.2(a) shows a STEM image in cross section taken in medium angle conditions to more prominently reveal the defects in the sample [199]. The two layers of the structure have been marked by white arrows. The AlN layer thickness has been measured to be ~100 nm. Threading dislocations (TDs) can be observed crossing the AlN layer. This type of defects frequently appears to release the strain at interfaces with high lattice mismatch as in the case of AlN/sapphire [202], [203]. From this STEM image, it can also be seen that a significant number of the initially formed TDs are then terminated [195], [204] and stop propagating within the first 50 nm of growth, consistent with the initial buffer layers before and after the multiple in situ annealing cycles. In contrast, in previous reports, several hundreds of nm of buffer are required to obtain a desired top layer, and most dislocations generated in these layers propagate all the way to the surface [58], [184], [195], [205], [206]. Another noteworthy finding from these studies is the presence of misorientations in the AlN film that are directly due to steps on the sapphire surface causing a small misalignment (<1 degree). While the exact cause and possible mitigation steps are being investigated, these observations reveal the significant impact of the substrate surface on the epilayers, and that precise control of the initial interface is key to growing high-quality AlN. In this regard, Fig. 4.2(b) shows a high-magnification STEM image of the interface between the AlN layer and the sapphire substrate. The brighter spots seen in the sample are due to contamination/redeposition from the FIB sample preparation process. The interface between both materials is very smooth, but atomic steps can be observed, such as the one marked with a red

arrow. In order to obtain quantitative information about the local atomic displacements in the AlN layer compared to the sapphire substrate (the zone of reference), PPA has been applied to Fig. 4.2(b). Figure 4.2(c) presents the ε_{xx} strain (defined with respect to a reference area) map, in the direction contained in the growth plane, obtained during the analysis. No noticeable strain variations are observed in the sapphire substrate (since it is taken as reference) given that the values are near zero. However, a remarkable variation in lattice parameter can be clearly observed in the AlN layer. When taking the substrate as a reference, the apparent "strain" value, i.e. the difference compared to the reference sapphire, has been measured as 13.1 ± 0.2% based on the plot profile in Fig. 4.2(d) taken along the map. This value agrees with the lattice mismatch expected between AlN and sapphire, 13.3% [207], suggesting that the AlN layer is grown almost fully relaxed, as it is extremely close to maintaining its bulk lattice parameter.

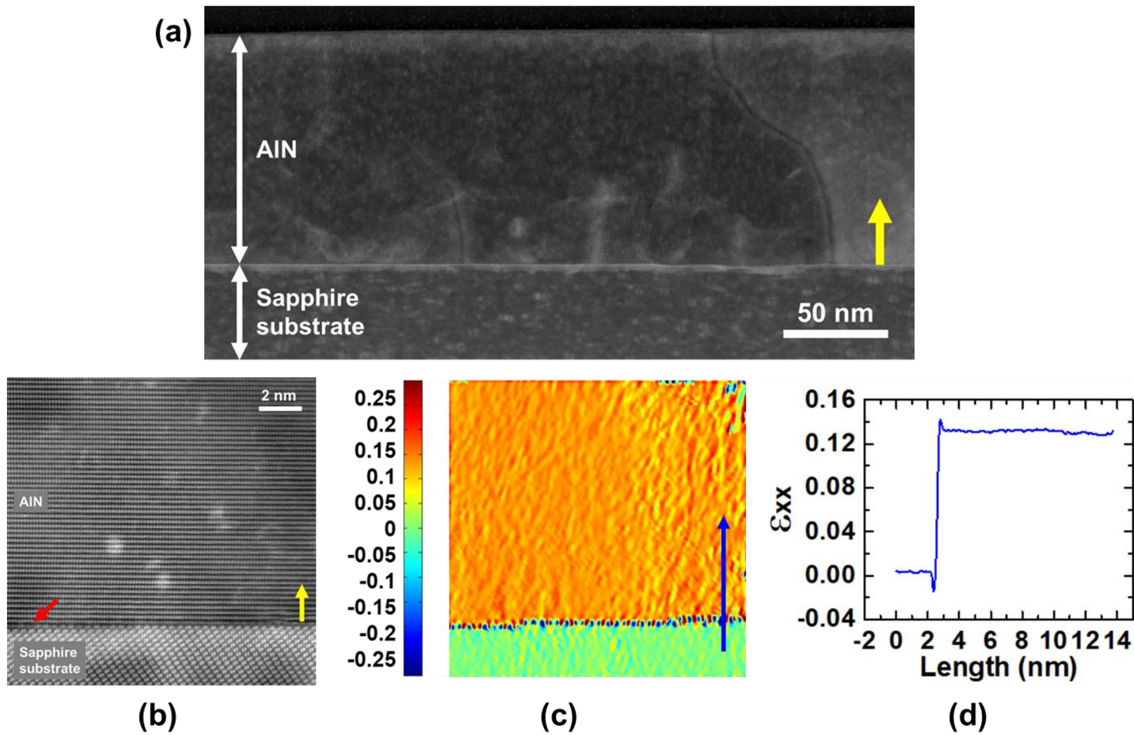

Figure 4.2 – (a) STEM cross-section image of the ~100-nm-thick AlN sample on sapphire substrate. The yellow arrow indicates the growth direction. (b) High-magnification STEM image of the AlN and sapphire interface. The red arrow highlights an atomic step height mismatch at

the interface. (c) ε_{xx} strain map (in the direction contained in the growth plane) obtained during the analysis, with the strain values (taking sapphire as the zero reference) in the included color scale bar. (d) Strain profile taken along the map in (c) denoted by the blue arrow.

XRD was performed using a Rigaku SmartLab X-ray Diffractometer with a Ge(220) 2-bounce monochromator aligned for thin-film rocking curve analysis. For a ~100 nm-thick sample, the measured XRD (002) rocking curve is shown in Fig. 4.3(a). Its peak FWHM is 126 arcsec based on a Lorentz fitting. The (102) FWHM is 1387 arcsec, based on a Lorentz fitting of the curve from Fig. 4.3(b). These are the narrowest linewidths reported for AlN epilayers of comparable thickness grown by any technique [95], [97], [163], [184]–[187], [193], [195], [204], [208]–[223], as highlighted in Fig. 4.3(c). In contrast, for a sample grown with similar thickness but without the use of the multiple cycle in situ annealing steps, the (102) linewidth is over 4000 arcsec. In that regard, we found that higher annealing temperatures help obtain a narrower linewidth, up to a limit above which a worsening of the (002) linewidth is observed and the surface becomes increasingly difficult to recover. These observations are consistent with the fact that the (102) FWHM will become narrower with overall reduced threading dislocation densities [205], [224], especially edge dislocations [225], while the (002) linewidth is sensitive to screw dislocations that will remain regardless of the subsequent epitaxy process [220], [223].

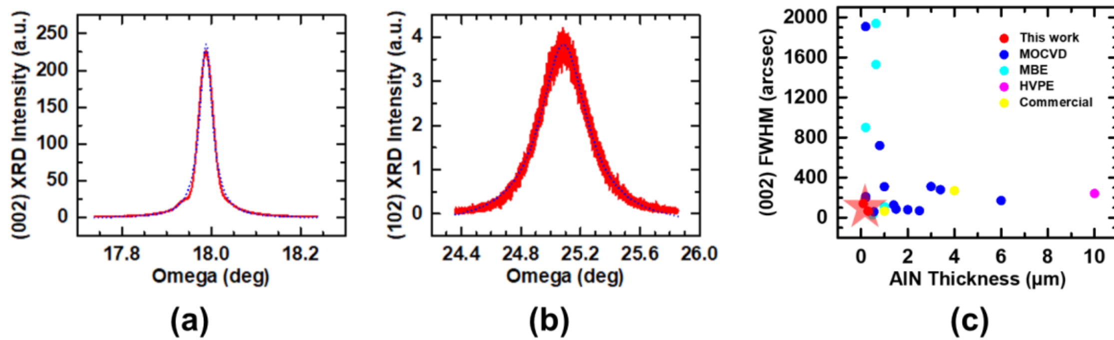

Figure 4.3 – XRD rocking curves (in red) of the (a) symmetrical (002) and (b) asymmetrical (102) reflections of the ~100-nm-thick AlN layer grown on sapphire substrate. The dotted blue

curves are the Lorentz fitting of each curve, used to obtain a FWHM of 126 arcsec and 1387 arcsec for (a) and (b), respectively. (c) Comparison of AlN XRD (002) rocking curve linewidths reported in literature and that of this work (in red).

4.5 Optical Characterization of the Ultrathin AlN Films on Sapphire

Optical properties of the thin (~100 nm) AlN epilayer grown directly on sapphire were characterized using variable excitation power and temperature-dependent PL spectroscopy with a 193 nm ArF excimer laser as the excitation source. The sample emissions were spectrally resolved by a Horiba iHR550 spectrometer and a UV-sensitive Symphony II CCD detector. At cryogenic temperatures, the excitonic emission of AlN at ~205 nm is accompanied by lower-energy shoulder emissions that can be attributed to its longitudinal optical (LO) phonon replica [226], shown in the inset of Fig. 4.4(a). As the temperature is increased, as expected for AlN, the emission intensity is reduced, and the emission peak is redshifted to ~208 nm. Figure 4.4(a) shows the temperature dependence of the integrated PL intensity. As seen in the inset of Fig. 4.4(b), an estimated IQE of ~30% is obtained, by taking the ratio of integrated PL intensities at room and low temperatures, assuming near-unity quantum efficiency at low temperature [178]. The droop is likely due to heating and other non-ideal effects under high laser excitation conditions. For comparison, shown in Fig. 4.4(b), the near-band-edge PL emission of this sample is nearly twice as strong as a commercial AlN epitaxial template (DOWA Electronics Materials Co., Ltd.) that is ~10 times thicker.

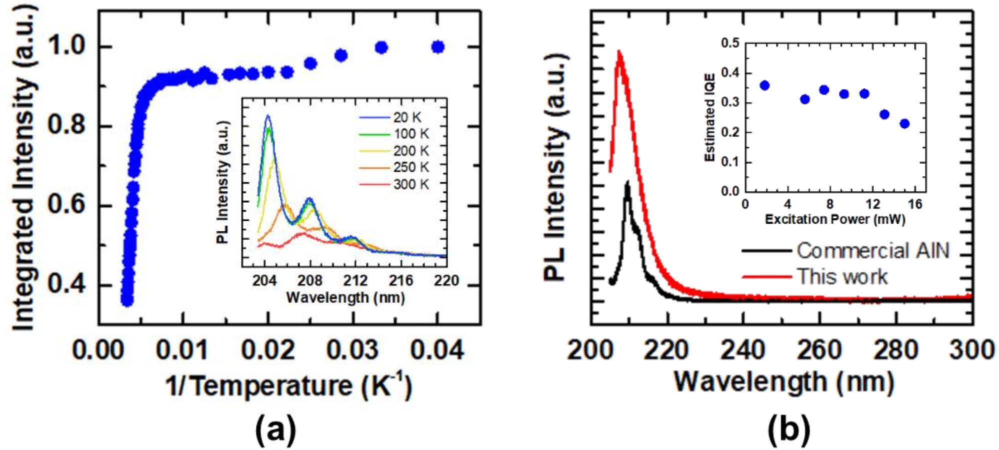

Figure 4.4 – (a) Normalized temperature dependence of the integrated PL intensity of the ~100-nm-thick AlN sample. The inset shows the emission spectra under constant excitation power at various temperatures. (b) Comparison of the PL intensity of the same sample (in red) and a commercial AlN epitaxial template that is ~10 times thicker (in black). The inset shows the estimated IQE of ~30% of the sample from this study.

4.6 Thicker AlN Epilayers on Sapphire

Using the same growth approach as the thin sample, AlN epilayers with various thicknesses can be obtained by simply extending the epilayer growth duration (Stage IV of Fig. 4.1(a)). For such a 1-μm-thick sample, the (002) and (102) X-ray rocking curve peaks have FWHM values ~60 arcsec and 1050 arcsec, respectively. Using a Hitachi SU8000 SEM, an overall uniform and smooth surface can be seen in Fig. 4.5(a) of this sample's surface, with an absence of hillocks or cracks commonly seen after the growth of lattice mismatched layers due to strain [220], [227]. This holds true at the entire wafer scale, as verified by optical microscopy, with an image included as inset. A Bruker Dimension Icon AFM was used in tapping mode in air to obtain the 1×1 μm^2 surface topology (Fig. 4.5(b)). The observed terraces are of atomic steps corresponding to the top epitaxial monolayers that did not fully form at the end of growth [169]. The RMS roughness is ~0.3 nm. The PL spectra at room and cryogenic temperatures are shown in Fig. 4.5(c). The PL

intensity is ~20 times stronger than the commercial AlN epitaxial template with similar 1 μm thickness (Fig. 4.5(d)). Further improvements in material quality are expected with more refined surface treatment methods of the sapphire substrate [227]–[229], and a study of the impact of post-growth annealing of these AlN samples as has been demonstrated in other works [95], [97], [221], [222].

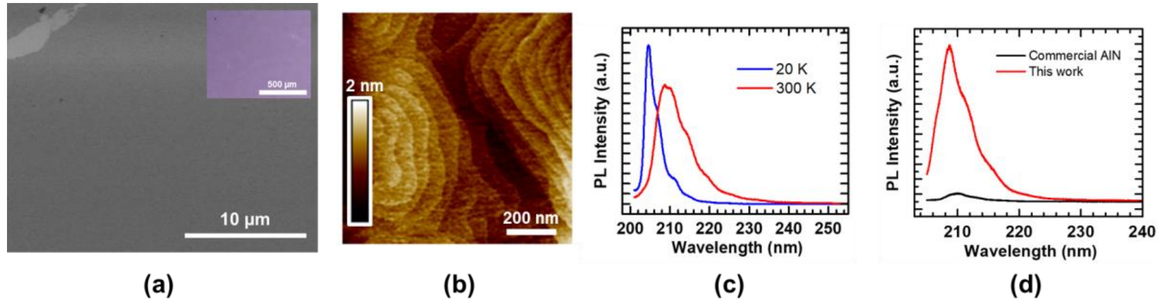

Figure 4.5 – (a) Low-magnification SEM image of the ~1-μm-thick sample surface. The intentional scratch mark on the top left corner was used to properly focus on the sample surface. An optical image is included as the inset. (b) High-magnification AFM image of the sample surface topology. (c) PL spectrum of the sample at room (in red) and cryogenic (in blue) temperatures. (d) Comparison of the PL intensity of the same sample (in red) and the commercial AlN epitaxial template from Fig. 4.4(b) (in black).

4.7 Conclusion

In summary, we have studied the epitaxy and characteristics of AlN epilayers grown directly on sapphire using a high-temperature-assisted MBE process. We demonstrate that strain-free ultrathin AlN epilayers can be obtained directly on sapphire by utilizing in situ high-temperature annealing. We further show that the optical properties are significantly better than commercial AlN templates, which is consistent with the excellent structural properties. Future studies include the development of high quality AlGaN by MBE using a similar approach as in this study, and the demonstration of high efficiency and high power deep-UV light-emitting diodes (LEDs) and laser diodes.

Chapter 5 AlN/h-BN Heterostructures for Mg Dopant-Free Deep Ultraviolet Photonics

5.1 Author Contributions and Copyright Disclaimer

The contents of this chapter were published in ACS Publication's Nano Letters in May 2017 [99], for which I retain the right to include it in this thesis/dissertation, provided it is not published commercially. The co-authors were Zetian Mi from the University of Michigan, Songrui Zhao, Hong Nhung Tran, Huy Binh Le, Thomas Szkopek and Hong Guo with past or current affiliation with McGill University, and Steffi Y. Woo and Gianluigi A. Botton with past or current affiliation with McMaster University. I designed, conducted and authored most of the work. The work was supervised by Z. M., who contributed to the design of the experiments. S. Z. contributed to the growth experiments. H. N. T. and H. B. L. conducted the Hall effect measurements, with supervision and assistance by T. S., who also contributed to the discussions. H. G. provided theoretical insights into the underlying mechanisms of the h-BN material and heterojunction LED operation. S. Y. W. and G. A. B. performed the STEM and related characterization of the samples. This work was supported by NSERC, and US Army Research Office under the grant W911NF-17-1-0109. Part of the work was performed in the Nanotools Microfab facility and Facility for Electron Microscopy Research at McGill University. High-resolution SEM and STEM were performed in the Canadian Centre for Electron Microscopy, a national facility supported by NSERC, the Canada Foundation for Innovation under the MSI program, and McMaster University.

5.2 Background and Motivation

An efficient LED operating in the UV-C band is in demand for a broad range of applications, including analytical chemistry, medicine, water purification, sensing and sterilization [42], [44], [53], [134], and represents the *only* alternative technology to replace conventional mercury lamps and excimer laser sources, which are costly and toxic and suffer from short lifetimes and instability [230]. In the past decades, significant progress has been made in (Al)GaN LEDs and laser diodes operating in the blue and near-UV spectral range [130], [139], [150], [159], [231]–[233]. Mg has been widely used as the p-type dopant in GaN, but poses significant challenges for AlN; the exceptionally large ionization energy (up to 600 meV) leads to extremely poor doping efficiency [44], [69], [94], [234]. Moreover, the presence of free hole concentration in Mg-doped AlGaN is heavily compensated by the formation of extensive native defects and impurity incorporation during the epitaxy of highly lattice mismatched AlGaN epilayers [57]. In an effort to reduce the contact resistance, a common approach is to grow a thin p-(Al)GaN capping layer, which, however, is highly absorptive in the deep-UV spectrum [53]. Other significant challenges for achieving high efficiency UV-C optoelectronic devices include the large spontaneous polarization of AlGaN and enhanced electron overflow for devices operating near 210 nm, due to the lack of carrier confinement.

h-BN, an ideal substrate for two-dimensional materials such as graphene [28]–[30] and one of the building blocks for van der Waals heterostructures [20], [27], has recently demonstrated considerable promise for deep-UV optoelectronics owing to its large bandgap and near-zero polarization field [17], [19], [20], [235], [236]. It has been identified as a structurally compatible material with wurtzite Al(Ga)N to form heterostructures to provide effective carrier confinement [16], [94], [237] (see Section 1 of Appendix F). Unique to h-BN is its unusual propensity for p-

type doping; the p-type resistivity of Mg-doped h-BN is measured to be significantly smaller than that of Mg-doped AlN [238]. Moreover, recent theoretical calculations have shown that the formation of point defects, such as B vacancies, serve as acceptors in h-BN (see Section 2 of Appendix F). For example, the energy level of B vacancies is calculated to be ~150 meV above the valence band edge [25]; the corresponding ionization energy is nearly four times smaller than that for Mg dopant in AlN. Strong p-type conductivity may therefore be achieved for nominally undoped h-BN with the presence of B vacancies [239]–[241].

In this context, we have investigated the epitaxy and performance characteristics of Mg dopant-free AlN/h-BN nanowire LEDs. By exploiting the p-type characteristics from B vacancies in h-BN, we have demonstrated that h-BN can exhibit highly stable, efficient p-type conduction when grown under relatively low substrate temperature (400-800 °C) and under N-rich conditions. At room temperature, the mobility is measured to be ~16 $cm^2/V \cdot s$, which is nearly ten times higher than that of Mg-doped AlN [73]. Moreover, free hole concentration can reach up to ~10^{20} cm^{-3}, which is ten orders of magnitude larger than that previously measured for p-type AlN [42], [234], [242]. The resulting Mg dopant-free AlN/h-BN nanowire LEDs exhibit significantly enhanced optical and electrical performance compared to conventional AlN p-i-n LEDs, including higher output power, reduced efficiency droop, and better electrical efficiency. This work provides an alternative path to address the critical p-type doping challenge of wide bandgap III-nitride semiconductors and offers a viable approach for achieving high efficiency deep-UV optoelectronic devices that were not previously possible.

5.3 Growth of AlN/h-BN Heterojunction Nanowire LEDs

Schematically shown in Fig. 5.1(a), the AlN/h-BN nanowire LED heterostructure consists of 100 nm Si-doped AlN, 50 nm undoped AlN, and up to 10 nm h-BN. The energy band diagram

along the nanowire axial direction, showing that h-BN can provide effective charge carrier confinement in the LED active region and reduce electron overflow, is included in Section 1 of Appendix F. Catalyst-free, self-organized AlN nanowires were grown on Si substrate [44] in the first reaction chamber of two interconnected Veeco GENxplor RF nitrogen plasma-assisted MBE systems. The growth conditions include a substrate temperature of 900 °C, an Al flux measured as a beam equivalent pressure of 2×10^{-8} Torr, a nitrogen flow rate of 1 sccm and RF plasma forward power of 350 W. A Si effusion cell was used for n-type doping the bottom segment of the AlN nanowires. The top portion acting as the active region was kept undoped. To promote the formation of these nanowires, n-GaN nanowires were first grown to serve as a template. Subsequently, the sample was transferred into the second MBE reactor chamber, which is equipped with an in situ e-beam evaporation boron source (99.999% purity). The growth of h-BN was conducted at substrate temperatures varying from 400 °C to 800 °C, by evaporating boron with a relatively low rate (< 0.1 Å/s), measured with an Inficon Guardian EIES controller, a nitrogen flow rate of 1.5 sccm and RF plasma forward power of 350 W, corresponding to nitrogen rich conditions to promote the formation of B vacancies. Samples with h-BN thicknesses ranging from 1.5 nm to 10 nm were grown. Shown in Fig. 5.1(b) is the SEM image of AlN/h-BN nanowire arrays, taken using a FEI F50 system. The sample was loaded with a 45° angle and an acceleration voltage of 5 kV was used. The nanowires are vertically aligned on the Si substrate and exhibit a relatively uniform height distribution, with a length and diameter of ~200 nm and 50 nm, respectively. For comparison, conventional AlN p-i-n and i-n heterostructures without BN incorporation were also grown under identical conditions.

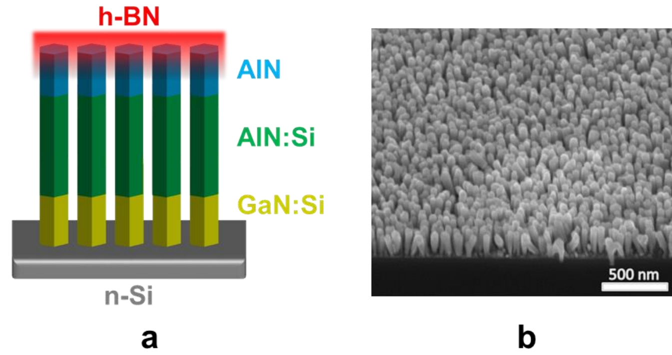

Figure 5.1 – MBE growth of the AlN/h-BN nanowire array. (a) Schematic of the AlN nanowires (n-doped in green, undoped in blue) grown on a GaN nanowire template (in yellow) on a Si substrate (in gray), with a thin layer of h-BN on top (in red). (b) SEM image of such an as-grown nanowire array.

5.4 Characterization of the AlN/h-BN Nanowires

The AlN/h-BN nanowire structure was further investigated using aberration-corrected FEI Titan Cubed 80-300 STEM operated at 200 kV. The nanowire samples were mechanically removed from the Si substrate, deposited after dispersing in anhydrous ethanol or prepared by dry-pressing directly onto carbon-coated TEM support grids for observation. The STEM BF image of a single nanowire, including the GaN template, is shown in Fig. 5.2(a) viewed along the *a*-plane orientation. The GaN (dark gray), AlN (gray) and h-BN (light gray) segments along the growth direction can be observed. The HAADF image of the same nanowire is shown in Fig. 5.2(b), with a detailed view of the nanowire top AlN/h-BN region in Fig. 5.2(c). The h-BN thickness is determined to be ~5 nm. Fig. 5.2(d) shows a high magnification HAADF image of the AlN (bright contrast) and h-BN (dark contrast) interface, which confirms that the AlN segment is free of extended defects. By comparison, the h-BN segment appears mostly dendritic, with the presence of nm-sized regions of crystalline lattice planes visible interlaced throughout. The measured interlayer spacing is 3.3 – 3.4 Å, and corresponds well to the h-BN (0002) interplanar spacing. The

pseudo-color composite elemental map from EELS spectrum imaging in Fig. 5.2(e) illustrates the distribution of group-III elements in the top AlN/h-BN region. Weighted-principal components analysis was applied for noise reduction of the EELS spectrum images using the MSA plugin implemented within DigitalMicrograph by HREM Research Inc. The Al-map extracted from the Al $L_{2,3}$-edge shows defined boundaries to the semi-polar top facets of the AlN segment. More notable is the B-map, showing the continuous coverage of h-BN along both the top and sidewall surfaces of the AlN nanowire, which leads to the formation of an AlN/h-BN core-shell nanowire heterostructure.

To identify the crystalline phase of the boron nitride, additional spectroscopic analysis was conducted by STEM-EELS to investigate the nature of the bonding. The B K-edge spectrum in Fig. 5.2(f) exhibits the π* peak at 191 eV characteristic of sp^2-hybridization in hexagonal BN, while the other peaks (σ* fine structures) also match the ones previously reported for h-BN [243], [244]. Similar correspondence is observed between the N K-edge because of the strong covalent bonding, including the π* peak and the subsequent σ* fine structures on the N K-edge [244]. The low-loss EELS spectrum from the h-BN layer (see Section 3 of Appendix F) shows a dominant bulk plasmon (σ + π type) peak at ~25 eV, and a secondary peak at ~8 eV corresponding to the π*-plasmon that is also characteristic of sp^2-hybridization in h-BN. The bulk plasmon peak energy provides further evidence that the crystalline form of the boron nitride film is hexagonal [245].

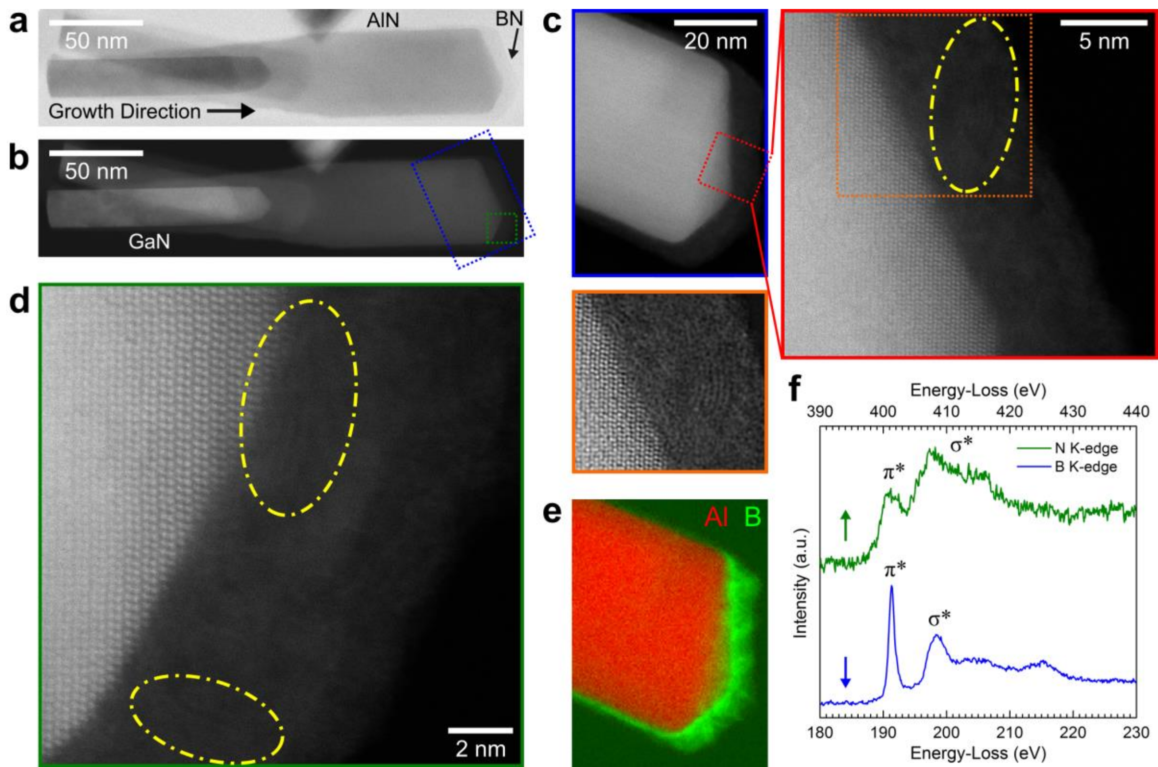

Figure 5.2 – Structural characterization of a single nanowire. (a) STEM-BF and (b) HAADF images of an AlN/h-BN nanowire, highlighting the GaN template, AlN, and h-BN segments. (c) High-magnification HAADF image of the AlN/h-BN region, and inset (boxed in red) detailed views of the crystalline lattice within the h-BN layer (circled in yellow). Additional inset shows a bandpass filtered image of the region boxed in orange to emphasize contrast in the crystalline layers. (d) Detailed view of the h-BN layer from another area (boxed in green in b) in the same nanowire. (e) STEM-EELS elemental map of the region in c, extracted from the Al $L_{2,3}$ and B K-edges, showing conformal h-BN coverage on the top and sidewall facets of the AlN segment. (f) Core-loss EELS spectra of the N K, and B K-shell ionizations from the h-BN layer showing both π^* and σ^* components labeled that correspond to sp^2 hybridization in hexagonal BN.

The optical properties in the deep-UV range of the AlN/h-BN nanowire heterostructures obtained from power-dependent PL measurements are shown in Fig. 5.3(a). PL measurements were performed using a 193 nm ArF excimer laser as the excitation source. The emitted light from the samples were spectrally resolved by a high-resolution, UV-sensitive Horiba iHR550 spectrometer and detected using a low-noise Symphony II CCD detector. The inset of Fig. 5.3(b) compares the PL spectrum measured at 210 nm at cryogenic (20 K) and room temperatures (300

K), using a helium cold finger cryostat, which agrees well with that measured from nearly defect-free AlN nanowires [44]. The IQE is estimated by taking the ratio of the integrated PL intensity measured at 300 K over that at 20 K [178], assuming a near-unity efficiency at 20 K. Shown in Fig. 5.3(b), the IQE is derived to be ~80% over a broad range of excitation conditions, which is significantly higher than that of AlN epilayers [246]. PL emission characteristics of the h-BN segment as well as h-BN thin films grown under similar conditions are also characterized, dominated by emission from B vacancy-related defects (see Section 4 of Appendix F).

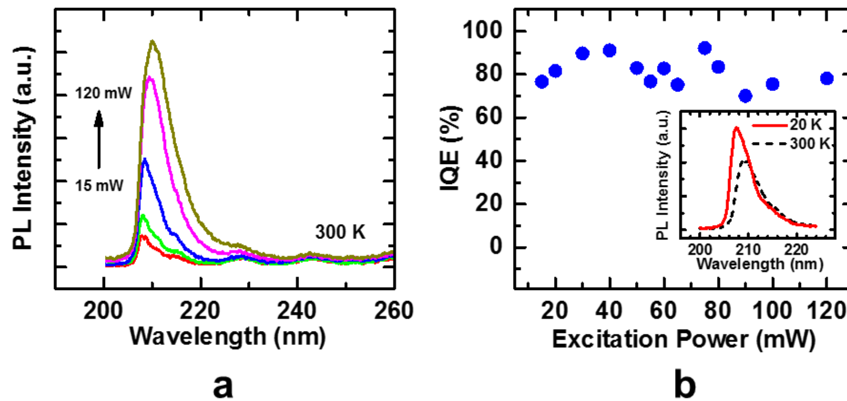

Figure 5.3 – PL and optical properties of the nanowires. (a) Room-temperature PL spectrum of the AlN/h-BN nanowire sample at various excitation powers. (b) Estimated IQE at these excitation powers. Inset shows the PL spectrum centered at 210 nm at 20 K (in solid red) and 300 K (in dashed black).

5.5 Mg Dopant-Free AlN/h-BN Nanowire Light-Emitting Diodes

Large-area, Mg dopant-free AlN/h-BN nanowire LED devices, as schematized in Fig. 5.4(a), were subsequently fabricated and characterized. Devices were fabricated by depositing topside p-metal contacts (15 nm Ni / 10 nm Au) with the nanowire samples loaded at a tilted angle of 30°. These metal layers were deposited without the addition of a filling material to prevent the absorption of deep-UV photons by taking advantage of the high density of the nanowires and the

shadowing effect obtained by tilting these samples during the metal evaporation process. 10 nm Ti / 30 nm Au deposited on the backside of the heavily n-doped Si substrate act as a suitable n-metal ohmic contact. Devices with sizes ranging from 0.1 mm^2 to 1 mm^2 were defined by standard photolithography techniques. Fig. 5.4(b) shows the *I-V* characteristics of a 0.3 mm × 0.3 mm device, measured with a probe station and a Keithley 2400 source meter, with its photograph included in the inset. The same *I-V* plot in semi-log scale is included in Section 5 of Appendix F. The device exhibits excellent *I-V* characteristics, with negligible leakage current under reverse bias. The device turn-on voltage is ~5.5 V, which is only limited by the bandgap energy of AlN and h-BN. For comparison, previously reported planar *c*-plane AlN p-i-n LEDs exhibit turn-on voltages in the range of 20-30 V, due to the poor p-type conduction of AlN [42]. In this study, a forward bias voltage of 7.8 V is measured for a current density of 20 A/cm^2, which corresponds to an electrical efficiency of 80%. We have also studied the *I-V* characteristics of identical nanowire devices except with the omission of h-BN, which did not show any current rectification behavior. This finding demonstrates, for the first time, that h-BN, through intentional B vacancy formation, can serve as a highly conducting p-contact layer for Al(Ga)N deep-UV optoelectronic devices. To further validate that h-BN can exhibit strong p-type conduction, we conducted detailed Hall effect measurements of a uniform h-BN film grown on an SiO_x/Si substrate grown under similar growth conditions as that used for the nanowire LED. The Hall effect measurement was performed at various temperatures to measure the free hole concentration and mobility of a 10-nm thick, uniform h-BN thin film with a standard lock-in measurement technique and a resistive magnet with field up to 3000 Gauss. The film was grown on an SiO_x/Si(001) substrate, where the thickness of the thermal oxide was 200 nm, and was patterned into an area of 200 × 200 μm^2, with electrodes being deposited in a standard van der Pauw geometry. The metal contacts consisted of Ni/Au/Ni/Au

(10/10/20/40 nm), deposited by e-beam evaporation and subsequently annealed at 500 °C in N_2 ambient for 2 minutes. The sample was mounted in a nitrogen cryostat for variable temperature Hall measurements. The measured temperature dependent Hall mobility and bulk carrier density are shown in Fig. 5.4(c). The hole mobility and concentration follow that of conventional semiconductors, i.e., the Hall mobility decreases while the free hole concentration increases with increasing temperature. The hole mobility is 16 $cm^2/V \cdot s$ and the hole concentration is as high as 10^{20} cm^{-3}, with a corresponding resistivity of 5 mΩ·cm, over ten orders of magnitude greater than that previously measured for Mg-doped AlN [42], [234], [242]. The specific contact resistivity was measured to be below 1×10^{-2} $\Omega \cdot cm^2$. Such unusually strong p-type conduction is directly related to the formation of acceptor-like point defects in h-BN. The use of a relatively low growth temperature and N-rich conditions promote the formation of B vacancies. Recent theoretical studies have revealed that the energy levels of B vacancies are positioned at ~0.15 eV above the valence band edge [25], which can be readily ionized to provide free holes in h-BN. Detailed correlation between calculated defect energy levels and the optical spectra of h-BN are described in Sections 2 and 4 of Appendix F. Moreover, compared to the conventional p-GaN contact layer, h-BN is transparent in the deep-UV spectral range (see Section 6 of Appendix F).

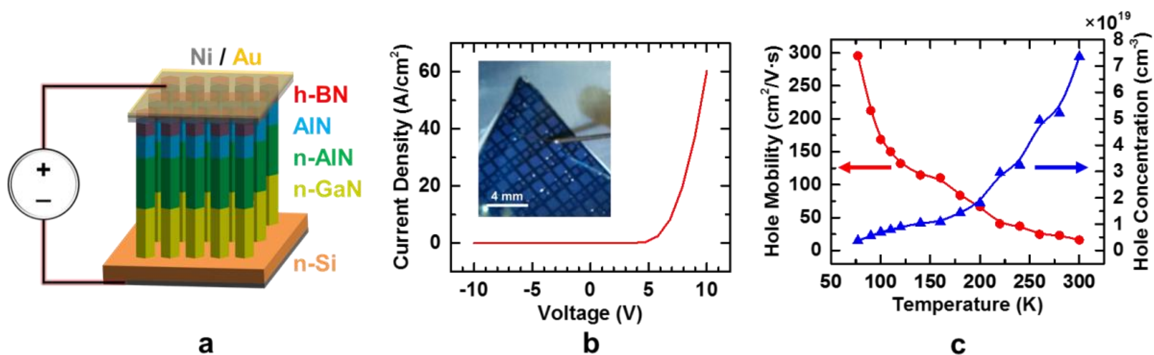

Figure 5.4 – Electrically injected AlN/h-BN nanowire LEDs. (a) Schematic of the fabricated LED structure, which includes thin Ni/Au p-metal contacts and the heavily n-doped Si substrate as the n-contact. (b) I-V curve of a 300 μm × 300 μm LED device at room temperature, with a

photograph of said device as the inset, which is characteristic of a diode rectification behavior. (c) Variation of Hole mobility and concentration of an equivalent h-BN layer grown on a SiO_x/Si substrate as a function of temperature.

Presented in Fig. 5.5(a) are the EL emission spectra of an AlN/h-BN nanowire LED measured at room temperature, with the emitted light being collected by a UV-sensitive optical fiber coupled to the same spectrometer used for the PL studies. The device exhibits emission at ~210 nm, which corresponds to the excitonic emission of AlN. The lower energy shoulder emission can be attributed to the LO phonon replica of the exciton emission in AlN [226]. The small red shift of the peak wavelength with increasing current is due to the Joule heating effect. No other defect-related emission is measured in the deep-UV spectral range. This device is the first demonstration of EL from any h-BN/Al(Ga)N heterostructure [16], [94]. Shown in Fig. 5.5(b), the output power increases near-linearly with increasing injection current. The output power is estimated to be 50 nW at 60 A/cm^2, by measuring the intensity of a commercial UV LED (Marktech Optoelectronics MTE280F13-UV) with a known power output to establish a calibration between the optical power and measured CCD counts. This output power is more than one order of magnitude greater than that measured from an equivalent AlN nanowire p-i-n LED device without the use of a h-BN contact layer. Since AlN nanowire segments in both samples are grown under identical conditions, the significantly enhanced output power of the AlN/h-BN LED is directly related to the enhanced hole transport and injection, and eliminated light absorption by the top p-Al(Ga)N segment. The use of h-BN p-contact layer provides not only more efficient hole transport and injection, but also effective charge carrier confinement in the active region, which can lead to significantly reduced electron overflow. The relative EQE, defined as the ratio of output power and current density, is plotted in Fig. 5.5(c) for various injection currents. The EQE first increases with increasing injection current, then saturates and decreases at high injection currents.

This behavior is characteristic of the efficiency droop in LEDs, due to factors such as electron overflow and other carrier loss mechanisms [65], [66], including in AlN-based devices [72].

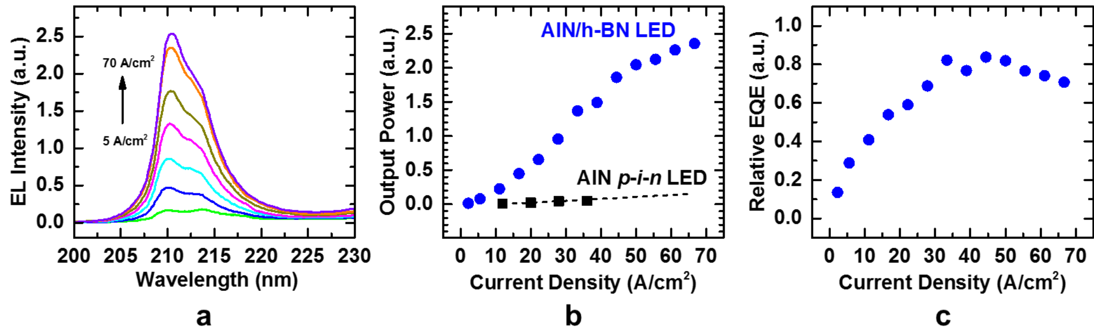

Figure 5.5 – EL properties of the AlN/h-BN nanowire LED. (a) EL spectrum of this LED device at ~210 nm for various injection currents, measured at room temperature. (b) Light output as a function of injection current, showing a near-linear increase and saturation at higher current densities. The black squares show the same measurement results for an equivalent AlN p-i-n homojunction LED. The black dashed line is a linear extrapolation of the output power at higher current densities. (c) Relative EQE as a function of the injection current density for this LED device, showing an increase up to a maximum efficiency, followed by a droop at higher injection currents.

We have monitored the device performance, including *I-V* and light emission characteristics, over a six-month period, which has remained virtually unchanged, confirming the stability of hole conduction of h-BN.

5.6 Conclusion

The highly efficient, stable p-type conduction of h-BN, together with its large bandgap and unique band alignment with Al(Ga)N, can therefore effectively address the present challenges of UV-C optoelectronics. With controlled p-type characteristics, h-BN is also positioned to significantly advance the efficiency of III-Nitride LEDs and lasers operating in the UV-B, UV-A, blue, and blue-green wavelength ranges by replacing the highly resistive Mg-doped Al(Ga)N layers. Moreover, the highly conductive and transparent h-BN nanowire and film structures opens

up exciting opportunities to replace indium tin oxide (ITO), which is one of the most widely used transparent conductive electrodes, but is limited by the high cost and shortage of indium [247], and inadequate transmittance for wavelengths below 400 nm [248]–[250]. For high-performance applications, deep-UV transparent sapphire substrates can be utilized. Future work also includes the development of Al(Ga)N/h-BN quantum-confined nanostructures and planar heterostructures to control the polarization of deep-UV light emission and to achieve wavelength tunable high efficiency LEDs and lasers operating in the UV-C band.

Chapter 6 Effect of Growth Temperature on the Structural and Optical Properties of Few-Layer Hexagonal Boron Nitride by Molecular Beam Epitaxy

6.1 Author Contributions and Copyright Disclaimer

The contents of this chapter were published in OSA Publishing's Optics Express in August 2018 [100], for which I retain the right to include it in this thesis/dissertation, provided it is not published commercially. The co-authors were Kelsey Mengle, Yongjie Wang, Emmanouil Kioupakis and Zetian Mi with past or current affiliation with the University of Michigan, and Songrui Zhao from McGill University. I designed, conducted and authored most of the work. The work was supervised by Z. M., who contributed to the design of the experiments. S. Z. contributed to the growth experiments. Y. W. contributed to some of the sample characterization. K. M. and E. K. conducted the theoretical calculations and contributed in correlating these results to the experimental ones. This work was supported by the National Science Foundation under grant DMR-1807984; Natural Sciences and Engineering Research Council of Canada (NSERC) award PGSD3-502905-2017; US Army Research Office under grant W911NF-16-1-0582; National Science Foundation Graduate Research Fellowship Program (NSF GRFP) through grant DGE 1256260. This research used resources of the National Energy Research Scientific Computing (NERSC) Center, a DOE Office of Science User Facility supported under Contract No. DE-AC02-05CH11231.

6.2 Introduction

BN, in particular its hexagonal polymorph (h-BN), has shown in recent years tremendous promise when used alongside other 2D materials such as graphene, and as a wide-bandgap semiconductor for deep UV optoelectronics and quantum photonics. Given its crystalline structure, h-BN can be the perfect 2D insulator with an atomically smooth surface [251]. This property makes it suitable for van der Waals epitaxy [20], [27] and as a substrate for the growth of other 2D materials such as graphene [30]. In addition, h-BN as a wide-bandgap semiconductor has many promising applications in deep-UV photonics. Owing to its large bandgap energy, comparable to or higher than Al(Ga)N, h-BN can be used to form heterostructures to address some of the critical challenges of Al(Ga)N-based systems, allowing for better device performance and efficiency [16], [17]. To date, however, many fundamental material properties of h-BN remain unknown. For example, its bandgap energy remains under debate, with reports spanning from 5.9 to 6.5 eV. There is also strong controversy as to whether h-BN has a direct or indirect bandgap [14], [19]–[22]. To better understand and further analyze these unique properties, it becomes critical to develop controllable means to epitaxially grow h-BN of high crystalline quality.

Many previous studies of this material use thin films obtained by mechanical or chemical exfoliation of h-BN flakes [251], but more scalable growth of h-BN by MOCVD [252]–[254] and MBE [30], [255], [256] are essentially required for practical device application. To date, however, the epitaxy of h-BN and a detailed understanding of its fundamental properties are still in their infancy. Recent findings include the importance of the nitrogen atom supply (NH_3 flow rate) for MOCVD-grown h-BN in eliminating nitrogen vacancies, resulting in epilayers with pure free exciton emission [26]. It is also believed that high MBE growth temperatures favor the formation of crystalline h-BN [257], [258]. A variety of substrates have been considered, including sapphire

[259], [260], pyrolytic graphite [257], and metals such as Cu [261], [262], Pt [263], and Co [30]. In particular, Ni(111) is an attractive substrate [254], [255], [258], [264], [265], due to a small lattice mismatch (~0.5%) with h-BN [266] and strong interaction in the chemical bonding [267].

In this work, we have investigated, both theoretically and experimentally, the properties of few-layer h-BN grown by plasma-assisted MBE, using a relatively low growth rate (<0.1 Å/s), and nitrogen-rich condition on Ni(111) substrate. It is observed that the material quality depends critically on the growth temperature. When grown at temperatures <1000 °C, the h-BN film is polycrystalline and defect-related PL emission dominates. Epitaxial domains of exceptional crystalline quality are obtained at elevated substrate temperatures of ~1300 °C, which was validated by micro-Raman analysis and strong near-band-edge emission (~220 nm). At room temperature, the luminescence intensity of few-layer h-BN is nearly 100 times higher than that of high quality, 4-μm thick, commercially grown direct-bandgap AlN. Theoretically, we have studied the vibrational, electronic, and optical properties of h-BN using atomistic calculations based on density functional and many-body perturbation theory, which agree well with the experimental results [268]. Our studies suggest that, although h-BN has an indirect bandgap, it can luminesce as efficiently as a direct-bandgap material, demonstrating the extraordinary potential of epitaxial h-BN for deep UV optoelectronics and quantum photonics.

6.3 Growth and Characterization of Few-Layer h-BN

Few-layer h-BN samples were grown on bulk crystalline Ni(111) substrate using a Veeco GENxplor RF nitrogen plasma-assisted MBE system equipped with an e-beam evaporation source for elemental boron (99.999% purity). The boron evaporation rate was monitored with an Inficon Guardian EIES controller. Growths with nitrogen flow rates from 0.3 to 3 sccm were attempted, in all cases at a constant RF plasma forward power of 350 W. Substrate temperatures from 500 up

to 1300 °C were used in these studies. Prior to initiating the growth, the 1 cm × 1 cm Ni(111) substrates were outgassed, and subsequently heated to 900 °C for 30 min to thermally desorb the surface native oxide [255]. Growth was monitored in situ by RHEED. Both in situ and ex situ characterization of a series of samples showed that, under the presented growth conditions, the growth temperature has the most significant impact on the structural and optical quality of h-BN by MBE [269].

Figure 6.1 shows a 45° tilted-angle SEM image of h-BN samples. In the case of Sample A grown at 500 °C (see Figs. 6.1(a) and 6.1(d)), the RHEED pattern initially showing the streaks from the bulk Ni(111) substrate [255] transitioned to a series of uniform ring diffraction patterns indicative of polycrystalline growth [270], with the formation of nanoscale grains and dendritic micro-surface. Increasing the growth temperature to 900 °C causes a spotty RHEED pattern indicative of a rough surface morphology (not shown) [160], and the samples examined post-growth exhibited poor optical and structural characteristics. Similar behavior is observed until the substrate temperature is increased to 1200 °C, such as is the case of Sample B (see Figs. 6.1(b) and 6.1(e)), where a streaky RHEED pattern was sustained for the duration of the h-BN growth, suggesting two-dimensional epitaxial growth [160]. As can be seen from SEM, the grown material is not uniformly covering the substrate surface. There are rather signs of interconnected or overlapping triangular or star-shaped nucleation centers [262], [271], [272]. It was noticed during the ramp-down process at the end of growth that the RHEED pattern gets broadened. It is however clear at higher-magnification SEM that the h-BN domains are themselves smooth and conformal to the underlying substrate. Sample C (see Figs. 6.1(c) and 6.1(f)) was grown at 1300 °C and showed a narrowing of the streaky RHEED pattern observed from Sample B, which is a sign of improved crystalline quality. SEM at low magnification shows the formation of more uniformly

spread and less clustered triangular domains promoted by the higher growth temperature enhancing boron adatom migration and diffusion along the surface [258], [265]. While an exact thickness of the h-BN domains cannot be measured given their overlaps and clustering, and the irregularities of the substrate surface, the lower and upper boundaries can be estimated to be from several monolayers up to a few nm.

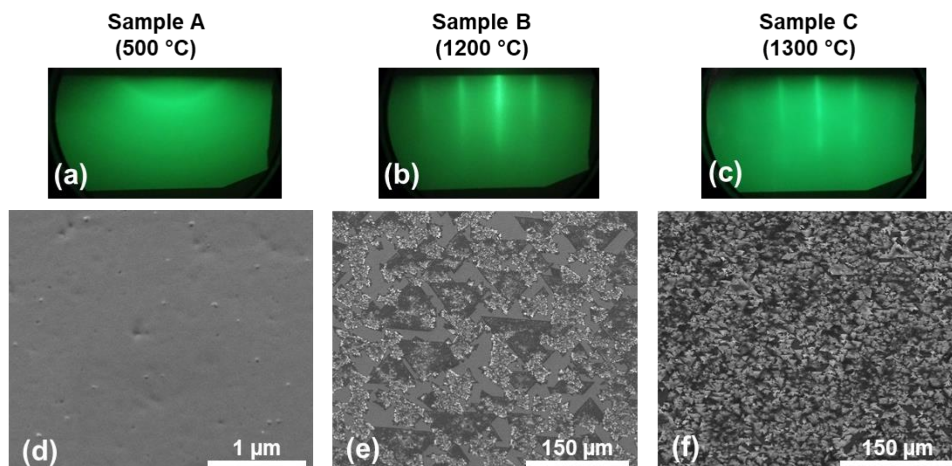

Figure 6.1 – (a)-(c) Snapshots of RHEED patterns during the growth of h-BN at 500 °C (Sample A), 1200 °C (Sample B) and 1300 °C (Sample C), respectively. The RHEED pattern transitions from polycrystalline rings to continuous streaks with samples growing at higher temperature. (d)-(f) SEM images of the same three sample surfaces.

A composition analysis of Sample C was conducted by XPS using a Thermo Scientific K-Alpha system with 100 µm scan size; binding energies were calibrated from the reference C 1s peak (285 eV) [256]. Figures 6.2(a) and 6.2(b) were obtained from the high-resolution scans of B 1s and N 1s. Both spectra show a single peak at a binding energy of 191 eV and 398 eV, respectively, corresponding to the B-N bond; and the π-plasmon peak in the B 1s spectrum at ~200 eV is a signature of h-BN [273]. The XPS elemental analysis using the Thermo Scientific Avantage Data System suggests the formation of pure h-BN on the Ni(111) substrate with nearly 1:1 chemical stoichiometry. It is worth noting that the extremely low oxygen content of this sample

(<2%), given the strong tendency for nickel to oxidize, would indicate the h-BN layers have completely covered the substrate surface [261], [274].

The structural quality of these samples was further characterized by micro-Raman spectroscopy. The measurements were performed using a Renishaw InVia system with a 100× objective and a 488 nm excitation laser. Shown in Fig. 6.2(c), Sample A, the polycrystalline boron nitride thin film grown at 500 °C, exhibits a peak position at ~1365 cm^{-1}, which is consistent with the hexagonal polymorph of this material [275]–[277]. Due to the imperfect material quality, this peak is relatively broad and weak; and a secondary peak at ~1600 cm^{-1} is also present, and is attributed to the theoretically calculated LO phonon mode at 1627 cm^{-1} becoming Raman-active by symmetry breaking, e.g., by disorder or on a surface (inset of Fig. 6.2(c)) [278]. Serrano et al. reported a similar experimental (theoretical) value of 1609.9 cm^{-1} (1610.7 cm^{-1}) [279]. The Raman spectrum of the bare Ni substrate was also measured as a baseline reference. Sample C grown at 1300 °C shows a drastically narrower and stronger Raman peak at 1360 cm^{-1} (shown in Fig. 6.2(d)), corresponding to the in-plane vibrational mode between boron and nitrogen. The FWHM of this Raman peak is 13 cm^{-1}, which is one of the narrowest reported for epitaxially grown h-BN [93], [271], [276], [280]. Our density functional perturbation theory (DFPT) calculations predict a frequency for this phonon mode with symmetry E_{2g} at 1394 cm^{-1}, agreeing within 3% to the experimentally measured value (inset of Figs. 6.2(c) and 6.2(d)). There is also the emergence of a secondary weak peak at ~800 cm^{-1}. Our DFPT studies suggest the presence of two phonon modes at 747 cm^{-1} (IR-active; A_{2u} symmetry) and 818 cm^{-1} (IR- and Raman-forbidden; B_{1g}) (inset of Fig. 6.2(d)). Serrano et al. also reported a phonon mode with A_{2u} symmetry at 747 cm^{-1} (theory) and 783.2 cm^{-1} (experiment) and another with B_{1g} symmetry at 809.8 cm^{-1} (theory) [279]. With symmetry breaking at the surface of the sample, one of these modes could become Raman-active.

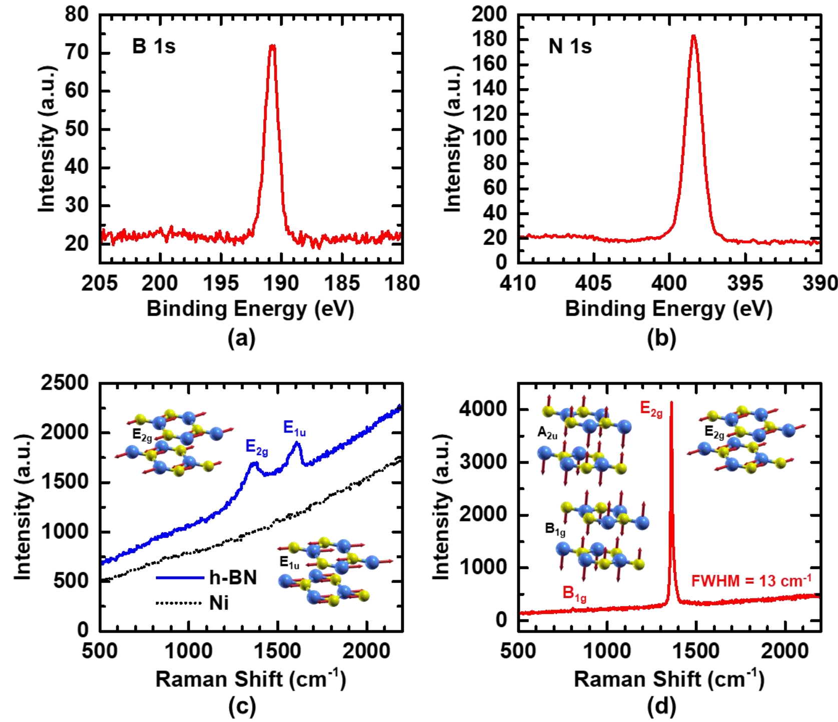

Figure 6.2 – XPS high-resolution spectrum of B 1s (a) and N 1s (b) for the h-BN Sample C. Micro-Raman spectrum of: (c) Sample A (in solid blue) as compared to the bare Ni substrate (in dotted black). The h-BN sample shows peaks at ~1365 and 1600 cm^{-1}, corresponding to theoretical frequencies of 1394 (Raman-active; E_{2g}) and 1627 cm^{-1} (IR-active LO mode; E_{1u}); (d) Sample C, showing a strong and narrow Raman peak at 1360 cm^{-1} (FWHM of 13 cm^{-1}). A secondary weak peak at 800 cm^{-1} is also present. Symmetry-breaking at the surface could turn the theoretically calculated mode at 747 (IR-active; A_{2u}) or 818 cm^{-1} (IR- and Raman-forbidden; B_{1g}) into a Raman-active mode.

6.4 Optical Properties of Few-Layer h-BN Grown by MBE

Optical properties of these samples were characterized using temperature and power variable PL spectroscopy with a 193 nm ArF excimer laser as the excitation source. The emitted photons from the samples were spectrally resolved by a Horiba iHR550 spectrometer and detected using a low-noise Symphony II CCD detector. Shown in Fig. 6.3 are the room-temperature PL spectra of h-BN Samples A, B and C, grown at 500 °C, 1200 °C and 1300 °C, respectively. Sample A shows broad PL peaks centered at ~260 and 300 nm, which are attributed to defect-level

transitions in h-BN, such as boron vacancies, as identified in previous studies [99]. Significantly reduced defect-related emission was measured for the sample grown at 1200 °C (Sample B), with a dominant emission peak at ~220 nm. For the sample grown at 1300 °C (Sample C), the PL intensity of this short-wavelength emission is increased considerably, with the presence of negligible defect-related emission. It is worth noting that these samples were grown using similar growth rates and durations, but that under such conditions, other samples with a reduced growth duration exhibited the same PL spectra but with slightly lower intensities, which can simply be due to less h-BN domains per unit area taking part in luminescence. The PL spectrum of Sample C measured at 20 K is further shown in the inset of Fig. 6.3, which exhibits distinct emission peaks at ~219, 223, and 226 nm. These emission peaks can be ascribed to free and bound exciton related emission and have been previously observed in h-BN epilayers [19], [21], [22]. On the other hand, recent studies suggested that h-BN had an indirect energy bandgap and these emission peaks could be attributed to phonon-assisted processes [20], [281].

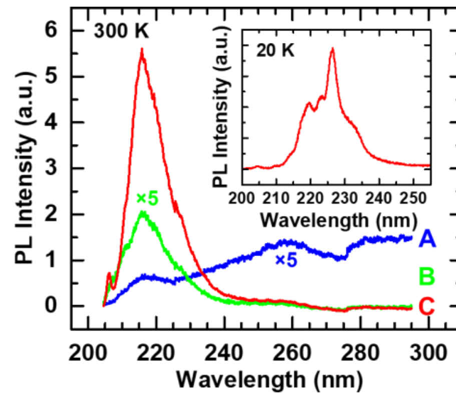

Figure 6.3 – Room-temperature PL spectra of three h-BN Samples A (in blue), B (in green) and C (in red). As growth temperature is increased, the short-wavelength emission is enhanced, and the longer-wavelength defect emissions are suppressed. The inset shows the PL spectrum measured at cryogenic temperature of Sample C.

6.5 Theory and Discussion

To elucidate the underlying mechanism for the luminescence emission of h-BN, we have calculated the phonon frequencies and displacements using DFPT [282] as implemented in Quantum Espresso [283]. We have also determined the band structure with the GW method and the binding energy of the lowest-energy direct exciton via the Bethe-Salpeter equation (BSE) as implemented in the BerkeleyGW code [284]. We identified the locations of the band extrema and their corresponding optical matrix elements using the maximally localized Wannier function method [285] and the wannier90 code [286]. Our atomistic calculations reveal that even though h-BN has an indirect bandgap, it luminesces like a direct-gap material because the corresponding phonon-assisted optical matrix element is strong. Figure 6.4 illustrates a schematic band structure of h-BN. The indirect bandgap of 6.20 eV occurs between the valence-band maximum (VBM) at (0.390, 0.310, 0.990) and the conduction-band minimum (CBM) at the (0.485, 0.035, 0.010) points of the Brillouin zone (in crystal coordinates). The minimum direct gap of 6.69 eV occurs at (0.670, 0.670, 0.480). We attribute the difference between the bandgap and the measured luminescence at lower photon energy to strongly bound excitons. We find the lowest-energy direct exciton binding energy to be 0.83 eV as calculated with the BSE method using a Brillouin-zone sampling grid of 24×24×12. This value is consistent with previous studies [21], [22]. Additionally, optical transitions in indirect-gap materials can be assisted by phonons, which enable energy and momentum conservation. The phonon-assisted matrix element S is given by Equation 6.1.

$$S^2 = \frac{{p_{VBM}}^2 g^2}{(\Delta E + h\omega_{phonon})^2} \qquad \textit{(Equation 6.1)}$$

where p_{VBM}=0.61 (in atomic units) is the velocity matrix element for intraband optical transitions between the valence and conduction band at the VBM location (the corresponding CBM matrix element is approximately zero), g=320 meV is the electron-phonon coupling matrix element in the

conduction band (determined with the Fröhlich model) [50], $\hbar\omega_{phonon}$=0.2 eV is the frequency of the LO phonons, and ΔE=0.6 eV in the energy denominator is the difference between the conduction-band energies at the VBM and the CBM locations [287]. Here we assumed that electrons couple most strongly to the polar optical LO phonons, which is typical of polar semiconductors. The indirect matrix element is then S^2=0.06 (in atomic units), *which is 600 times larger than the corresponding matrix element in silicon* [288]. h-BN can thus luminesce as efficiently as a direct-gap material, even though its band structure has an indirect gap.

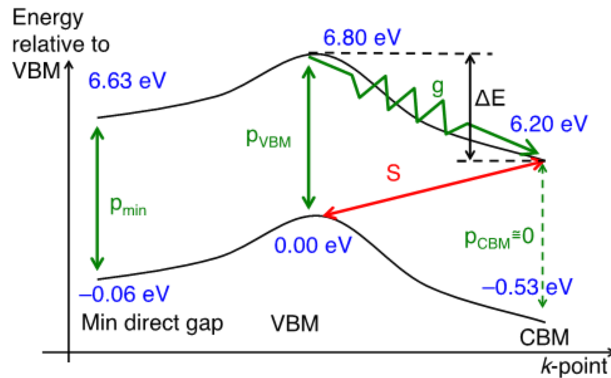

Figure 6.4 – Schematic band structure of BN near the band extrema. Although the bandgap is indirect, the phonon-assisted matrix element S is similarly strong to direct optical transition, and hence BN luminesces as a direct-gap material.

To confirm such a theoretical prediction, we compared the PL emission of h-BN with AlN, a direct bandgap semiconductor with similar energy bandgap values. Shown in Fig. 6.5(a) are the PL spectra of h-BN grown by plasma-assisted MBE (Sample C) and a commercial AlN epilayer sample (~4-μm thick, MSE Supplies LLC) measured under the same conditions at room temperature. It is seen that the PL intensity of few-layer h-BN is nearly 100 times stronger than that of thick AlN film. Variations of the PL intensity versus excitation power for both h-BN and AlN are further illustrated in Fig. 6.5(b), showing the much stronger emission of h-BN over a wide range of excitation conditions. These measurements provide unambiguous evidence that h-BN,

albeit an indirect bandgap semiconductor, can luminesce efficiently like a direct-gap material, which is attributed to the unusually strong electron-phonon coupling. Moreover, the radiative recombination rates can be further enhanced by the strong excitonic effect of h-BN. The efficient radiative recombination also suggests the presence of negligible surface dangling bonds and defects of h-BN grown by plasma-assisted MBE.

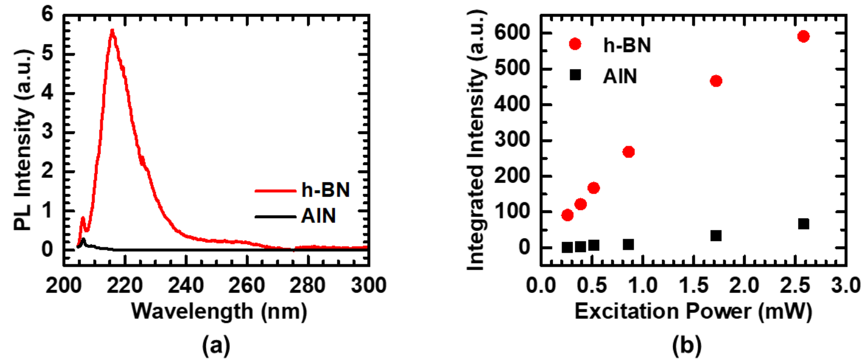

Figure 6.5 – (a) Room-temperature PL emission of Sample C (in red) as compared to a commercial AlN epilayer template on sapphire (in black). (b) Integrated PL intensity of both samples measured at various laser excitation powers.

6.6 Conclusion

We have demonstrated that superior quality h-BN can be obtained when grown at relatively high substrate temperature (~1300 °C) by plasma-assisted MBE. Significantly, our combined theoretical and experimental studies reveal that, even though the gap of h-BN is indirect, it luminesces as strongly as direct-gap materials. These findings provide new insight and further offer unique opportunities for the design and development of h-BN photonic and optoelectronic devices that can operate efficiently in the deep UV wavelengths.

Chapter 7 Hexagonal Boron Nitride Deep Ultraviolet Excitonic Light Emitting Diodes

7.1 Author Contributions and Copyright Disclaimer

At the time of writing, the work in this chapter is based on a manuscript that is in preparation. I designed, conducted and authored most of the work. Additional contributors to the experiments are Ping Wang, Ayush Pandey, Eric T. Reid and Zetian Mi, with past or current affiliation with the University of Michigan. The work was supervised by Z. M., who contributed to the design of the experiments. P. W. and A. P. contributed to the fabrication and characterization processes. E. T. R. conducted the polarization-resolving PL measurements. In addition, there are ongoing collaborations on the theoretical analyses and calculations by the Emmanouil Kioupakis and Mackillo Kira groups at the University of Michigan.

7.2 Background and Motivation

h-BN has shown tremendous promise given its unique characteristic of being both a 2D material and a wide-bandgap semiconductor, making it desirable for deep-UV optoelectronics and quantum photonics [289]. h-BN can be used to form heterostructures to address some of the critical challenges of Al(Ga)N-based systems [99], [290], [291]. To date, however, many fundamental material properties of h-BN remain unknown. Its bandgap energy remains under debate, and there are recent studies suggesting an indirect to direct band crossover for monolayer h-BN [23], [24]. In our previous study of this material, our atomistic calculations revealed that, even though the gap of h-BN is indirect, it can luminesce as strongly as direct-gap materials, because of the unusually strong phonon-assisted optical matrix element, which is nearly 600 times larger than that of Si

[100]. And indeed, we experimentally found that the PL intensity of a h-BN sample grown by MBE with a thickness on the order of nanometers is 10 to 100 times stronger than that of a high-quality 4-μm-thick commercially-grown direct-bandgap AlN, demonstrating the extraordinary potential of epitaxial h-BN for deep-UV optoelectronics and quantum photonics. In this regard, while the CL and PL of h-BN synthesized using a variety of methods have been studied in detail [14], [19], [257], [289], [292], there are to our best knowledge no reports on EL, from an electrically injected device with h-BN as its active region. This work addresses this missing piece of the puzzle, demonstrating an LED with h-BN EL.

7.3 Hexagonal Boron Nitride LED Structure

Given the current limitations of doping h-BN [16], [17], [293], and our success in previously demonstrating superior quality h-BN obtained by MBE on Ni substrate [100], surpassing that of exfoliated h-BN, the LED structure schematized in Fig. 7.1 was designed and experimentally attempted. It consists of the aforementioned h-BN/Ni, with the addition of an AlN p-i-n stack regrown on top. As such, the Ni substrate readily acts as the p-contact for hole injection through the h-BN active region [44], [99]. The n-type carriers injected from the top Ti/Au metal contact and n-AlGaN contact layer could also reach and recombine in the h-BN active region via electron overflow [65], [66]. It was found that this design was not only successful in demonstrating EL from h-BN for the first time, but in the process revealed previously unobserved peaks with relatively much stronger and narrower intensity. Their origin is currently being investigated.

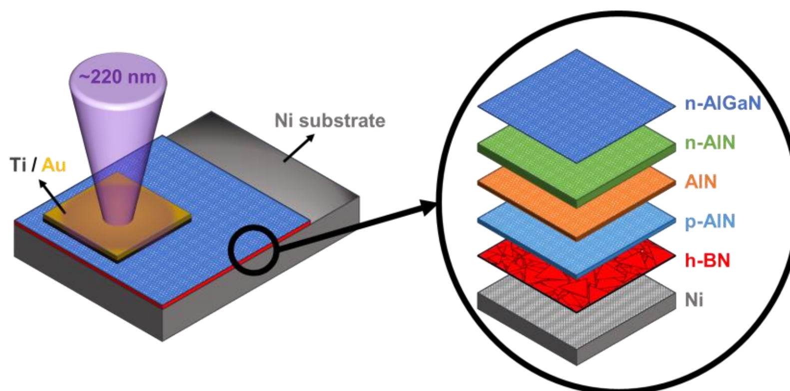

Figure 7.1 – Schematic of the LED structure consisting of a p-i-n AlN stack on h-BN on Ni substrate. The substrate acts as the p-contact, while thin Ti/Au metal pads act as n-contacts on top of the n-AlGaN contact layer.

7.4 Growth of the LED Structure

The details of the epitaxy of h-BN by using plasma-assisted MBE on Ni substrate are discussed elsewhere [100]. For this work, unannealed polycrystal Ni metallic wafers (MTI Corporation) were used. The substrate temperature was optimized to promote a dense surface coverage of the h-BN epitaxial domains, while maintaining the excellent material quality based on our previous studies. The AlN p-i-n stack consisted of a regrowth under nitrogen-rich and doping conditions similar to our previously reported AlN nanowires [44]. The substrate temperature was however reduced considerably (~600 °C), as this was identified as the solution for conformal and dense coverage of AlN, preventing paths for electrical shorts between the h-BN domains and grain boundaries in the Ni substrate. In the final minutes of the regrowth, the substrate temperature was further lowered, and a Ga flux was introduced to form a thin n-AlGaN contact layer [44]. The regrowth stack thickness is estimated to be ~100 nm. The SEM images in Fig. 7.2 taken using a Hitachi SU8000 system show the h-BN domains on Ni and the sample surface after the Al(Ga)N regrowth. Interestingly, the h-BN features are still perceptible, given the morphological differences

of AlN grown on h-BN or Ni. This is indicative that the h-BN were largely unaffected by the regrowth process.

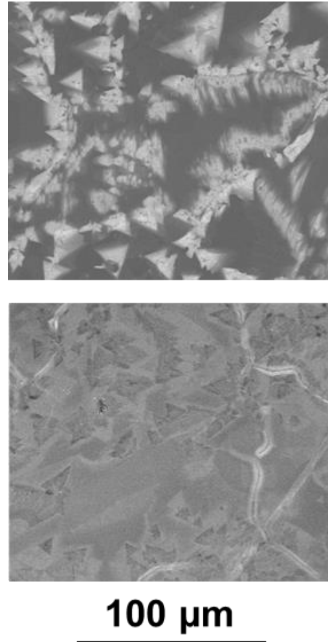

Figure 7.2 – SEM images of the h-BN/Ni surface before (top) and after (bottom) the AlN regrowth. The h-BN features remain noticeable and unchanged under relatively thick AlN.

7.5 Optical Properties of the h-BN

The optical properties of the epitaxial h-BN were characterized using variable excitation power and temperature-dependent PL spectroscopy with a 193 nm ArF excimer laser as the excitation source. The sample emissions were spectrally resolved by a Horiba iHR550 spectrometer and a UV-sensitive Symphony II CCD detector. Fig. 7.3(a) is a plot of the PL intensity integrated at ~220 nm at cryogenic and room temperatures. Fig. 7.3(b) shows an estimated IQE of ~50%, obtained by taking the ratio of integrated PL intensities at room and low temperatures, assuming near-unity quantum efficiency at low temperature [178]. From polarization-resolving PL, we found that the h-BN emission is predominantly TE polarized light

(see Fig. 7.3(c)), which is in direct contrast to the dominant TM polarized emission of AlN and Al-rich AlGaN [62], [63]. This offers significant advantages in achieving high LEE for potential deep-UV LEDs, compared to Al(Ga)N-based LED structures.

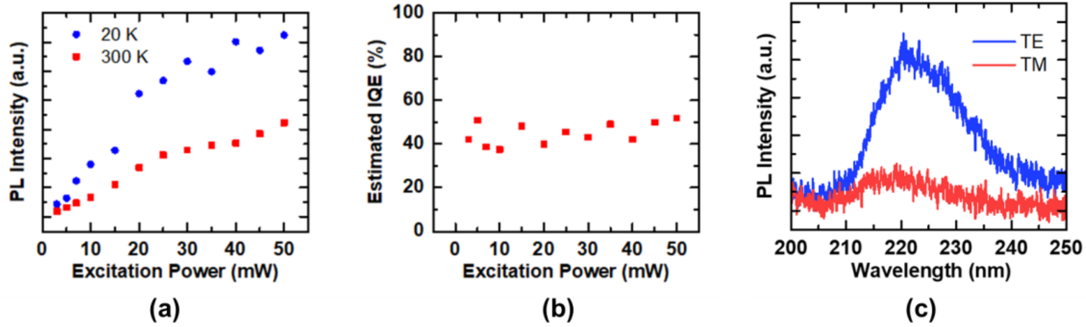

Figure 7.3 – (a) Integrated PL intensity at ~220 nm of h-BN/Ni at various excitation powers at cryogenic and room temperatures. (b) Estimated IQE of h-BN/Ni of ~50% at various excitation powers. (c) Polarization-resolving PL spectra of h-BN/Ni, showing predominantly TE polarized light being emitted.

7.6 h-BN LED Demonstration

The h-BN-based LED was fabricated by depositing topside n-metal contacts (15 nm Ti / 20 nm Au). Devices with sizes ranging from 0.1 to 1 mm^2 were defined using standard photolithography techniques. Fig. 7.4(a) shows the *I-V* characteristics of a 1 mm × 1 mm device, directly contacted with needle probes and a Keithley 2400 source meter, with its photograph included as the inset. The device exhibits excellent *I−V* characteristics, with low leakage current under reverse bias. The device turn-on voltage is ∼12 V. For comparison, previously reported planar *c*-plane AlN p-i-n LEDs can exhibit turn-on voltages as high as 20-30 V [42]. This confirms that although the AlN regrowth was conducted at relatively low temperature, its material and dopant properties are acceptable. Presented in Fig. 7.4(b) is the EL emission spectrum of the 1 mm × 1 mm LED device at room temperature, with the emitted light being collected by a UV-sensitive optical fiber coupled to the same spectrometer used for the PL studies. The device exhibits EL

emission at ~220 nm, consistent with the previous reports of CL and PL of h-BN. It is worth noting from the EL spectra that the peaks resolve at high injection only, which agrees with the LED design based on electron overflow for getting the n-carriers to recombine in the h-BN active region. Furthermore, these peaks were not measured from a control sample consisting of the AlN p-i-n stack grown directly on Ni without h-BN, supporting that they originate from h-BN.

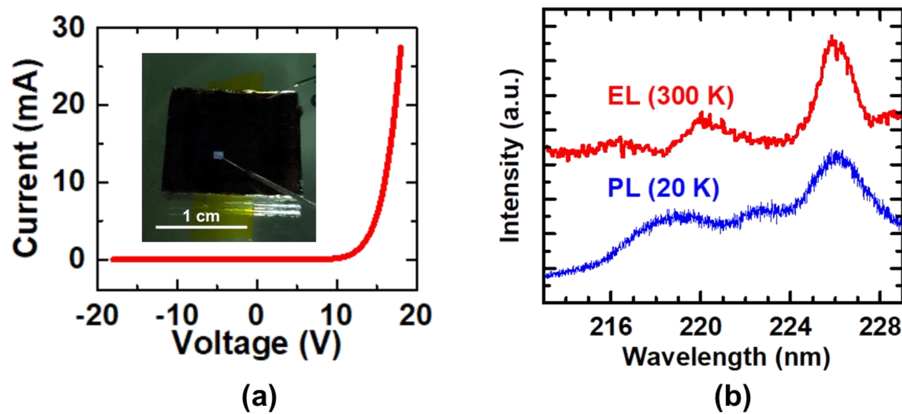

Figure 7.4 – (a) I-V curve of a 1 mm × 1 mm LED device, with a photograph of the device being probed as the inset. (b) Room-temperature EL spectrum of the device (in red) in the deep UV wavelength range, as compared to the low-temperature PL emission peaks (in blue) from a h-BN/Ni sample.

7.7 Conclusion

This first realization of an LED with h-BN electroluminescence is a major milestone for the next generation of deep-UV light emitters. It validates the favorable luminescence properties of this material, even though its bandgap may be indirect, and the critical role it has used alongside Al(Ga)N in forming heterostructures. It is also worth noting the strengths of using a scalable method, MBE, for the synthesis of these structures: a large number of devices were fabricated using standard techniques (without having to rely on electron-beam lithography) and probed using common needle probes without strict handling requirements.

Chapter 8 Summary and Future Work

8.1 Summary

This previous chapters in this thesis presented key studies and advances of the MBE growth of wide-bandgap III-Nitride materials, with characterization and measurement results focusing on deep-UV light emission. Improvements of the growth process of Al(Ga)N epilayers on lattice mismatched substrates are first realized, such that these thin films are now of comparable or better quality than samples reported by other established and relatively more mature technologies traditionally used for these materials. The MBE growth of h-BN was then investigated, both to obtain structurally and optically high-quality material and form heterostructures with AlN. A milestone result is the first demonstration of electroluminescence from h-BN embedded in an LED structure. This chapter provides an overview of suggested future work expanding on these studies.

8.2 Further Improvements in the MBE Growth of Al(Ga)N Epilayers

Chapter 3 presented a method for growing AlGaN epilayers with tunable Al composition. Chapter 4 discussed how in situ annealing steps can improve the AlN material quality. A first proposed plan for further optimizing the growth of AlGaN would be to incorporate the in situ annealing steps. Preliminary work, shown in Fig. 8.1, indicates improvements in PL intensity, which may be indicative of higher material quality.

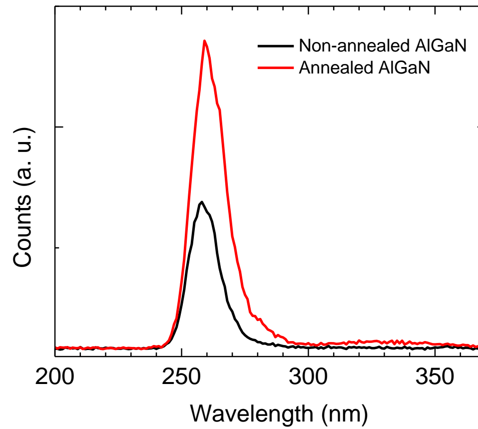

Figure 8.1 – PL spectra of AlGaN epilayer samples grown with (in red) and without (in black) in situ annealing in the MBE chamber. (Source: courtesy of Ayush Pandey, University of Michigan)

An alternative approach to the in situ annealing process during growth would be a high temperature annealing of the sample post-growth. Preliminary studies of this process however showed severe decomposition and roughening of the sample. Depositing a thin (20 nm) aluminum oxide capping layer by atomic layer deposition (ALD) prior to the annealing process provided effective surface protection. When the samples were re-loaded into the MBE chamber and annealed at up to 1800 °C, changes could be seen in the XRD and PL characteristics. The (002) rocking curve peak FWHM remains constant, but eventually increases once the annealing temperature becomes too high (>1700 °C). The (102) peak however keeps narrowing and the PL intensity keeps increasing with higher temperatures. This is shown in Fig. 8.2 and indicates that with an optimal annealing temperature post-growth, further improvements in AlN material quality can be achieved, which would be relevant for AlN/sapphire photonic applications [294].

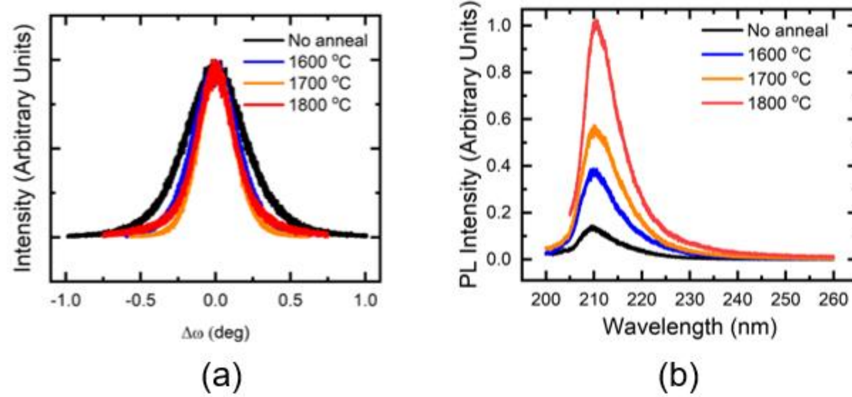

Figure 8.2 – (a) XRD (102) rocking curves of AlN films annealed at different temperatures, showing a reduction in linewidth compared to the as-grown sample. (b) Normalized PL spectra of AlN annealed at different temperatures, showing stronger intensities with increasing annealing temperature. (Source: courtesy of Eric T. Reid, University of Michigan)

Expanding of the improvements of the AlN epilayers on sapphire, a next step would be to grow the AlGaN epilayers on that platform instead of the commercially available templates on sapphire. With superior optical properties, a reduction in dislocation densities, and the option to grow the AlGaN on AlN stack directly without forming an interface due to the exposure of the AlN template surface to air, improvements in the AlGaN-based UV LEDs are expected.

8.3 Doping of MBE-Grown AlN Epilayers

Based on the AlGaN growth method established in Chapter 3, the charge carrier transport properties of Mg-doping the wide-bandgap AlGaN films were studied [295], and enhanced p-type doping efficiencies were demonstrated by utilizing a metal-semiconductor junction assisted epitaxy process [194]. This has yet to be accomplished for AlN. Even Si-doped n-AlN currently remains elusive irrespective of method used [51].

8.4 Elucidating the Luminescence and Excitonic Properties of h-BN

The h-BN LED measurements presented in Chapter 7 reveal additional luminescence peaks previously unobserved from theoretical, CL or PL reports of h-BN, [19]–[21], [26], [257], [276], [289], [296]–[299], nor any type of luminescence from AlN [70], [71], [226]. The longer-range EL spectrum is shown in Fig. 8.3. These peaks are of stronger intensity and narrower linewidth than the BN EL emissions around 220 nm. More involved studies and theoretical calculations would be necessary to elucidate the mechanisms at play. Given the strong exciton effects in h-BN [300]–[302], one proposed explanation is that these luminesce peaks originate from indirect excitons at the AlN and h-BN interface with possible phonon sidebands, as illustrated in Fig. 8.4(a). Given the unusually strong electron-phonon coupling in h-BN, and large exciton binding energies compared to the other III-Nitrides, other previously unseen interactions may arise, for example involving polarons [293], [303], [304], as illustrated in Fig. 8.4(b).

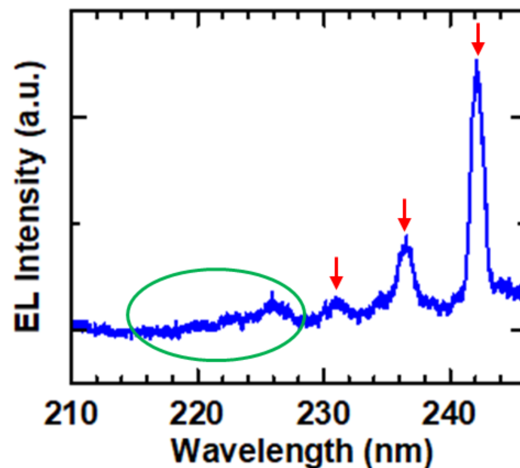

Figure 8.3 – EL spectrum of the h-BN LED presented in Chapter 7. Circled in green is the emission range that is consistent with the luminescence properties of h-BN. The red arrows highlight additional lower-energy peaks previously unseen from luminescence of h-BN or AlN.

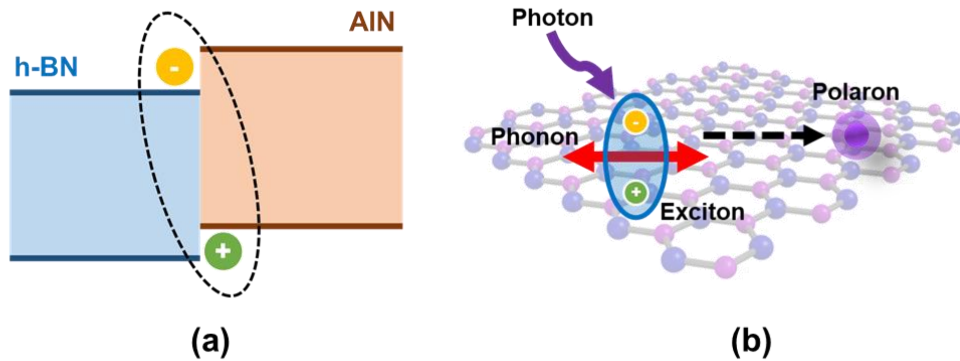

Figure 8.4 – (a) Flat-band schematic of the h-BN/AlN interface, showing the formation of an indirect exciton between an electron in h-BN and hole in AlN. (b) Illustration of possible polarons in the h-BN lattice from phonon-exciton coupling.

8.5 Towards Wafer-Scale Monolayer h-BN

As mentioned in Chapter 1, ML BN is desired for a number of applications, especially if it can be grown at the wafer scale [305]–[307]. Using the high-temperature MBE approach similar to the one described in this thesis but on highly oriented pyrolytic graphite (HOPG) substrates, linearly aligned, uniform ML BN nanoribbons are grown along the HOPG steps. This work in ongoing. For the h-BN on Ni used in Chapter 7, preliminary AES mapping results indicate h-BN coverage even around the triangular domains, although much thinner, possibly a monolayer. Another indication of this being achievable was observed during the growth optimization of h-BN on polycrystal Ni substrates. When the growth temperature was unintendedly too high, the triangular domains appeared to have more spread, with almost complete surface coverage, as shown in the SEM image in Fig. 8.5. Further efforts focusing in this temperature range, and for example reducing the growth duration, may lead to controllable ML BN growth with full wafer coverage.

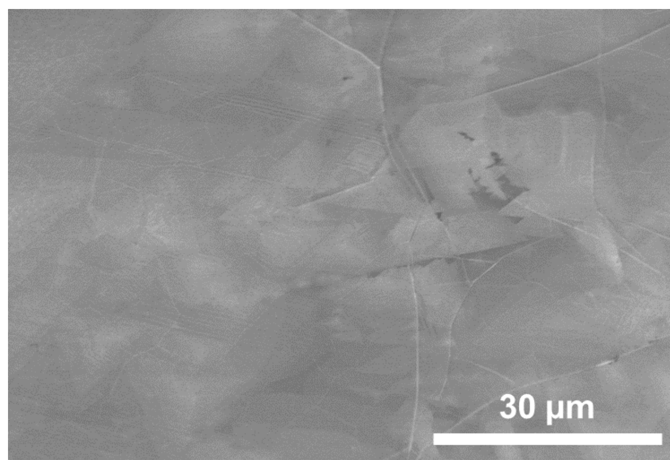

Figure 8.5 – SEM image of h-BN on Ni grown at unintendedly high temperature, showing a spread of the nucleation domains and more complete surface coverage.

8.6 Hybrid h-BN/Al(Ga)N Heterostructures

Chapter 5 presented notable enhancements of AlN nanowires when combined with h-BN. A promising characteristic was the achievement of p-type conduction suitable for deep-UV applications without the challenges associated with Mg doping of AlN. A next step would therefore be to attempt similar heterostructures with Al(Ga)N epilayers to validate the scalability of this approach to planar UV LEDs.

While the AlN/h-BN on Ni samples were robust enough for device fabrication and measurements without any processing or handling concerns, it was observed that the flakes of material can be mechanically delaminated if done intentionally, as shown in the SEM images of Fig. 8.6. h-BN domains are still visible on the Ni substrate in regions where the AlN was removed. It is currently unclear whether some layers of h-BN peel off along with the AlN, therefore requiring additional studies using some of the more advanced characterization techniques. This type of lift off can be a pathway for free-standing III-Nitride materials or for transfer onto different substrates. In addition, if it is found that h-BN indeed peels off with the AlN, it would become a way to

integrate the conventional III-Nitrides in van der Waals heterostructures similar to the 2D layered materials, enabling a new realm of possibilities. This type of studies have been successfully conducted in the past by other groups for (In)GaN with graphene [308], [309] or even h-BN [310], [311], but remains a challenge for AlN. In addition, none of these reports are by MBE, which would offer advantages in terms of the controllability of the different layers and the interfaces.

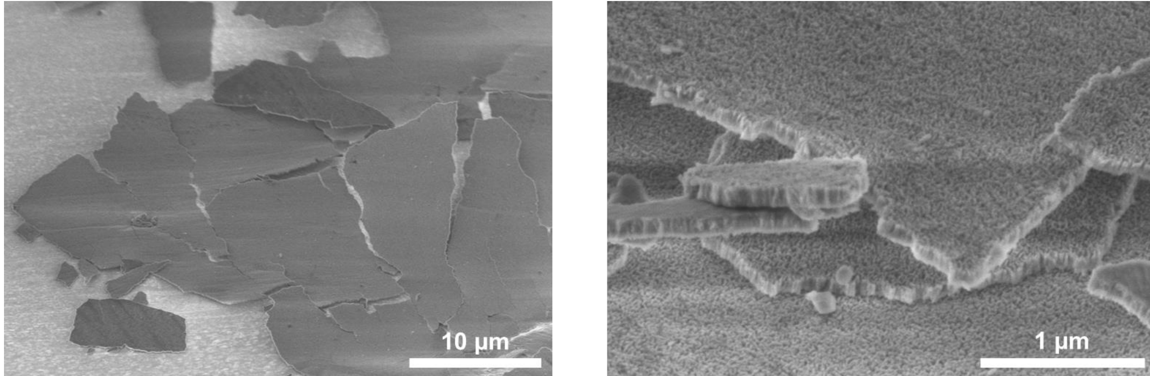

Figure 8.6 – SEM images at low (left) and high (right) magnifications of the mechanically delaminated material grown on Ni.

8.7 Boron Containing III-Nitride Alloys

Boron containing III-Nitride ternary and quaternary alloys are appealing for the additional degree of freedom that such compounds can offer in the design of heterostructures. Theoretical and experimental studies on boron containing thin-film structures have been previously reported. Benefits of B(In,Ga,Al)N materials include the possibility of varying the lattice constant for lattice matching with AlN and SiC substrates [312]–[315], bandgap engineering for refractive index tuning and strain compensation [32], [312], [316], and decreased built-in internal polarization fields [317]. Experimental demonstrations of B(In,Ga,Al)N, mainly grown by MOVPE, have however been limited to low boron compositions, as further increases have led to a degradation of the material quality and structural properties from strain induced defects due to segregation and

phase separation effects [31], [316], [318]–[320]. While most of these reports focused on ternary BGaN or BAlN, avoiding the additional complexities and challenges of quaternary alloys, a recent theoretical study proposes that BAlGaN can in fact be a promising material for Al(Ga)N heterostructures [321]. These results indicate that B incorporation into AlGaN alloys is in fact not thermodynamically any less favorable than into AlN or GaN. Yet, lower B alloy compositions are sufficient in BAlGaN to achieve benefits such as lattice matching with AlN, or maintaining predominantly TE-polarized light emission.

Based on these findings, preliminary studies were conducted on the MBE growth of BAlGaN. The initial steps were similar to the process described in Chapter 3 but conducted in the e-beam evaporator equipped GENxplor system to introduce some B in the second half of the growth. Figure 8.7 shows a sample with B incorporation and a control AlGaN sample without introducing a B flux. The B compositions were estimated based on the AlGaN growth rate and B deposition rate. Severe phase separation was observed for a sample with ~5% B composition, not shown, consistent with the previous reports of BGaN and BAlN. The surface morphology was reasonable for the sample with ~1% B composition, but not as smooth as AlGaN. Interestingly, the RHEED patterns during growth were very indicative of the surface morphology.

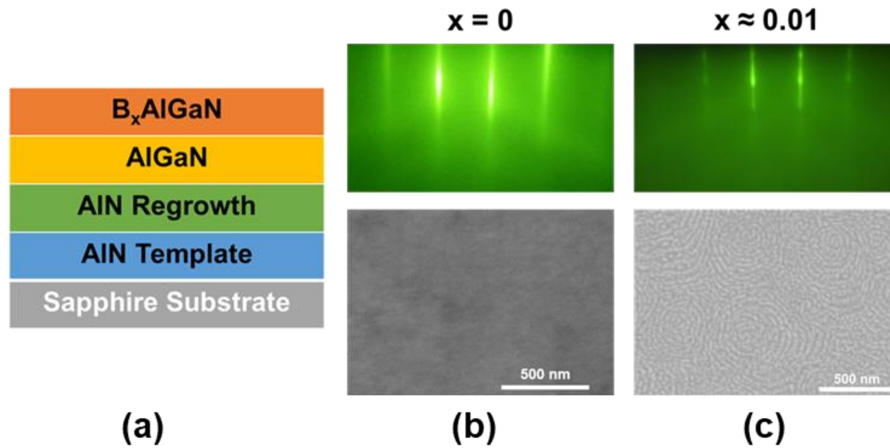

Figure 8.7 – (a) Schematic of the layer stacking of the grown samples (not to scale). (b-c) Top: RHEED pattern during the growth of the topmost layer; bottom: SEM surface image of the samples post-growth for B compositions of (b) 0% (AlGaN-only) and (c) ~1%.

XPS characterization of the sample from Fig. 8.7 (c) confirms the presence of B at ~1%, as shown in Fig. 8.8(a). The XRD scan in Fig. 8.8(b) for this sample shows some differences compared to the AlGaN sample, although it is not certain whether this is due to alloying, strain or both. The PL spectrum of the sample in Fig. 8.8(c) shows two distinct peaks at ~240 and 300 nm. The first is consistent with the underlying AlGaN, while the second emerges from the BAlGaN layer. Measuring PL emission from this preliminary sample is promising, as previous reports of incorporating B often indicate a suppression of luminesce due a degradation of the material quality.

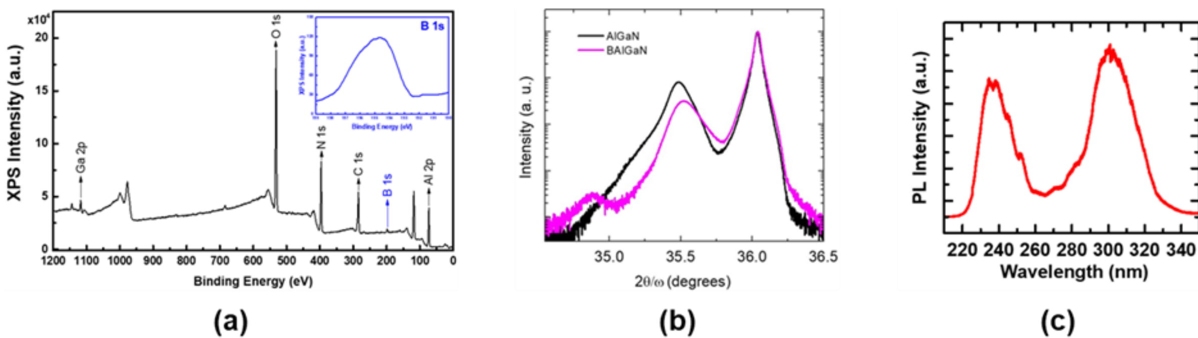

Figure 8.8 – (a) XPS survey scan of the sample with a B composition ~1%. The inset shows the high-resolution scan of the B 1s peak with a binding energy of ~195 eV. (Source: courtesy of Ping Wang, University of Michigan) (b) XRD scans around the (0002) peak for the AlGaN and BAlGaN samples. The

common peak at 36° corresponds to the AlN template the samples were grown on. (Source: courtesy of Ayush Pandey, University of Michigan) (c) Room-temperature PL spectrum of the MBE-grown BAlGaN sample with ~1% B composition. The peak at ~240 nm is consistent with that of the underlying AlGaN, while the peak ~300 nm emerges from the BAlGaN layer. (Source: courtesy of Ayush Pandey, University of Michigan)

Appendices

Appendix A Illustration of the Electromagnetic Spectrum

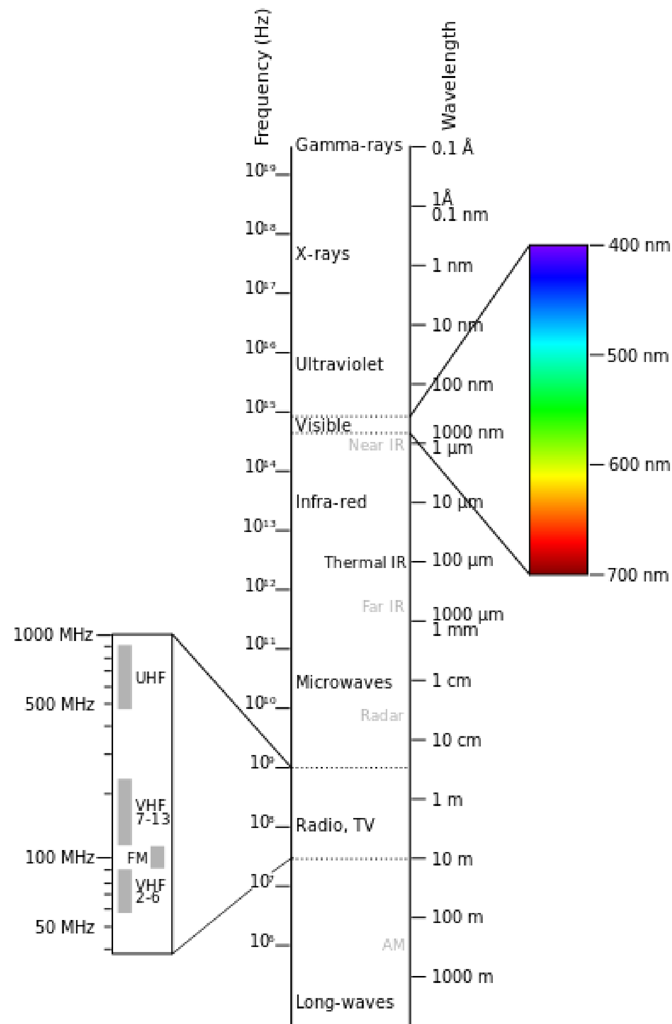

Figure A.1 – Illustration of the electromagnetic spectrum. (Source: Wikipedia.org)

Appendix B Fabrication Steps of UV LEDs

The following steps describe the basic process used in the fabrication of the h-BN/AlN-based LED devices presented in this thesis. For high performance devices, a more advanced fabrication process and extra steps are required, which, however, are beyond the scope of this thesis work.

1. Dice or cleave samples to the desired size (optional)
2. Standard solvent cleaning (without delay between steps)
    a. Acetone (5 minutes)
    b. Methanol (5 minutes)
    c. Deionized water rinse (5 times)
    d. Nitrogen drying
3. Photoresist spin coating
    a. Resist: S1813
    b. Speed/Time: 4000 RPM, 30 seconds
    c. Soft bake: 115 °C, 60 seconds
4. Exposure using a suitable photomask
    a. Hard contact
    b. 4.5 seconds
5. Development
    a. Developer: AZ 726 (or MF 319)

    b. Duration: 30-60 seconds (verify under optical microscope)
    c. Deionized water rinse and nitrogen drying
6. Surface cleaning
    a. Chemical: Hydrochloric acid (HCl)
    b. Duration: 1 minute
    c. Deionized water rinse and nitrogen drying
7. Thin contact metal deposition
    a. Load samples on 30° angled holder using double-sided Kapton tape
    b. Carefully mount into the e-beam evaporator, pump down
    c. Deposit metals sequentially
        i. Typical n-contact stack: Ti / Au (15 nm / 20 nm)
        ii. Typical p-contact stack: Ni / Au (15 nm / 10 nm)
    d. Remove samples
8. Lift-off process
    a. Chemical: heated acetone (or Remover PG / 1165 if stubborn)
    b. Gently move around until lift off occurs
    c. Place samples in clean acetone
    d. Transfer into methanol
    e. Deionized water rinse and nitrogen drying
9. Inspect sample with optical microscope

Note: the devices are now ready to be tested using needle probes. Light would be emitted through the thin metal contact pad.

Appendix C Bandgap and Lattice Constant Relation of the III-Nitride Materials

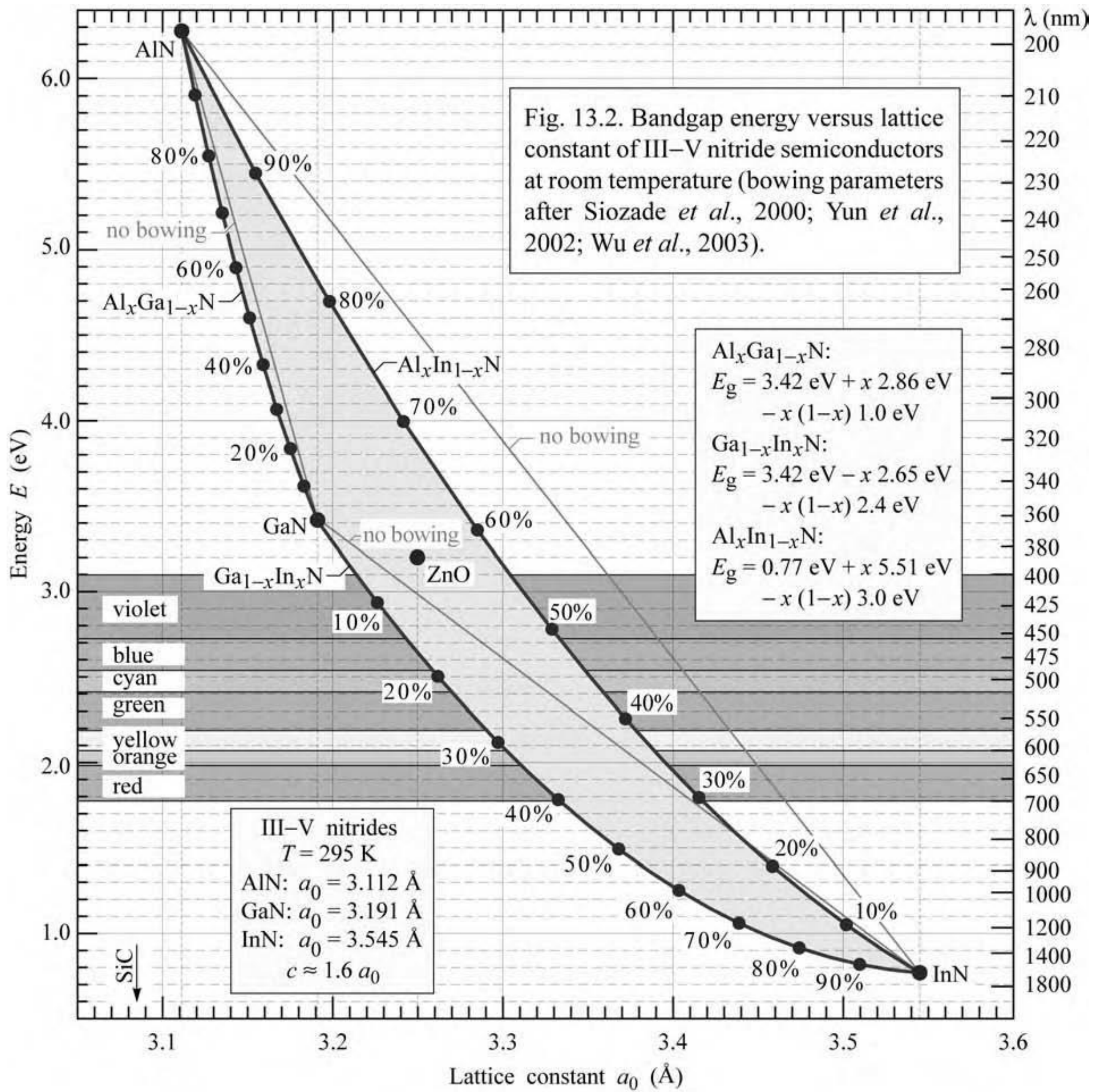

Figure A.2 – Bandgap and Lattice Constant Relation of the III-Nitride Materials. (Source: [3])

Appendix D Useful Lookup Table of $Al_xGa_{1-x}N$ Properties

Table A.1 – Table of calculated $Al_xGa_{1-x}N$ bandgap energy (E_g), PL wavelength and XRD 2Theta-Omega angle for various compositions.

AlxGa1-xN			
x	Eg (eV)	PL (nm)	XRD (deg)
0	3.40	365	34.50
0.02	3.43	361	34.53
0.04	3.46	358	34.56
0.06	3.49	355	34.59
0.08	3.53	351	34.62
0.1	3.56	348	34.65
0.12	3.60	345	34.68
0.14	3.64	341	34.71
0.16	3.67	338	34.74
0.18	3.71	334	34.77
0.2	3.75	330	34.80
0.22	3.79	327	34.83
0.24	3.83	323	34.86
0.26	3.88	320	34.89
0.28	3.92	316	34.92
0.3	3.97	313	34.95
0.32	4.01	309	34.98
0.34	4.06	305	35.01
0.36	4.11	302	35.04
0.38	4.16	298	35.07
0.4	4.21	295	35.10
0.42	4.26	291	35.13
0.44	4.31	288	35.16
0.46	4.37	284	35.19
0.48	4.42	281	35.22
0.5	4.48	277	35.25
0.52	4.53	274	35.28
0.54	4.59	270	35.31
0.56	4.65	267	35.34
0.58	4.71	263	35.37
0.6	4.77	260	35.40
0.62	4.83	257	35.43
0.64	4.89	253	35.46
0.66	4.96	250	35.49
0.68	5.02	247	35.52
0.7	5.09	244	35.55
0.72	5.15	241	35.58
0.74	5.22	237	35.61
0.76	5.29	234	35.64
0.78	5.36	231	35.67
0.8	5.43	228	35.70
0.82	5.50	225	35.73
0.84	5.58	222	35.76
0.86	5.65	219	35.79
0.88	5.73	217	35.82
0.9	5.80	214	35.85
0.92	5.88	211	35.88
0.94	5.96	208	35.91
0.96	6.04	205	35.94
0.98	6.12	203	35.97
1	6.20	200	36.00

Appendix E Schematics of Measurement Setups

UV-Sensitive PL Setup

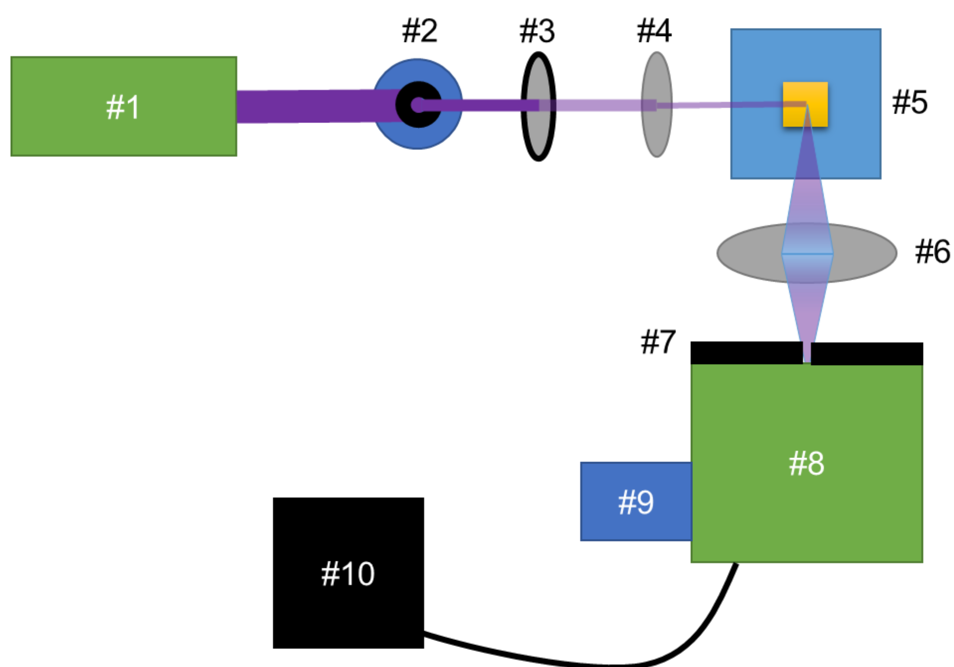

Figure A.3 – Schematic of the PL setup for UV measurements. Table A.2 lists the components. For temperature-dependent PL, the sample needs to be loaded into the cryostat, pumped down and then cooled down using a closed-loop helium compressor and temperature controller.

Table A.2 – List of components for Fig. A.3.

#	Component
1	193 nm laser (Coherent Inc.)
2	Pinhole (Thorlabs, Inc.)
3	Attenuator wheel (Thorlabs, Inc.)
4	Focusing lens (on 3D stage, Thorlabs, Inc.)
5	Sample holder (on 2D stage, or inside cryostat)
6	Collection lens (on 3D stage, Thorlabs, Inc.)
7	Spectrometer entrance slit
8	Spectrometer (Horiba iHR 550)
9	CCD Detector (Horiba Symphony II)
10	Computer (Horiba SynerJY software)

UV LED EL Setup

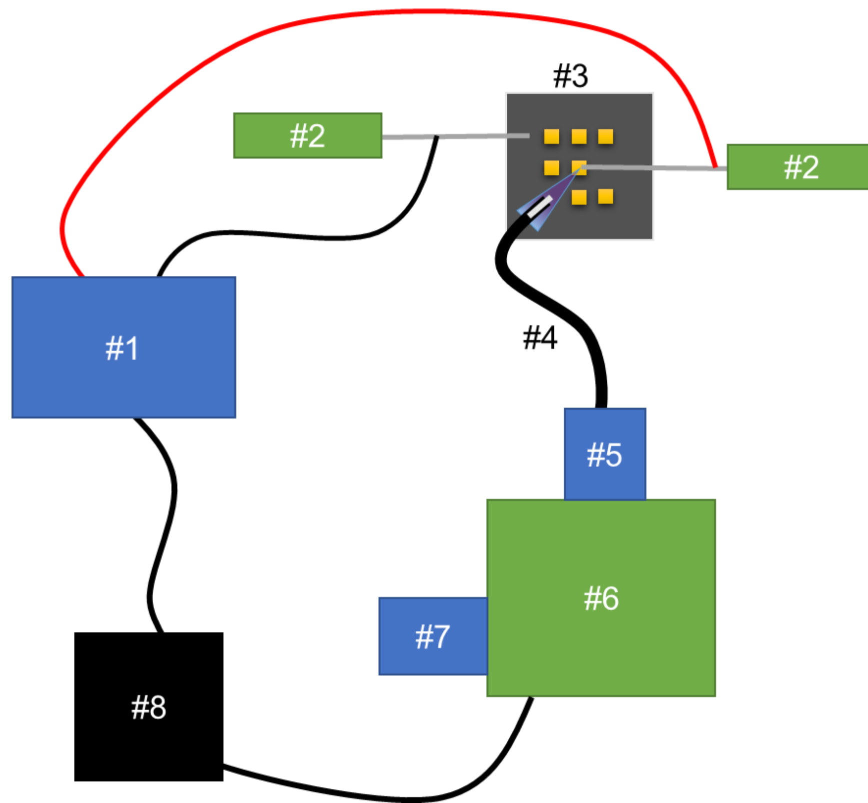

Figure A.4 – Schematic of the EL setup for UV LED measurements. Table A.3 lists the components.

Table A.3 – List of components for Fig. A.4.

#	Component
1	Source meter (Keithley 2400)
2	Needle probes (The Micromanipulator Company)
3	Sample (with metal contacts)
4	Optical fiber (Ocean Optics XSR)
5	Fiber adapter (Horiba, Ltd.)
6	Spectrometer (Horiba iHR 550)
7	CCD Detector (Horiba Symphony II)
8	Computer (Horiba SynerJY and Keithley KickStart software)

Appendix F Supporting Information for Chapter 5

Section 1 – Band Alignment Between h-BN and Al(Ga)N

The structure being studied in this work is schematically illustrated in Fig. A.5(a), consisting of n-type GaN, n-type AlN, undoped AlN and undoped (p-type) h-BN respectively along the growth direction. Of particular interest is the band alignment between AlN and h-BN. As can be seen in Fig. A.5(b), a type I alignment (straddling gap) between AlN and h-BN is favorable for both effective hole injection from the p-type behaving h-BN, and as an electron blocking layer for the carriers injected from the n-contact, providing effective carrier confinement. The use of h-BN in this heterostructure therefore provides crucial benefits that were previously lacking in AlN-based deep UV light emitting devices. It is worth noting that the exact bandgap of h-BN remains under debate [16], [17], [19], [20], [22]. The experimental report of ~6.5 eV has been used to construct the proposed band diagram.

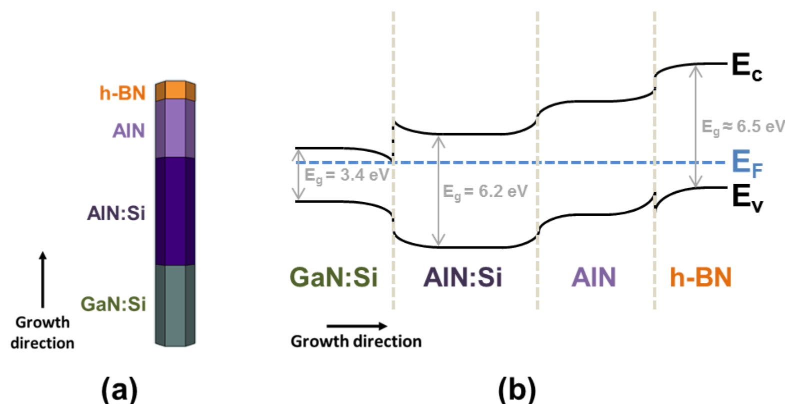

Figure A.5 – (a) Schematic of the AlN/h-BN nanowire heterostructure, with the growth direction denoted by the black arrow. (b) Flat energy band diagram of this heterostructure, highlighting the band alignment between the different layers along the growth direction denoted by the black

arrow. E_c, E_v, E_F and E_g are the conduction band minima, valence band maxima, Fermi level and bandgap energies, respectively.

Section 2 – Boron Vacancies in h-BN

The undoped h-BN epilayer in this study exhibits p-type behavior, which is ascribed to the presence of boron vacancies. While h-BN is typically regarded as a dielectric material [241], native defects such as nitrogen vacancy (V_N) and boron vacancy (V_B) have been known to form unintentionally in h-BN during the growth process. The formation of V_N, however, has been suppressed using nitrogen-rich epitaxy conditions. It has also been demonstrated that V_B acts as a triple acceptor [25]. Thus, it is reasonable to interpret that V_B is responsible for the p-type conduction in current h-BN epilayer.

Attaccalite et al. have conducted a theoretical study on the signature of defects in the optical spectra of h-BN specifically for nanostructures [25]. Of particular note is their result on the position of the defect quasiparticle energies within the band gap for a boron vacancy. Taking into account their theoretical estimation of the bandgap energy, the unoccupied levels they have identified approximately match the PL peaks at 260 nm (4.77 eV), 290 nm (4.28 eV) and 380 nm (3.26 eV) of the AlN/h-BN heterostructure and h-BN thin film grown under similar conditions on SiO_x/Si(001) substrate (see Section 4). The proposed energy diagram in Fig. A.6 illustrates the optical processes of these observed impurity emission lines. Interestingly, an additional level caused by a B vacancy in this theoretical model is an occupied level at ~0.15 eV, which is very close to the valence band edge. This is consistent with another theoretical study that places the Fermi level close to the valence band maximum [241], as would be the case in a p-doped semiconductor, thus elucidating the unusual p-type behavior of this material.

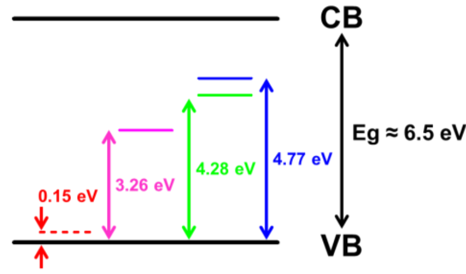

Figure A.6 – Energy diagram of the optical processes observed from the impurity emission lines of the h-BN reported in this study, which match the energy levels theoretically attributed to boron vacancies. Eg is the bandgap energy, and CB and VB are the conduction and valence band edges, respectively.

Section 3 – Structural Characterization of h-BN

STEM low-loss EELS spectrum

Figure A.7 shows the low-loss EELS spectrum from the boron nitride layer in the AlN/h-BN heterostructure, exhibiting the $\pi + \sigma$ bulk plasmon peak (~25 eV) and the π^* plasmon (~8 eV), also indicative of h-BN. The shoulder towards lower energy of the bulk plasmon peak and its slight shift towards lower energy can be attributed to surface plasmons or the presence of carbon contaminant, and delocalized bulk plasmon signal from the adjacent AlN (at 21 eV), respectively.

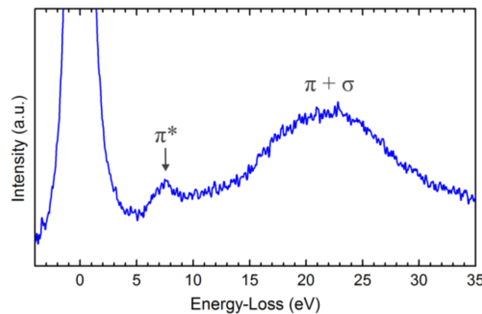

Figure A.7 – Low-loss EELS spectrum from the BN layer in the AlN/h-BN heterostructure

Electron microscopy of h-BN on SiO_x/Si(001) substrate

The h-BN thin film used for the Hall effect measurements was grown on SiO_x/Si(001) substrate using similar conditions as the h-BN grown on AlN nanowires. STEM imaging was performed on this h-BN/SiO_x/Si(001) sample, prepared in cross-section by wedge-polishing using an Allied High Tech MultiPrep System, then cleaned with low-energy Ar-ions with a Technoorg Linda Gentle-Mill. The detailed characterization results in Fig. A.8 validate that this h-BN material is identical to the one grown on the surface of the AlN nanowires.

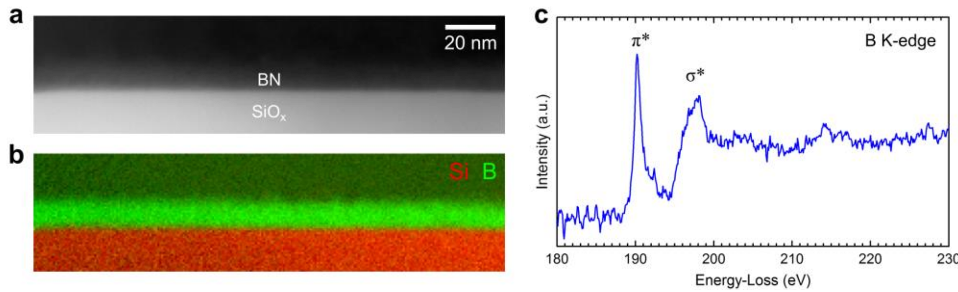

Figure A.8 – (a) STEM-HAADF image of the h-BN layer grown on a SiO_x/Si(001) substrate. (b) EELS elemental mapping of the distribution of B and Si at the h-BN/SiO_x interface using the B K and Si $L_{2,3}$-edges, respectively. (c) Core-loss EELS spectra of the B K-edge from the BN layer showing both π and σ* components, confirming h-BN.*

Section 4 – Photoluminescence Properties of h-BN

Impact of h-BN on the optical properties of AlN nanowires

Comparing the dominant emission at ~210 nm of the AlN/h-BN core-shell nanowire heterostructure and identical AlN nanowires without BN incorporation (Fig. A.9(a)), it is observed that the former exhibits enhanced photoluminescence emission due to the enhanced charge carrier confinement and suppressed surface recombination [49]. To better understand the effect of the h-BN segment on the PL emissions, multiple samples were studied with identical AlN nanowires but different h-BN thicknesses and growth temperatures. As can be seen in Fig. A.9(b), other than the

AlN free exciton emission at ~210 nm, the emergence of longer wavelength peak at ~290 nm can be observed, and as such attributed to defect levels from the h-BN layer [322]. Comparing these samples, this defect-induced peak is lower for the sample with the h-BN segment grown at higher temperature. Coincidentally, this sample also exhibited the strongest enhancement of the AlN free excitonic emission peak. While further optimization may be possible, these samples already provide important insight into the growth and optical characteristics of a thin h-BN layer.

PL spectrum of h-BN on SiO_x/Si(001) substrate

Figure A.9(c) shows the room-temperature PL spectrum of the previously discussed h-BN/SiO_x/Si(001) sample (see Sections 2 and 3), also excited using a 193 nm laser. Compared to the AlN/h-BN heterostructure, this sample does not show emission at 210 nm due to the absence of AlN nanowires, but exhibits strong emission at ~260 nm and 380 nm, which can also be attributed to defect levels from the h-BN thin film.

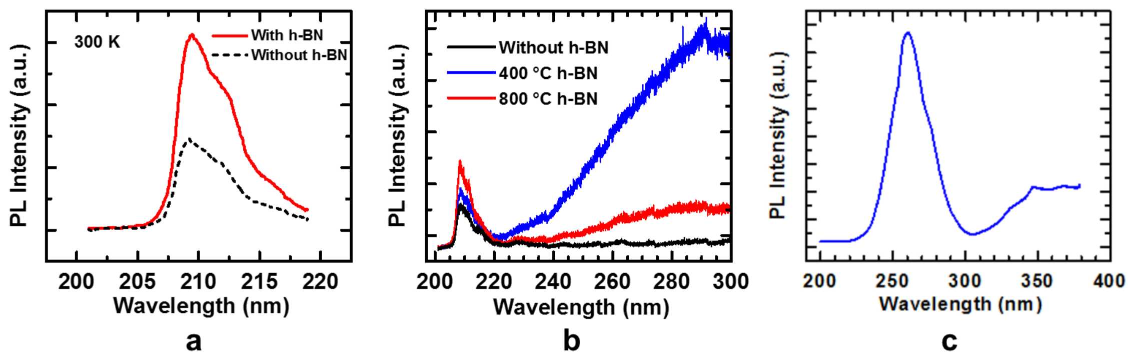

Figure A.9 – (a) Room-temperature PL spectrum centered at 210 nm of the AlN/h-BN nanowire sample (in solid red) and an identical AlN nanowire sample without h-BN (in dashed black). (b) Extended-range PL spectra highlighting the band-edge and defect-related emissions of two AlN/h-BN nanowire samples with h-BN growth temperatures of 400 °C (in blue) and 800 °C (in red). The spectrum of an equivalent AlN nanowire sample without h-BN is included (in black) for comparison. (c) PL spectrum of h-BN grown on a SiO_x/Si(001) substrate, showing the dominance of boron-vacancy related transition.

Section 5 – Electrical Properties of the AlN/h-BN LED

Figure A.10 shows the *I-V* characteristics of the AlN/h-BN LED using a semi-log plot, highlighting the current density when the device is forward and reverse biased.

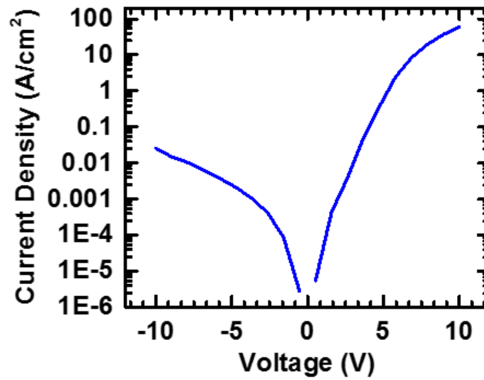

Figure A.10 – I-V curve of the same device shown in Fig. 5.4(b) in semi-log scale.

Section 6 – Transmittance of h-BN in the Deep-UV Spectral Range

One important motivation in using h-BN for deep-UV photonics is for its use as a transparent electrode in this spectral range. To validate this claim, UV-Vis spectroscopy measurements were conducted on 10 nm h-BN films grown on sapphire under similar growth conditions. A Cary 5000 UV-Vis system was used and the spectra were baseline corrected with air. The results show that the transmittance at 210 nm of h-BN sample is significantly higher than a GaN on sapphire sample of equal thickness, typically used as the p-contact layer in deep-UV LEDs. The measurement results are presented in Fig. A.11, and the transmittance curves extracted from these results are shown in Fig. A.12.

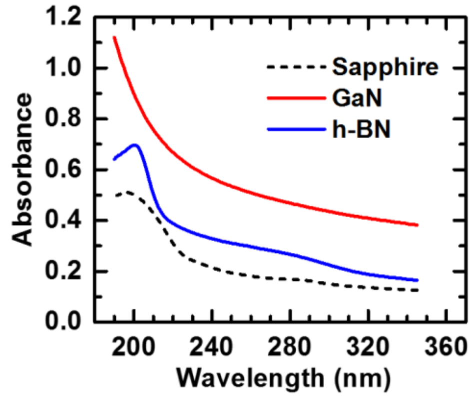

Figure A.11 – Absorbance spectrum of a bare sapphire substrate (in dashed black), h-BN on sapphire substrate (in solid blue) and GaN on sapphire substrate of equivalent thickness (in solid red).

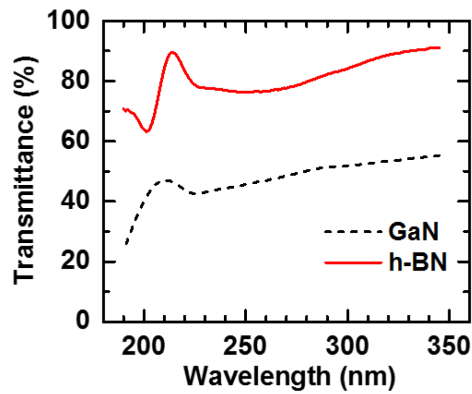

Figure A.12 – Transmittance curves of GaN and h-BN derived from the absorbance spectra in Fig. A.11 using Beer's law and subtracting the absorbance spectrum of the bare sapphire substrate as a baseline.

Appendix G List of Abbreviations

0D: zero-dimension(al)

1D: one-dimension(al)

2D: two-dimension(al)

3D: three-dimension(al)

AES: Auger electron spectroscopy

AFM: atomic force microscope / microscopy

ALD: atomic layer deposition

AlGaN: aluminum gallium nitride

AlN: aluminum nitride

BEP: beam equivalent pressure

BF: bright field

BFM: beam flux monitor

BN: boron nitride

BSE: Bethe-Salpeter equation

c-BN: cubic boron nitride

CAR: continuous azimuthal rotation

CBM: conduction band minimum

CCD: charge-coupled device

CH: crystal-field split-off hole

CIE: carrier injection efficiency

CL: cathodoluminescence

CVD: chemical vapor deposition

DF: dark field

DFPT: density functional perturbation theory

EBL: electron blocking layer

EDS/EDX: energy dispersive X-Ray spectroscopy

EELS: electron energy loss spectroscopy

EIES: electron impact emission spectroscopy

EL: electroluminescence

ELO: epitaxial lateral overgrowth

EQE: external quantum efficiency

FIB: focused ion beam

FWHM: full width at half maximum

GaAs: gallium arsenide

GaN: gallium nitride

h-BN: hexagonal boron nitride

HAADF: high-angle annular dark-field

HCl: hydrochloric acid

HH: heavy hole

HOPG: highly oriented pyrolytic graphite

HVPE: hydride vapor phase epitaxy

I-V: current-voltage

InGaN: indium gallium nitride

InN: indium nitride

IQE: internal quantum efficiency

IR: infrared

ITO: indium tin oxide

LD: laser diode

LED: light-emitting diode

LEE: light extraction efficiency

LH: light hole

LO: longitudinal optical

MBE: molecular beam epitaxy

MEE: migration-enhanced epitaxy

MIS: metal-insulator-semiconductor

ML: monolayer

MOCVD: metal organic chemical vapor deposition

MOVPE: metalorganic vapor-phase epitaxy

MQW: multiple quantum well

MSE: mean squared error

OM: optical microscope / microscopy

PBN: pyrolytic boron nitride

PL: photoluminescence

PPA: peak pairs analysis

PSS: patterned sapphire substrate

PVT: physical vapor transport

QCM: quartz crystal monitor

r-BN: rhombohedral boron nitride

RF: radio frequency

RGA: residual gas analyzer

RHEED: reflection high-energy electron diffraction

RMS: root mean square

SEM: scanning electron microscope / microscopy

SiC: silicon carbide

SIMS: secondary-ion mass spectrometry

SL: superlattice

SRH: Shockley-Read-Hall

STEM: scanning transmission electron microscope / microscopy

TD: threading dislocation

TDD: threading dislocation density

TE: transverse electric

TEM: transmission electron microscope / microscopy

TIR: total internal reflection

TM: transverse magnetic

UHT: ultra-high temperature

UHV: ultra-high vacuum

UV: ultraviolet

UV-Vis: ultraviolet-visible

VBM: valence band maximum

w-BN: wurtzite boron nitride

WPE: wall-plug efficiency

XPS: X-ray photoelectron spectroscopy

XRD: X-ray diffraction

Bibliography

[1] S. O. Kasap, *Principles of electronic materials and devices*. Boston: McGraw-Hill, 2006.

[2] G. W. Neudeck, *The PN junction diode*. Addison-Wesley Longman, Incorporated, 1983.

[3] E. F. Schubert, *Light-emitting diodes*. Cambridge; New York: Cambridge University Press, 2006.

[4] P. Bhattacharya, *Semiconductor Optoelectronic Devices*, 2 edition. Upper Saddle River, NJ: Prentice Hall, 1996.

[5] J.-J. Huang, H.-C. Kuo, and S.-C. Shen, *Nitride Semiconductor Light-Emitting Diodes (LEDs): Materials, Technologies and Applications*. Woodhead Publishing, 2014.

[6] J. Piprek, *Semiconductor Optoelectronic Devices: Introduction to Physics and Simulation*. Academic Press, 2003.

[7] Q. Dai *et al.*, "On the symmetry of efficiency-versus-carrier-concentration curves in GaInN/GaN light-emitting diodes and relation to droop-causing mechanisms," *Appl. Phys. Lett.*, vol. 98, no. 3, p. 033506, Jan. 2011, doi: 10.1063/1.3544584.

[8] J. Tsao, "Solid-State Lighting: Toward Smart and Ultra-Efficient Materials, Devices, Lamps and Systems," in *Photonics Volume 3: Photonics Technology and Instrumentation*, Wiley, 2013.

[9] S. Franssila, *Introduction to Microfabrication*, 2 edition. Chichester, West Sussex England: Wiley, 2010.

[10] K. B. Nam, J. Li, J. Y. Lin, and H. X. Jiang, “Optical properties of AlN and GaN in elevated temperatures,” *Appl. Phys. Lett.*, vol. 85, no. 16, p. 3489, Oct. 2004, doi: doi:10.1063/1.1806545.

[11] C. F. Li, Y. S. Huang, L. Malikova, and F. H. Pollak, “Temperature dependence of the energies and broadening parameters of the interband excitonic transitions in wurtzite GaN,” *Phys. Rev. B*, vol. 55, no. 15, pp. 9251–9254, Apr. 1997, doi: 10.1103/PhysRevB.55.9251.

[12] T. Westover, R. Jones, J. Y. Huang, G. Wang, E. Lai, and A. A. Talin, “Photoluminescence, Thermal Transport, and Breakdown in Joule-Heated GaN Nanowires,” *Nano Lett.*, vol. 9, no. 1, pp. 257–263, Jan. 2009, doi: 10.1021/nl802840w.

[13] Y. Arakawa, “Progress in GaN-based quantum dots for optoelectronics applications,” *IEEE J. Sel. Top. Quantum Electron.*, vol. 8, no. 4, pp. 823–832, Jul. 2002, doi: 10.1109/JSTQE.2002.801675.

[14] N. Izyumskaya, D. O. Demchenko, S. Das, Ü. Özgür, V. Avrutin, and H. Morkoç, “Recent Development of Boron Nitride towards Electronic Applications,” *Adv. Electron. Mater.*, vol. 3, no. 5, p. 1600485, May 2017, doi: 10.1002/aelm.201600485.

[15] F. Mahvash, E. Paradis, D. Drouin, T. Szkopek, and M. Siaj, “Space-Charge Limited Transport in Large-Area Monolayer Hexagonal Boron Nitride,” *Nano Lett.*, vol. 15, no. 4, pp. 2263–2268, Apr. 2015, doi: 10.1021/nl504197c.

[16] H. X. Jiang and J. Y. Lin, “Hexagonal boron nitride for deep ultraviolet photonic devices,” *Semicond. Sci. Technol.*, vol. 29, no. 8, p. 084003, 2014, doi: 10.1088/0268-1242/29/8/084003.

[17] H. X. Jiang and J. Y. Lin, “Review—Hexagonal Boron Nitride Epilayers: Growth, Optical Properties and Device Applications,” *ECS J. Solid State Sci. Technol.*, vol. 6, no. 2, pp. Q3012–Q3021, Jan. 2017, doi: 10.1149/2.0031702jss.

[18] B. He *et al.*, “p-type conduction in beryllium-implanted hexagonal boron nitride films,” *Appl. Phys. Lett.*, vol. 95, no. 25, p. 252106, Dec. 2009, doi: 10.1063/1.3276065.

[19] K. Watanabe, T. Taniguchi, and H. Kanda, “Direct-bandgap properties and evidence for ultraviolet lasing of hexagonal boron nitride single crystal,” *Nat. Mater.*, vol. 3, no. 6, pp. 404–409, Jun. 2004, doi: 10.1038/nmat1134.

[20] G. Cassabois, P. Valvin, and B. Gil, “Hexagonal boron nitride is an indirect bandgap semiconductor,” *Nat. Photonics*, vol. 10, no. 4, pp. 262–266, Apr. 2016, doi: 10.1038/nphoton.2015.277.

[21] J. Li, X. K. Cao, T. B. Hoffman, J. H. Edgar, J. Y. Lin, and H. X. Jiang, “Nature of exciton transitions in hexagonal boron nitride,” *Appl. Phys. Lett.*, vol. 108, no. 12, p. 122101, 2016.

[22] T. C. Doan, J. Li, J. Y. Lin, and H. X. Jiang, “Bandgap and exciton binding energies of hexagonal boron nitride probed by photocurrent excitation spectroscopy,” *Appl. Phys. Lett.*, vol. 109, no. 12, p. 122101, Sep. 2016, doi: 10.1063/1.4963128.

[23] C. Elias *et al.*, “Direct band-gap crossover in epitaxial monolayer boron nitride,” *Nat. Commun.*, vol. 10, no. 1, p. 2639, Jun. 2019, doi: 10.1038/s41467-019-10610-5.

[24] D. Wickramaratne, L. Weston, and C. G. Van de Walle, “Monolayer to Bulk Properties of Hexagonal Boron Nitride,” *J. Phys. Chem. C*, vol. 122, no. 44, pp. 25524–25529, Nov. 2018, doi: 10.1021/acs.jpcc.8b09087.

[25] C. Attaccalite, M. Bockstedte, A. Marini, A. Rubio, and L. Wirtz, “Coupling of excitons and defect states in boron-nitride nanostructures,” *Phys. Rev. B*, vol. 83, no. 14, p. 144115, Apr. 2011, doi: 10.1103/PhysRevB.83.144115.

[26] X. Z. Du, J. Li, J. Y. Lin, and H. X. Jiang, “The origins of near band-edge transitions in hexagonal boron nitride epilayers,” *Appl. Phys. Lett.*, vol. 108, no. 5, p. 052106, 2016.

[27] A. K. Geim and I. V. Grigorieva, “Van der Waals heterostructures,” *Nature*, vol. 499, no. 7459, pp. 419–425, Jul. 2013, doi: 10.1038/nature12385.

[28] C. R. Dean *et al.*, “Boron nitride substrates for high-quality graphene electronics,” *Nat. Nanotechnol.*, vol. 5, no. 10, pp. 722–726, Oct. 2010, doi: 10.1038/nnano.2010.172.

[29] Z. Zuo, Z. Xu, R. Zheng, A. Khanaki, J.-G. Zheng, and J. Liu, “In-situ epitaxial growth of graphene/h-BN van der Waals heterostructures by molecular beam epitaxy,” *Sci. Rep.*, vol. 5, p. 14760, Oct. 2015, doi: 10.1038/srep14760.

[30] Z. Xu, R. Zheng, A. Khanaki, Z. Zuo, and J. Liu, “Direct growth of graphene on in situ epitaxial hexagonal boron nitride flakes by plasma-assisted molecular beam epitaxy,” *Appl. Phys. Lett.*, vol. 107, no. 21, p. 213103, Nov. 2015, doi: 10.1063/1.4936378.

[31] V. K. Gupta, C. C. Wamsley, M. W. Koch, and G. W. Wicks, “Molecular beam epitaxy growth of boron-containing nitrides,” *J. Vac. Sci. Technol. B*, vol. 17, no. 3, pp. 1246–1248, May 1999, doi: 10.1116/1.590731.

[32] A. Ougazzaden *et al.*, “Bandgap bowing in BGaN thin films,” *Appl. Phys. Lett.*, vol. 93, no. 8, p. 083118, Aug. 2008, doi: 10.1063/1.2977588.

[33] T. T. Tran, K. Bray, M. J. Ford, M. Toth, and I. Aharonovich, “Quantum emission from hexagonal boron nitride monolayers,” *Nat. Nanotechnol.*, vol. 11, no. 1, pp. 37–41, Jan. 2016, doi: 10.1038/nnano.2015.242.

[34] Z. Lei, S. Xu, J. Wan, and P. Wu, “Facile preparation and multifunctional applications of boron nitride quantum dots,” *Nanoscale*, vol. 7, no. 45, pp. 18902–18907, 2015, doi: 10.1039/C5NR05960G.

[35] L. Lin, Y. Xu, S. Zhang, I. M. Ross, A. C. M. Ong, and D. A. Allwood, “Fabrication and Luminescence of Monolayered Boron Nitride Quantum Dots,” *Small*, vol. 10, no. 1, pp. 60–65, Jan. 2014, doi: 10.1002/smll.201301001.

[36] N. G. Chopra, R. J. Luyken, K. Cherrey, V. H. Crespi, and et al, “Boron nitride nanotubes,” *Sci. Wash.*, vol. 269, no. 5226, p. 966, Aug. 1995.

[37] D. Golberg, Y. Bando, C. C. Tang, and C. Y. Zhi, “Boron Nitride Nanotubes,” *Adv. Mater.*, vol. 19, no. 18, pp. 2413–2432, Sep. 2007, doi: 10.1002/adma.200700179.

[38] C. Zhi, Y. Bando, C. Tang, and D. Golberg, “Boron nitride nanotubes,” *Mater. Sci. Eng. R Rep.*, vol. 70, no. 3–6, pp. 92–111, Nov. 2010, doi: 10.1016/j.mser.2010.06.004.

[39] D. Stevenson, W. Rhines, and H. Maruska, “Gallium nitride metal-semiconductor junction light emitting diode,” US3819974A, Jun. 25, 1974.

[40] T. D. Moustakas, “Highly insulating monocrystalline gallium nitride thin films,” US5686738A, Nov. 11, 1997.

[41] “The 2014 Nobel Prize in Physics - Press Release.” http://www.nobelprize.org/nobel_prizes/physics/laureates/2014/press.html (accessed Nov. 17, 2014).

[42] Y. Taniyasu, M. Kasu, and T. Makimoto, “An aluminium nitride light-emitting diode with a wavelength of 210 nanometres,” *Nature*, vol. 441, no. 7091, pp. 325–328, May 2006, doi: 10.1038/nature04760.

[43] B. H. Le, S. Zhao, N. H. Tran, and Z. Mi, “Electrically injected near-infrared light emission from single InN nanowire p-i-n diode,” *Appl. Phys. Lett.*, vol. 105, no. 23, p. 231124, Dec. 2014, doi: 10.1063/1.4904271.

[44] S. Zhao *et al.*, “Aluminum nitride nanowire light emitting diodes: Breaking the fundamental bottleneck of deep ultraviolet light sources,” *Sci. Rep.*, vol. 5, no. 8332, Feb. 2015, doi: 10.1038/srep08332.

[45] E. Ertekin, P. A. Greaney, D. C. Chrzan, and T. D. Sands, “Equilibrium limits of coherency in strained nanowire heterostructures,” *J. Appl. Phys.*, vol. 97, no. 11, p. 114325, Jun. 2005, doi: 10.1063/1.1903106.

[46] R. Yan, D. Gargas, and P. Yang, “Nanowire photonics,” *Nat. Photonics*, vol. 3, no. 10, pp. 569–576, Oct. 2009, doi: 10.1038/nphoton.2009.184.

[47] C. Pfüller *et al.*, “Raman spectroscopy as a probe for the coupling of light into ensembles of sub-wavelength-sized nanowires,” *Appl. Phys. Lett.*, vol. 101, no. 8, p. 083104, Aug. 2012, doi: 10.1063/1.4747208.

[48] M.-L. Kuo, Y.-S. Kim, M.-L. Hsieh, and S.-Y. Lin, “Efficient and Directed Nano-LED Emission by a Complete Elimination of Transverse-Electric Guided Modes,” *Nano Lett.*, vol. 11, no. 2, pp. 476–481, 2010, doi: 10.1021/nl103243n.

[49] H. P. T. Nguyen *et al.*, “Breaking the Carrier Injection Bottleneck of Phosphor-Free Nanowire White Light-Emitting Diodes,” *Nano Lett.*, vol. 13, no. 11, pp. 5437–5442, Nov. 2013, doi: 10.1021/nl4030165.

[50] M. Kneissl and J. Rass, *III-Nitride Ultraviolet Emitters: Technology and Applications*. Springer, 2015.

[51] Z. Mi and C. Jagadish, Eds., *III-Nitride Semiconductor Optoelectronics*, 1 edition. Cambridge, MA San Diego, CA Oxford London: Academic Press, 2017.

[52] Q. Wang *et al.*, "Highly efficient, spectrally pure 340 nm ultraviolet emission from AlxGa1−xN nanowire based light emitting diodes," *Nanotechnology*, vol. 24, no. 34, p. 345201, Aug. 2013, doi: 10.1088/0957-4484/24/34/345201.

[53] A. Khan, K. Balakrishnan, and T. Katona, "Ultraviolet light-emitting diodes based on group three nitrides," *Nat. Photonics*, vol. 2, no. 2, pp. 77–84, Feb. 2008, doi: 10.1038/nphoton.2007.293.

[54] K. Ding, V. Avrutin, Ü. Özgür, and H. Morkoç, "Status of Growth of Group III-Nitride Heterostructures for Deep Ultraviolet Light-Emitting Diodes," *Crystals*, vol. 7, no. 10, p. 300, Oct. 2017, doi: 10.3390/cryst7100300.

[55] S. Zhang, D. A. Laleyan, Q. Wang, and Z. Mi, "Impact of nanowire geometry on the carrier transport in GaN/InGaN axial nanowire light-emitting diodes," *J. Eng.*, vol. 2015, no. 10, pp. 299–301, Sep. 2015, doi: 10.1049/joe.2014.0349.

[56] K. Pinardi, U. Jain, S. C. Jain, H. E. Maes, R. V. Overstraeten, and M. Willander, "Critical thickness and strain relaxation in lattice mismatched II–VI semiconductor layers," *J. Appl. Phys.*, vol. 83, no. 9, pp. 4724–4733, May 1998, doi: 10.1063/1.367261.

[57] L. Chang, S. K. Lai, F. R. Chen, and J. J. Kai, "Observations of Al segregation around dislocations in AlGaN," *Appl. Phys. Lett.*, vol. 79, no. 7, pp. 928–930, Aug. 2001, doi: 10.1063/1.1391409.

[58] D. Li, K. Jiang, X. Sun, and C. Guo, "AlGaN photonics: recent advances in materials and ultraviolet devices," *Adv. Opt. Photonics*, vol. 10, no. 1, pp. 43–110, Mar. 2018, doi: 10.1364/AOP.10.000043.

[59] H.-Y. Ryu, I.-G. Choi, H.-S. Choi, and J.-I. Shim, “Investigation of Light Extraction Efficiency in AlGaN Deep-Ultraviolet Light-Emitting Diodes,” *Appl. Phys. Express*, vol. 6, no. 6, p. 062101, May 2013, doi: 10.7567/APEX.6.062101.

[60] T. Kolbe *et al.*, “Optical polarization characteristics of ultraviolet (In)(Al)GaN multiple quantum well light emitting diodes,” *Appl. Phys. Lett.*, vol. 97, no. 17, p. 171105, Oct. 2010, doi: 10.1063/1.3506585.

[61] Y. Guo, J. Yan, Y. Zhang, J. Wang, and J. Li, “Enhancing the light extraction of AlGaN-based ultraviolet light-emitting diodes in the nanoscale,” *J. Nanophotonics*, vol. 12, no. 4, p. 043510, Jul. 2018, doi: 10.1117/1.JNP.12.043510.

[62] J. Zhang, H. Zhao, and N. Tansu, “Effect of crystal-field split-off hole and heavy-hole bands crossover on gain characteristics of high Al-content AlGaN quantum well lasers,” *Appl. Phys. Lett.*, vol. 97, no. 11, p. 111105, Sep. 2010, doi: 10.1063/1.3488825.

[63] K. B. Nam, J. Li, M. L. Nakarmi, J. Y. Lin, and H. X. Jiang, “Unique optical properties of AlGaN alloys and related ultraviolet emitters,” *Appl. Phys. Lett.*, vol. 84, no. 25, pp. 5264–5266, Jun. 2004, doi: 10.1063/1.1765208.

[64] J. Piprek and S. Li, “Electron leakage effects on GaN-based light-emitting diodes,” *Opt. Quantum Electron.*, vol. 42, no. 2, pp. 89–95, Jan. 2010, doi: 10.1007/s11082-011-9437-z.

[65] D. S. Meyaard *et al.*, “Identifying the cause of the efficiency droop in GaInN light-emitting diodes by correlating the onset of high injection with the onset of the efficiency droop,” *Appl. Phys. Lett.*, vol. 102, no. 25, p. 251114, Jun. 2013, doi: 10.1063/1.4811558.

[66] H. P. T. Nguyen *et al.*, “Controlling Electron Overflow in Phosphor-Free InGaN/GaN Nanowire White Light-Emitting Diodes,” *Nano Lett.*, vol. 12, no. 3, pp. 1317–1323, Mar. 2012, doi: 10.1021/nl203860b.

[67] D. S. Meyaard *et al.*, “Asymmetry of carrier transport leading to efficiency droop in GaInN based light-emitting diodes,” *Appl. Phys. Lett.*, vol. 99, no. 25, p. 251115, Dec. 2011, doi: 10.1063/1.3671395.

[68] G.-B. Lin, D. Meyaard, J. Cho, E. F. Schubert, H. Shim, and C. Sone, “Analytic model for the efficiency droop in semiconductors with asymmetric carrier-transport properties based on drift-induced reduction of injection efficiency,” *Appl. Phys. Lett.*, vol. 100, no. 16, p. 161106, Apr. 2012, doi: 10.1063/1.4704366.

[69] M. L. Nakarmi, N. Nepal, J. Y. Lin, and H. X. Jiang, “Photoluminescence studies of impurity transitions in Mg-doped AlGaN alloys,” *Appl. Phys. Lett.*, vol. 94, no. 9, p. 091903, Mar. 2009, doi: 10.1063/1.3094754.

[70] Q. Wang *et al.*, “Optical properties of strain-free AlN nanowires grown by molecular beam epitaxy on Si substrates,” *Appl. Phys. Lett.*, vol. 104, no. 22, p. 223107, Jun. 2014, doi: 10.1063/1.4881558.

[71] A. T. Connie *et al.*, “Optical and electrical properties of Mg-doped AlN nanowires grown by molecular beam epitaxy,” *Appl. Phys. Lett.*, vol. 106, no. 21, p. 213105, May 2015, doi: 10.1063/1.4921626.

[72] S. Zhao, M. Djavid, and Z. Mi, “Surface Emitting, High Efficiency Near-Vacuum Ultraviolet Light Source with Aluminum Nitride Nanowires Monolithically Grown on Silicon,” *Nano Lett.*, vol. 15, no. 10, pp. 7006–7009, Oct. 2015, doi: 10.1021/acs.nanolett.5b03040.

[73] N. H. Tran, B. H. Le, S. Zhao, and Z. Mi, “On the mechanism of highly efficient p-type conduction of Mg-doped ultra-wide-bandgap AlN nanostructures,” *Appl. Phys. Lett.*, vol. 110, no. 3, p. 032102, 2017.

[74] S. Zhao *et al.*, “Molecular beam epitaxy growth of Al-rich AlGaN nanowires for deep ultraviolet optoelectronics,” *APL Mater.*, vol. 4, no. 8, p. 086115, Aug. 2016, doi: 10.1063/1.4961680.

[75] S. M. Sadaf *et al.*, “An AlGaN Core–Shell Tunnel Junction Nanowire Light-Emitting Diode Operating in the Ultraviolet-C Band,” *Nano Lett.*, vol. 17, no. 2, pp. 1212–1218, Feb. 2017, doi: 10.1021/acs.nanolett.6b05002.

[76] K. H. Li, X. Liu, Q. Wang, S. Zhao, and Z. Mi, “Ultralow-threshold electrically injected AlGaN nanowire ultraviolet lasers on Si operating at low temperature,” *Nat. Nanotechnol.*, vol. 10, no. 2, pp. 140–144, Feb. 2015, doi: 10.1038/nnano.2014.308.

[77] S. Zhao, X. Liu, S. Y. Woo, J. Kang, G. A. Botton, and Z. Mi, “An electrically injected AlGaN nanowire laser operating in the ultraviolet-C band,” *Appl Phys Lett*, vol. 107, no. 4, p. 043101, Jul. 2015, doi: 10.1063/1.4927602.

[78] S. Zhao, X. Liu, Y. Wu, and Z. Mi, “An electrically pumped 239 nm AlGaN nanowire laser operating at room temperature,” *Appl. Phys. Lett.*, vol. 109, no. 19, p. 191106, Nov. 2016, doi: 10.1063/1.4967180.

[79] B. H. Le, S. Zhao, X. Liu, S. Y. Woo, G. A. Botton, and Z. Mi, “Controlled Coalescence of AlGaN Nanowire Arrays: An Architecture for Nearly Dislocation-Free Planar Ultraviolet Photonic Device Applications,” *Adv. Mater.*, vol. 28, no. 38, pp. 8446–8454, Oct. 2016, doi: 10.1002/adma.201602645.

[80] R. Schlesser, V. Noveski, and Z. Sitar, “Seeded growth process for preparing aluminum nitride single crystals,” US7678195B2, Mar. 16, 2010.

[81] R. Schlesser, R. Dalmau, and Z. Sitar, “Seeded growth of AlN bulk single crystals by sublimation,” *J. Cryst. Growth*, vol. 241, no. 4, pp. 416–420, Jun. 2002, doi: 10.1016/S0022-0248(02)01319-2.

[82] “HEXATECH, INC.” http://www.hexatechinc.com/ (accessed Mar. 10, 2020).

[83] R. Dalmau, B. Moody, J. Xie, R. Collazo, and Z. Sitar, “Characterization of dislocation arrays in AlN single crystals grown by PVT,” *Phys. Status Solidi A*, vol. 208, no. 7, pp. 1545–1547, 2011, doi: 10.1002/pssa.201000957.

[84] B. Neuschl *et al.*, “Optical identification of silicon as a shallow donor in MOVPE grown homoepitaxial AlN,” *Phys. Status Solidi B*, vol. 249, no. 3, pp. 511–515, 2012, doi: 10.1002/pssb.201100381.

[85] W.-H. Chen *et al.*, “The Physical Vapor Transport Method for Bulk AlN Crystal Growth,” *Molecules*, vol. 24, no. 8, p. 1562, Jan. 2019, doi: 10.3390/molecules24081562.

[86] Y. Kumagai *et al.*, “Preparation of a Freestanding AlN Substrate from a Thick AlN Layer Grown by Hydride Vapor Phase Epitaxy on a Bulk AlN Substrate Prepared by Physical Vapor Transport,” *Appl. Phys. Express*, vol. 5, no. 5, p. 055504, May 2012, doi: 10.1143/APEX.5.055504.

[87] M. Bockowski, M. Iwinska, M. Amilusik, M. Fijalkowski, B. Lucznik, and T. Sochacki, “Challenges and future perspectives in HVPE-GaN growth on ammonothermal GaN seeds,” *Semicond. Sci. Technol.*, vol. 31, no. 9, p. 093002, Aug. 2016, doi: 10.1088/0268-1242/31/9/093002.

[88] “AIXTRON Technologies: MOCVD :: AIXTRON.” https://www.aixtron.com/en/innovation/technologies/mocvd (accessed Mar. 10, 2020).

[89] M. Kneissl *et al.*, "Advances in group III-nitride-based deep UV light-emitting diode technology," *Semicond. Sci. Technol.*, vol. 26, no. 1, p. 014036, Dec. 2010, doi: 10.1088/0268-1242/26/1/014036.

[90] T. Takano, T. Mino, J. Sakai, N. Noguchi, K. Tsubaki, and H. Hirayama, "Deep-ultraviolet light-emitting diodes with external quantum efficiency higher than 20% at 275 nm achieved by improving light-extraction efficiency," *Appl. Phys. Express*, vol. 10, no. 3, p. 031002, Feb. 2017, doi: 10.7567/APEX.10.031002.

[91] H. Wang, Y. Zhao, Y. Xie, X. Ma, and X. Zhang, "Recent progress in synthesis of two-dimensional hexagonal boron nitride," *J. Semicond.*, vol. 38, no. 3, p. 031003, 2017, doi: 10.1088/1674-4926/38/3/031003.

[92] D. Y. Kim *et al.*, "Pressure-Dependent Growth of Wafer-Scale Few-layer h-BN by Metal–Organic Chemical Vapor Deposition," *Cryst. Growth Des.*, vol. 17, no. 5, pp. 2569–2575, May 2017, doi: 10.1021/acs.cgd.7b00107.

[93] J. M. Wofford *et al.*, "A hybrid MBE-based growth method for large-area synthesis of stacked hexagonal boron nitride/graphene heterostructures," *Sci. Rep.*, vol. 7, p. 43644, Feb. 2017, doi: 10.1038/srep43644.

[94] S. Majety *et al.*, "Epitaxial growth and demonstration of hexagonal BN/AlGaN p-n junctions for deep ultraviolet photonics," *Appl. Phys. Lett.*, vol. 100, no. 6, p. 061121, Feb. 2012, doi: 10.1063/1.3682523.

[95] H. Miyake, C.-H. Lin, K. Tokoro, and K. Hiramatsu, "Preparation of high-quality AlN on sapphire by high-temperature face-to-face annealing," *J. Cryst. Growth*, vol. 456, pp. 155–159, Dec. 2016, doi: 10.1016/j.jcrysgro.2016.08.028.

[96] S. Xiao, R. Suzuki, H. Miyake, S. Harada, and T. Ujihara, “Improvement mechanism of sputtered AlN films by high-temperature annealing,” *J. Cryst. Growth*, vol. 502, pp. 41–44, Nov. 2018, doi: 10.1016/j.jcrysgro.2018.09.002.

[97] J. D. Greenlee *et al.*, “Defect reduction in MBE-grown AlN by multicycle rapid thermal annealing,” *Electron. Mater. Lett.*, vol. 12, no. 1, pp. 133–138, Jan. 2016, doi: 10.1007/s13391-015-5270-z.

[98] D. A. Laleyan *et al.*, “Molecular beam epitaxy and characterization of Al0.6Ga0.4N epilayers,” *J. Cryst. Growth*, vol. 507, pp. 87–92, Feb. 2019, doi: 10.1016/j.jcrysgro.2018.10.048.

[99] D. A. Laleyan *et al.*, “AlN/h-BN Heterostructures for Mg Dopant-Free Deep Ultraviolet Photonics,” *Nano Lett.*, vol. 17, no. 6, pp. 3738–3743, Jun. 2017, doi: 10.1021/acs.nanolett.7b01068.

[100] D. A. Laleyan, K. Mengle, S. Zhao, Y. Wang, E. Kioupakis, and Z. Mi, “Effect of growth temperature on the structural and optical properties of few-layer hexagonal boron nitride by molecular beam epitaxy,” *Opt. Express*, vol. 26, no. 18, pp. 23031–23039, Sep. 2018, doi: 10.1364/OE.26.023031.

[101] W. P. McCray, “MBE deserves a place in the history books,” *Nat. Nanotechnol.*, vol. 2, no. 5, pp. 259–261, May 2007, doi: 10.1038/nnano.2007.121.

[102] J. Singh, S. Dudley, B. Davies, and K. K. Bajaj, “Role of kinetics and thermodynamics in alloy clustering and surface quality in InAlAs grown by molecular-beam epitaxy: Consequences for optical and transport properties,” *J. Appl. Phys.*, vol. 60, no. 9, pp. 3167–3171, Nov. 1986, doi: 10.1063/1.337730.

[103] R. Heckingbottom, C. J. Todd, and G. J. Davies, “The Interplay of Thermodynamics and Kinetics in Molecular Beam Epitaxy (MBE) of Doped Gallium Arsenide,” *J. Electrochem. Soc.*, vol. 127, no. 2, p. 444, Feb. 1980, doi: 10.1149/1.2129685.

[104] J. E. Ayers, *Heteroepitaxy of Semiconductors: Theory, Growth, and Characterization*. CRC Press, 2007.

[105] P. Bhattacharya and Z. Mi, “Quantum-Dot Optoelectronic Devices,” *Proc. IEEE*, vol. 95, no. 9, pp. 1723–1740, Sep. 2007, doi: 10.1109/JPROC.2007.900897.

[106] R. C. Cramer, J. English, B. Bonef, and J. S. Speck, “BBr3 as a boron source in plasma-assisted molecular beam epitaxy,” *J. Vac. Sci. Technol. A*, vol. 37, no. 6, p. 061502, Sep. 2019, doi: 10.1116/1.5117240.

[107] Y.-H. Liang, N. T. Nuhfer, and E. Towe, “Liquid-metal-enabled synthesis of aluminum-containing III-nitrides by plasma-assisted molecular beam epitaxy,” *J. Vac. Sci. Technol. B*, vol. 34, no. 2, p. 02L112, Mar. 2016, doi: 10.1116/1.4943016.

[108] T. S. Cheng *et al.*, “High-Temperature Molecular Beam Epitaxy of Hexagonal Boron Nitride with High Active Nitrogen Fluxes,” *Materials*, vol. 11, no. 7, p. 1119, Jul. 2018, doi: 10.3390/ma11071119.

[109] OliverToon, “RHEED,” *STAIB INSTRUMENTS*. https://www.staibinstruments.com/products/rheed/ (accessed Mar. 10, 2020).

[110] www.inficon.com, “Guardian™ EIES Controller - INFICON.” https://products.inficon.com/en-us/nav-products/product/detail/guardian/ (accessed Mar. 10, 2020).

[111] C. Lu, M. J. Lightner, and C. A. Gogol, "Rate controlling and composition analysis of alloy deposition processes by electron impact emission spectroscopy (EIES)," *J. Vac. Sci. Technol.*, vol. 14, no. 1, pp. 103–107, Jan. 1977, doi: 10.1116/1.569096.

[112] C. Lu, C. D. Blissett, and G. Diehl, "An electron impact emission spectroscopy flux sensor for monitoring deposition rate at high background gas pressure with improved accuracy," *J. Vac. Sci. Technol. A*, vol. 26, no. 4, pp. 956–960, Jul. 2008, doi: 10.1116/1.2830633.

[113] "Infrared Pyrometer Ircon Modline 4 | Fluke Process Instruments." https://www.flukeprocessinstruments.com/en-us/products/infrared-temperature-solutions/spot-pyrometers/modline-4 (accessed Mar. 10, 2020).

[114] "kSA BandiT - Wafer, Substrate, and Thin-Film Temperature Monitoring." https://www.k-space.com/products/bandit/ (accessed Mar. 10, 2020).

[115] "Residual Gas Analyzer." https://www.thinksrs.com/products/rga.html (accessed Mar. 10, 2020).

[116] "Atomic-Resolution Elemental Mapping by EELS and XEDS in Aberration Corrected STEM | Applications | JEOL Ltd." https://www.jeol.co.jp/en/applications/detail/790.html (accessed Mar. 10, 2020).

[117] "Tapping Mode," *Bruker.com*. https://www.bruker.com/products/surface-and-dimensional-analysis/atomic-force-microscopes/modes/modes/imaging-modes/tapping-mode.html (accessed Mar. 10, 2020).

[118] "Thin film analysis | Rigaku Global Website." https://www.rigaku.com/applications/thin-film-analysis (accessed Mar. 10, 2020).

[119] "What is Raman Spectroscopy?," *HORIBA*. https://www.horiba.com/en_en/raman-imaging-and-spectroscopy/, https://www.horiba.com/en_en/raman-imaging-and-spectroscopy/ (accessed Mar. 10, 2020).

[120] "Thermo Scientific XPS: What is XPS." https://xpssimplified.com/whatisxps.php (accessed Mar. 10, 2020).

[121] "Auger Electron Spectroscopy (AES) Surface Analysis Technique." https://www.phi.com/surface-analysis-techniques/aes.html (accessed Mar. 10, 2020).

[122] "Secondary Ion Mass Spectrometry (SIMS)," *EAG Laboratories*. https://www.eag.com/techniques/mass-spec/secondary-ion-mass-spectrometry-sims/ (accessed Mar. 10, 2020).

[123] "What is Photoluminescence spectroscopy?," *HORIBA*. https://www.horiba.com/en_en/products/by-technique/molecular-spectroscopy/photoluminescence-pl-electroluminescence-el/, https://www.horiba.com/en_en/products/by-technique/molecular-spectroscopy/photoluminescence-pl-electroluminescence-el/ (accessed Mar. 10, 2020).

[124] T. Lu *et al.*, "Temperature-dependent photoluminescence in light-emitting diodes," *Sci. Rep.*, vol. 4, no. 1, pp. 1–7, Aug. 2014, doi: 10.1038/srep06131.

[125] S. Fan, Z. Qin, C. He, X. Wang, B. Shen, and G. Zhang, "Strain effect on the optical polarization properties of c-plane $Al_{0.26}Ga_{0.74}N$/GaN superlattices," *Opt. Express*, vol. 22, no. 6, pp. 6322–6328, Mar. 2014, doi: 10.1364/OE.22.006322.

[126] M. Guttmann *et al.*, "Optical light polarization and light extraction efficiency of AlGaN-based LEDs emitting between 264 and 220 nm," *Jpn. J. Appl. Phys.*, vol. 58, no. SC, p. SCCB20, May 2019, doi: 10.7567/1347-4065/ab0d09.

[127] "What is Ellipsometry?," *J.A. Woollam*. https://www.jawoollam.com/resources/ellipsometry-tutorial/what-is-ellipsometry (accessed Mar. 10, 2020).

[128] O. Philips'Gloeilampenfabrieken, "A method of measuring specific resistivity and Hall effect of discs of arbitrary shape," *Philips Res Rep*, vol. 13, no. 1, pp. 1–9, 1958.

[129] S. M. Sze and K. K. Ng, *Physics of Semiconductor Devices*, 3 edition. Hoboken, N.J: Wiley-Interscience, 2006.

[130] Y. Muramoto, M. Kimura, and S. Nouda, "Development and future of ultraviolet light-emitting diodes: UV-LED will replace the UV lamp," *Semicond. Sci. Technol.*, vol. 29, no. 8, p. 084004, Jun. 2014, doi: 10.1088/0268-1242/29/8/084004.

[131] A. M. Armstrong *et al.*, "Visible-blind and solar-blind detection induced by defects in AlGaN high electron mobility transistors," *J. Appl. Phys.*, vol. 123, no. 11, p. 114502, Mar. 2018, doi: 10.1063/1.4997605.

[132] C. Bayram, J. L. Pau, R. McClintock, and M. Razeghi, "Performance enhancement of GaN ultraviolet avalanche photodiodes with p-type δ-doping," *Appl. Phys. Lett.*, vol. 92, no. 24, p. 241103, Jun. 2008, doi: 10.1063/1.2948857.

[133] A. Nishikawa, K. Kumakura, and T. Makimoto, "High Critical Electric Field Exceeding 8 MV/cm Measured Using an AlGaN p–i–n Vertical Conducting Diode on n-SiC Substrate," *Jpn. J. Appl. Phys.*, vol. 46, no. 4S, p. 2316, Apr. 2007, doi: 10.1143/JJAP.46.2316.

[134] Z. Lochner *et al.*, "Deep-ultraviolet lasing at 243 nm from photo-pumped AlGaN/AlN heterostructure on AlN substrate," *Appl. Phys. Lett.*, vol. 102, no. 10, p. 101110, 2013, doi: 10.1063/1.4795719.

[135] M. Lachab *et al.*, “Optically-pumped 285 nm edge stimulated emission from AlGaN-based LED structures grown by MOCVD on sapphire substrates,” *Jpn. J. Appl. Phys.*, vol. 53, no. 11, p. 112101, Oct. 2014, doi: 10.7567/JJAP.53.112101.

[136] J. Bai, T. Wang, P. Comming, P. J. Parbrook, J. P. R. David, and A. G. Cullis, “Optical properties of AlGaN∕GaN multiple quantum well structure by using a high-temperature AlN buffer on sapphire substrate,” *J. Appl. Phys.*, vol. 99, no. 2, p. 023513, Jan. 2006, doi: 10.1063/1.2161941.

[137] X. Xu *et al.*, “Wafer-level MOCVD growth of AlGaN/GaN-on-Si HEMT structures with ultra-high room temperature 2DEG mobility,” *AIP Adv.*, vol. 6, no. 11, p. 115016, Nov. 2016, doi: 10.1063/1.4967816.

[138] K. B. Nam, J. Li, M. L. Nakarmi, J. Y. Lin, and H. X. Jiang, “Achieving highly conductive AlGaN alloys with high Al contents,” *Appl. Phys. Lett.*, vol. 81, no. 6, pp. 1038–1040, Jul. 2002, doi: 10.1063/1.1492316.

[139] J. Li, K. B. Nam, J. Y. Lin, and H. X. Jiang, “Optical and electrical properties of Al-rich AlGaN alloys,” *Appl. Phys. Lett.*, vol. 79, no. 20, pp. 3245–3247, Nov. 2001, doi: 10.1063/1.1418255.

[140] G. S. Huang, H. H. Yao, H. C. Kuo, and S. C. Wang, “Effect of growth conditions on the Al composition and quality of AlGaN film,” *Mater. Sci. Eng. B*, vol. 136, no. 1, pp. 29–32, Jan. 2007, doi: 10.1016/j.mseb.2006.08.064.

[141] Y. Jianchang, W. Junxi, L. Naixin, L. Zhe, R. Jun, and L. Jinmin, “High quality AlGaN grown on a high temperature AIN template by MOCVD,” *J. Semicond.*, vol. 30, no. 10, p. 103001, 2009, doi: 10.1088/1674-4926/30/10/103001.

[142] M. Z. Peng *et al.*, “Effect of growth temperature of initial AlN buffer on the structural and optical properties of Al-rich AlGaN,” *J. Cryst. Growth*, vol. 307, no. 2, pp. 289–293, Sep. 2007, doi: 10.1016/j.jcrysgro.2007.07.013.

[143] T. A. Henry, A. Armstrong, A. A. Allerman, and M. H. Crawford, “The influence of Al composition on point defect incorporation in AlGaN,” *Appl. Phys. Lett.*, vol. 100, no. 4, p. 043509, Jan. 2012, doi: 10.1063/1.3679681.

[144] Z. Ren *et al.*, “Heteroepitaxy of AlGaN on bulk AlN substrates for deep ultraviolet light emitting diodes,” *Appl. Phys. Lett.*, vol. 91, no. 5, p. 051116, Jul. 2007, doi: 10.1063/1.2766841.

[145] Y. H. Liang and E. Towe, “Heavy Mg-doping of (Al,Ga)N films for potential applications in deep ultraviolet light-emitting structures,” *J. Appl. Phys.*, vol. 123, no. 9, p. 095303, Mar. 2018, doi: 10.1063/1.5009937.

[146] Y.-H. Liang and E. Towe, “Progress in efficient doping of high aluminum-containing group III-nitrides,” *Appl. Phys. Rev.*, vol. 5, no. 1, p. 011107, Mar. 2018, doi: 10.1063/1.5009349.

[147] D. V. Nechaev, P. N. Brunkov, S. I. Troshkov, V. N. Jmerik, and S. V. Ivanov, “Pulsed growth techniques in plasma-assisted molecular beam epitaxy of AlxGa1−xN layers with medium Al content (x=0.4–0.6),” *J. Cryst. Growth*, vol. 425, pp. 9–12, Sep. 2015, doi: 10.1016/j.jcrysgro.2015.03.055.

[148] F. Fedler *et al.*, “Strain, morphological, and growth-mode changes in AlGaN single layers at high AlN mole fraction,” *J. Cryst. Growth*, vol. 241, no. 4, pp. 535–542, Jun. 2002, doi: 10.1016/S0022-0248(02)01324-6.

[149] N. Antoine-Vincent *et al.*, “Determination of the refractive indices of AlN, GaN, and AlxGa1−xN grown on (111)Si substrates,” *J. Appl. Phys.*, vol. 93, no. 9, pp. 5222–5226, Apr. 2003, doi: 10.1063/1.1563293.

[150] H. Hirayama, N. Maeda, S. Fujikawa, S. Toyoda, and N. Kamata, “Recent progress and future prospects of AlGaN-based high-efficiency deep-ultraviolet light-emitting diodes,” *Jpn. J. Appl. Phys.*, vol. 53, no. 10, p. 100209, Oct. 2014, doi: 10.7567/JJAP.53.100209.

[151] H. Hirayama, T. Yatabe, N. Noguchi, T. Ohashi, and N. Kamata, “231-261 nm AlGaN deep-ultraviolet light-emitting diodes fabricated on AlN multilayer buffers grown by ammonia pulse-flow method on sapphire,” *Appl. Phys. Lett.*, vol. 91, Aug. 2007, doi: 10.1063/1.2770662.

[152] J. Enslin *et al.*, “Metamorphic Al0.5Ga0.5N:Si on AlN/sapphire for the growth of UVB LEDs,” *J. Cryst. Growth*, vol. 464, pp. 185–189, Apr. 2017, doi: 10.1016/j.jcrysgro.2017.01.052.

[153] I. Bryan *et al.*, “The role of surface kinetics on composition and quality of AlGaN,” *J. Cryst. Growth*, vol. 451, pp. 65–71, Oct. 2016, doi: 10.1016/j.jcrysgro.2016.06.055.

[154] M. Shirazi-HD *et al.*, “Kinetic instability of AlGaN alloys during MBE growth under metal-rich conditions on m-plane GaN miscut towards the -c axis,” *J. Appl. Phys.*, vol. 123, no. 16, p. 161581, Jan. 2018, doi: 10.1063/1.5011413.

[155] Y.-S. Liu *et al.*, “Optically pumped AlGaN quantum-well lasers at sub-250 nm grown by MOCVD on AlN substrates,” *Phys. Status Solidi C*, vol. 11, no. 2, pp. 258–260, Feb. 2014, doi: 10.1002/pssc.201300213.

[156] G. Parish, S. Keller, S. P. Denbaars, and U. K. Mishra, “SIMS Investigations into the Effect of Growth Conditions on Residual Impurity and Silicon Incorporation in GaN and AlxGa1−xN,” *J Electron Mater*, vol. 29, no. 1, pp. 15–20, Jan. 2000, doi: 10.1007/s11664-000-0087-3.

[157] E. Iliopoulos and T. D. Moustakas, “Growth kinetics of AlGaN films by plasma-assisted molecular-beam epitaxy,” *Appl. Phys. Lett.*, vol. 81, no. 2, pp. 295–297, Jun. 2002, doi: 10.1063/1.1492853.

[158] S. V. Novikov, C. R. Staddon, J. Whale, A. J. Kent, and C. T. Foxon, “Growth of free-standing wurtzite AlGaN by MBE using a highly efficient RF plasma source,” *J. Vac. Sci. Technol. B*, vol. 34, no. 2, p. 02L102, Jan. 2016, doi: 10.1116/1.4940155.

[159] Y. Liao, C. Thomidis, C. Kao, and T. D. Moustakas, “AlGaN based deep ultraviolet light emitting diodes with high internal quantum efficiency grown by molecular beam epitaxy,” *Appl. Phys. Lett.*, vol. 98, no. 8, p. 081110, 2011.

[160] H. Okumura *et al.*, “Analysis of MBE growth mode for GaN epilayers by RHEED,” *J. Cryst. Growth*, vol. 189–190, pp. 364–369, Jun. 1998, doi: 10.1016/S0022-0248(98)00313-3.

[161] D. Brunner *et al.*, “Optical constants of epitaxial AlGaN films and their temperature dependence,” *J. Appl. Phys.*, vol. 82, no. 10, pp. 5090–5096, Nov. 1997, doi: 10.1063/1.366309.

[162] U. Tisch, B. Meyler, O. Katz, E. Finkman, and J. Salzman, “Dependence of the refractive index of AlxGa1−xN on temperature and composition at elevated temperatures,” *J. Appl. Phys.*, vol. 89, no. 5, pp. 2676–2685, Feb. 2001, doi: 10.1063/1.1341212.

[163] I. Bryan *et al.*, “Homoepitaxial AlN thin films deposited on m-plane (11¯00) AlN substrates by metalorganic chemical vapor deposition,” *J. Appl. Phys.*, vol. 116, no. 13, p. 133517, Oct. 2014, doi: 10.1063/1.4897233.

[164] A. Wise, R. Nandivada, B. Strawbridge, R. Carpenter, N. Newman, and S. Mahajan, “[0001] composition modulations in Al0.4Ga0.6N layers grown by molecular beam epitaxy,” *Appl. Phys. Lett.*, vol. 92, no. 26, p. 261914, Jun. 2008, doi: 10.1063/1.2953451.

[165] S. Keller *et al.*, “Recent progress in metal-organic chemical vapor deposition of N-polar group-III nitrides,” *Semicond. Sci. Technol.*, vol. 29, no. 11, p. 113001, 2014, doi: 10.1088/0268-1242/29/11/113001.

[166] J. Liu *et al.*, “Unintentionally doped high resistivity GaN layers with an InGaN interlayer grown by MOCVD,” *RSC Adv.*, vol. 6, no. 65, pp. 60068–60073, 2016, doi: 10.1039/C6RA10696J.

[167] Z. Mi, J. Yang, P. Bhattacharya, G. Qin, and Z. Ma, “High-Performance Quantum Dot Lasers and Integrated Optoelectronics on Si,” *Proc. IEEE*, vol. 97, no. 7, pp. 1239–1249, Jul. 2009, doi: 10.1109/JPROC.2009.2014780.

[168] O. Klein, J. Biskupek, K. Forghani, F. Scholz, and U. Kaiser, “TEM investigations on growth interrupted samples for the correlation of the dislocation propagation and growth mode variations in AlGaN deposited on SiNx interlayers,” *J. Cryst. Growth*, vol. 324, no. 1, pp. 63–72, Jun. 2011, doi: 10.1016/j.jcrysgro.2011.03.050.

[169] H. Gong, G. Pan, C. Zou, Y. Zhou, and L. Xu, “Investigation on the variation of the step-terrace structure on the surface of polished GaN wafer,” *Surf. Interfaces*, vol. 6, pp. 197–201, Mar. 2017, doi: 10.1016/j.surfin.2016.10.010.

[170] S. Özen, V. Şenay, S. Pat, and Ş. Korkmaz, “The influence of voltage applied between the electrodes on optical and morphological properties of the InGaN thin films grown by thermionic vacuum arc,” *Scanning*, Sep. 2015, doi: 10.1002/sca.21237.

[171] G. Webb-Wood, Ü. Özgür, H. O. Everitt, F. Yun, and H. Morkoç, “Measurement of AlxGa1-xN Refractive Indices,” *Phys. Status Solidi A*, vol. 188, no. 2, pp. 793–797, Dec. 2001, doi: 10.1002/1521-396X(200112)188:2<793::AID-PSSA793>3.0.CO;2-S.

[172] N. A. Sanford *et al.*, "Refractive index study of AlxGa1−xN films grown on sapphire substrates," *J. Appl. Phys.*, vol. 94, no. 5, pp. 2980–2991, Aug. 2003, doi: 10.1063/1.1598276.

[173] H. Sun *et al.*, "Development of AlGaN-based graded-index-separate-confinement-heterostructure deep UV emitters by molecular beam epitaxy," *J. Vac. Sci. Technol. B*, vol. 31, no. 3, p. 03C117, Mar. 2013, doi: 10.1116/1.4796107.

[174] Z. Bryan, I. Bryan, J. Xie, S. Mita, Z. Sitar, and R. Collazo, "High internal quantum efficiency in AlGaN multiple quantum wells grown on bulk AlN substrates," *Appl. Phys. Lett.*, vol. 106, no. 14, p. 142107, Apr. 2015, doi: 10.1063/1.4917540.

[175] H. Wang *et al.*, "Influence of excitation power and temperature on photoluminescence in InGaN/GaN multiple quantum wells," *Opt. Express*, vol. 20, no. 4, pp. 3932–3940, Feb. 2012, doi: 10.1364/OE.20.003932.

[176] T. Onuma *et al.*, "Radiative and nonradiative processes in strain-free AlxGa1−xN films studied by time-resolved photoluminescence and positron annihilation techniques," *J. Appl. Phys.*, vol. 95, no. 5, pp. 2495–2504, Feb. 2004, doi: 10.1063/1.1644041.

[177] A. H. Park *et al.*, "Efficient stress-relaxation in InGaN/GaN light-emitting diodes using carbon nanotubes," *Nanoscale*, vol. 7, no. 37, pp. 15099–15105, Sep. 2015, doi: 10.1039/C5NR04239A.

[178] A. Laubsch *et al.*, "Measurement of the internal quantum efficiency of InGaN quantum wells," in *Light-Emitting Diodes: Research, Manufacturing, and Applications XI*, Feb. 2007, vol. 6486, p. 64860J, doi: 10.1117/12.700829.

[179] T.-J. Lu *et al.*, "Aluminum nitride integrated photonics platform for the ultraviolet to visible spectrum," *Opt. Express*, vol. 26, no. 9, pp. 11147–11160, Apr. 2018, doi: 10.1364/OE.26.011147.

[180] C. Xiong, W. H. P. Pernice, X. Sun, C. Schuck, K. Y. Fong, and H. X. Tang, “Aluminum nitride as a new material for chip-scale optomechanics and nonlinear optics,” *New J. Phys.*, vol. 14, no. 9, p. 095014, Sep. 2012, doi: 10.1088/1367-2630/14/9/095014.

[181] K. X. Chen *et al.*, “Effect of dislocations on electrical and optical properties of n-type Al0.34Ga0.66N,” *Appl. Phys. Lett.*, vol. 93, no. 19, p. 192108, Nov. 2008, doi: 10.1063/1.3021076.

[182] H. Sun *et al.*, “Influence of TMAl preflow on AlN epitaxy on sapphire,” *Appl. Phys. Lett.*, vol. 110, no. 19, p. 192106, May 2017, doi: 10.1063/1.4983388.

[183] M. Lamprecht, C. Grund, S. Bauer, R. Collazo, Z. Sitar, and K. Thonke, “Slow decay of a defect-related emission band at 2.05 eV in AlN: Signatures of oxygen-related DX states,” *Phys. Status Solidi B*, vol. 254, no. 5, p. 1600338, 2017, doi: 10.1002/pssb.201600338.

[184] X.-H. Li *et al.*, “Growth of high-quality AlN layers on sapphire substrates at relatively low temperatures by metalorganic chemical vapor deposition,” *Phys. Status Solidi B*, vol. 252, no. 5, pp. 1089–1095, 2015, doi: 10.1002/pssb.201451571.

[185] X. Zhang *et al.*, “Epitaxial growth of AlN films on sapphire via a multilayer structure adopting a low- and high-temperature alternation technique,” *CrystEngComm*, vol. 17, no. 39, pp. 7496–7499, Sep. 2015, doi: 10.1039/C5CE01159K.

[186] G. S. Lee *et al.*, “Growth of AlN layer on patterned sapphire substrate by hydride vapor phase epitaxy,” *Jpn. J. Appl. Phys.*, vol. 55, no. 5S, p. 05FC02, Apr. 2016, doi: 10.7567/JJAP.55.05FC02.

[187] L. Zhang *et al.*, “High-quality AlN epitaxy on nano-patterned sapphire substrates prepared by nano-imprint lithography,” *Sci. Rep.*, vol. 6, p. 35934, Nov. 2016, doi: 10.1038/srep35934.

[188] V. Kueller *et al.*, “Growth of AlGaN and AlN on patterned AlN/sapphire templates,” *J. Cryst. Growth*, vol. 315, no. 1, pp. 200–203, Jan. 2011, doi: 10.1016/j.jcrysgro.2010.06.040.

[189] S. Hagedorn, A. Knauer, F. Brunner, A. Mogilatenko, U. Zeimer, and M. Weyers, “High-quality AlN grown on a thermally decomposed sapphire surface,” *J. Cryst. Growth*, vol. 479, pp. 16–21, Dec. 2017, doi: 10.1016/j.jcrysgro.2017.09.019.

[190] C.-P. Huang, K. Gupta, C.-H. Wang, C.-P. Liu, and K.-Y. Lai, “High-quality AlN grown with a single substrate temperature below 1200 °C,” *Sci. Rep.*, vol. 7, no. 1, pp. 1–6, Aug. 2017, doi: 10.1038/s41598-017-07616-8.

[191] H. Miyake *et al.*, “Annealing of an AlN buffer layer in N2–CO for growth of a high-quality AlN film on sapphire,” *Appl. Phys. Express*, vol. 9, no. 2, p. 025501, Jan. 2016, doi: 10.7567/APEX.9.025501.

[192] F. Ren, Z.-B. Hao, J.-N. Hu, C. Zhang, and Y. Luo, “Effects of AlN nucleation layer thickness on crystal quality of AlN grown by plasma-assisted molecular beam epitaxy,” *Chin. Phys. B*, vol. 19, no. 11, p. 116801, Nov. 2010, doi: 10.1088/1674-1056/19/11/116801.

[193] D. D. Le, D. Y. Kim, and S.-K. Hong, “Effect of First-Stage Growth Manipulation and Polarity of SiC Substrates on AlN Epilayers Grown Using Plasma-Assisted Molecular Beam Epitaxy,” *Korean J. Mater. Res.*, vol. 24, no. 5, pp. 266–270, 2014, doi: 10.3740/MRSK.2014.24.5.266.

[194] A. Pandey *et al.*, “Enhanced doping efficiency of ultrawide band gap semiconductors by metal-semiconductor junction assisted epitaxy,” *Phys. Rev. Mater.*, vol. 3, no. 5, p. 053401, May 2019, doi: 10.1103/PhysRevMaterials.3.053401.

[195] Z. Y. Fan, G. Rong, N. Newman, and D. J. Smith, "Defect annihilation in AlN thin films by ultrahigh temperature processing," *Appl. Phys. Lett.*, vol. 76, no. 14, pp. 1839–1841, Mar. 2000, doi: 10.1063/1.126185.

[196] G. Ferro, H. Okumura, T. Ide, and S. Yoshida, "RHEED monitoring of AlN epitaxial growth by plasma-assisted molecular beam epitaxy," *J. Cryst. Growth*, vol. 210, no. 4, pp. 429–434, Mar. 2000, doi: 10.1016/S0022-0248(99)00891-X.

[197] R. Page, J. Casamento, Y. Cho, S. Rouvimov, H. G. Xing, and D. Jena, "Rotationally aligned hexagonal boron nitride on sapphire by high-temperature molecular beam epitaxy," *Phys. Rev. Mater.*, vol. 3, no. 6, p. 064001, Jun. 2019, doi: 10.1103/PhysRevMaterials.3.064001.

[198] M. Moseley, D. Billingsley, W. Henderson, E. Trybus, and W. A. Doolittle, "Transient atomic behavior and surface kinetics of GaN," *J. Appl. Phys.*, vol. 106, no. 1, p. 014905, Jul. 2009, doi: 10.1063/1.3148275.

[199] V. M. Kaganer, O. Brandt, A. Trampert, and K. H. Ploog, "X-ray diffraction peak profiles from threading dislocations in GaN epitaxial films," *Phys. Rev. B*, vol. 72, no. 4, p. 045423, Jul. 2005, doi: 10.1103/PhysRevB.72.045423.

[200] M. J. Manfra, N. G. Weimann, J. W. P. Hsu, L. N. Pfeiffer, K. W. West, and S. N. G. Chu, "Dislocation and morphology control during molecular-beam epitaxy of AlGaN/GaN heterostructures directly on sapphire substrates," *Appl. Phys. Lett.*, vol. 81, no. 8, pp. 1456–1458, Aug. 2002, doi: 10.1063/1.1498867.

[201] P. L. Galindo *et al.*, "The Peak Pairs algorithm for strain mapping from HRTEM images," *Ultramicroscopy*, vol. 107, no. 12, pp. 1186–1193, Nov. 2007, doi: 10.1016/j.ultramic.2007.01.019.

[202] S. C. Jain, M. Willander, J. Narayan, and R. V. Overstraeten, “III–nitrides: Growth, characterization, and properties,” *J. Appl. Phys.*, vol. 87, no. 3, p. 965, Feb. 2000, doi: doi:10.1063/1.371971.

[203] T. S. Argunova *et al.*, “Distribution of Dislocations near the Interface in AlN Crystals Grown on Evaporated SiC Substrates,” *Crystals*, vol. 7, no. 6, p. 163, Jun. 2017, doi: 10.3390/cryst7060163.

[204] H. M. Foronda *et al.*, “Low threading dislocation density aluminum nitride on silicon carbide through the use of reduced temperature interlayers,” *J. Cryst. Growth*, vol. 483, pp. 134–139, Feb. 2018, doi: 10.1016/j.jcrysgro.2017.11.027.

[205] B. N. Pantha *et al.*, “Correlation between optoelectronic and structural properties and epilayer thickness of AlN,” *Appl. Phys. Lett.*, vol. 90, no. 24, p. 241101, Jun. 2007, doi: 10.1063/1.2747662.

[206] L. Zhang *et al.*, “High-quality AlN epitaxy on sapphire substrates with sputtered buffer layers,” *Superlattices Microstruct.*, vol. 105, pp. 34–38, May 2017, doi: 10.1016/j.spmi.2017.03.013.

[207] M. X. Wang *et al.*, “High-temperature annealing induced evolution of strain in AlN epitaxial films grown on sapphire substrates,” *Appl. Phys. Lett.*, vol. 114, no. 11, p. 112105, Mar. 2019, doi: 10.1063/1.5087547.

[208] T. Shibata *et al.*, “Characterization of high-quality epitaxial AlN films grown by MOVPE,” *MRS Online Proc. Libr. Arch.*, vol. 693, ed 2001, doi: 10.1557/PROC-693-I9.3.1.

[209] S. Kitagawa, H. Miyake, and K. Hiramatsu, “High-quality AlN growth on 6H-SiC substrate using three dimensional nucleation by low-pressure hydride vapor phase epitaxy,” *Jpn. J. Appl. Phys.*, vol. 53, no. 5S1, p. 05FL03, Mar. 2014, doi: 10.7567/JJAP.53.05FL03.

[210] Z. Chen, H. Zhi-Biao, R. Fan, H. Jian-Nan, and L. Yi, "Improvement of AlN Film Quality by Controlling the Coalescence of Nucleation Islands in Plasma-Assisted Molecular Beam Epitaxy," *Chin. Phys. Lett.*, vol. 27, no. 5, p. 058101, May 2010, doi: 10.1088/0256-307X/27/5/058101.

[211] W. Luo *et al.*, "Influence of the nucleation layer morphology on the structural property of AlN films grown on c-plane sapphire by MOCVD," *J. Alloys Compd.*, vol. 697, pp. 262–267, Mar. 2017, doi: 10.1016/j.jallcom.2016.12.126.

[212] P. Lu *et al.*, "Seeded growth of AlN on SiC substrates and defect characterization," *J. Cryst. Growth*, vol. 310, no. 10, pp. 2464–2470, May 2008, doi: 10.1016/j.jcrysgro.2008.01.010.

[213] N. Matsunami, H. Kakiuchida, M. Sataka, and S. Okayasu, "XRD Characterization of AlN Thin Films Prepared by Reactive RF-Sputter Deposition," *Adv. Mater. Phys. Chem.*, vol. 3, no. 1, pp. 101–107, Apr. 2013, doi: 10.4236/ampc.2013.31A012.

[214] N. Onojima, J. Suda, T. Kimoto, and H. Matsunami, "4H-polytype AlN grown on 4H-SiC($11\bar{2}0$) substrate by polytype replication," *Appl. Phys. Lett.*, vol. 83, no. 25, pp. 5208–5210, Dec. 2003, doi: 10.1063/1.1636533.

[215] N. Faleev, H. Lu, and W. J. Schaff, "Low density of threading dislocations in AlN grown on sapphire," *J. Appl. Phys.*, vol. 101, no. 9, p. 093516, May 2007, doi: 10.1063/1.2728755.

[216] S. Yoshida, S. Misawa, and A. Itoh, "Epitaxial growth of aluminum nitride films on sapphire by reactive evaporation," *Appl. Phys. Lett.*, vol. 26, no. 8, pp. 461–462, Apr. 1975, doi: 10.1063/1.88210.

[217] R. D. Vispute, H. Wu, and J. Narayan, "High quality epitaxial aluminum nitride layers on sapphire by pulsed laser deposition," *Appl. Phys. Lett.*, vol. 67, no. 11, pp. 1549–1551, Sep. 1995, doi: 10.1063/1.114489.

[218] Z. Chen *et al.*, “High quality AlN grown on SiC by metal organic chemical vapor deposition,” *Appl. Phys. Lett.*, vol. 93, no. 19, p. 191906, Nov. 2008, doi: 10.1063/1.2988323.

[219] J. Lemettinen, H. Okumura, I. Kim, C. Kauppinen, T. Palacios, and S. Suihkonen, “MOVPE growth of N-polar AlN on 4H-SiC: Effect of substrate miscut on layer quality,” *J. Cryst. Growth*, vol. 487, pp. 12–16, Apr. 2018, doi: 10.1016/j.jcrysgro.2018.02.013.

[220] J. Lemettinen *et al.*, “MOVPE growth of nitrogen- and aluminum-polar AlN on 4H-SiC,” *J. Cryst. Growth*, vol. 487, pp. 50–56, Apr. 2018, doi: 10.1016/j.jcrysgro.2018.02.020.

[221] M. X. Wang *et al.*, “Crystal quality evolution of AlN films via high-temperature annealing under ambient N2 conditions,” *CrystEngComm*, vol. 20, no. 41, pp. 6613–6617, Oct. 2018, doi: 10.1039/C8CE00967H.

[222] M. Nemoz, R. Dagher, S. Matta, A. Michon, P. Vennéguès, and J. Brault, “Dislocation densities reduction in MBE-grown AlN thin films by high-temperature annealing,” *J. Cryst. Growth*, vol. 461, pp. 10–15, Mar. 2017, doi: 10.1016/j.jcrysgro.2016.12.089.

[223] X.-H. Li *et al.*, “Temperature dependence of the crystalline quality of AlN layer grown on sapphire substrates by metalorganic chemical vapor deposition,” *J. Cryst. Growth*, vol. 414, pp. 76–80, Mar. 2015, doi: 10.1016/j.jcrysgro.2014.10.007.

[224] S. R. Lee *et al.*, “Effect of threading dislocations on the Bragg peakwidths of GaN, AlGaN, and AlN heterolayers,” *Appl. Phys. Lett.*, vol. 86, no. 24, p. 241904, Jun. 2005, doi: 10.1063/1.1947367.

[225] B. Heying *et al.*, “Role of threading dislocation structure on the x-ray diffraction peak widths in epitaxial GaN films,” *Appl. Phys. Lett.*, vol. 68, no. 5, pp. 643–645, Jan. 1996, doi: 10.1063/1.116495.

[226] Y. Taniyasu and M. Kasu, “Origin of exciton emissions from an AlN p-n junction light-emitting diode,” *Appl. Phys. Lett.*, vol. 98, no. 13, p. 131910, Mar. 2011, doi: 10.1063/1.3574025.

[227] S. Tojo *et al.*, “Influence of high-temperature processing on the surface properties of bulk AlN substrates,” *J. Cryst. Growth*, vol. 446, pp. 33–38, Jul. 2016, doi: 10.1016/j.jcrysgro.2016.04.030.

[228] C. Heinlein, J. Grepstad, H. Riechert, and R. Averbeck, “Plasma preconditioning of sapphire substrate for GaN epitaxy,” *Mater. Sci. Eng. B*, vol. 43, no. 1, pp. 253–257, Jan. 1997, doi: 10.1016/S0921-5107(96)01878-8.

[229] J. Wang *et al.*, “High quality AlN epilayers grown on nitrided sapphire by metal organic chemical vapor deposition,” *Sci. Rep.*, vol. 7, no. 1, pp. 1–7, Feb. 2017, doi: 10.1038/srep42747.

[230] S. Nakamura, “Current Status of GaN-Based Solid-State Lighting,” *MRS Bull.*, vol. 34, no. 2, pp. 101–107, Feb. 2009, doi: 10.1557/mrs2009.28.

[231] T. Kinoshita *et al.*, “Deep-Ultraviolet Light-Emitting Diodes Fabricated on AlN Substrates Prepared by Hydride Vapor Phase Epitaxy,” *Appl. Phys. Express*, vol. 5, no. 12, p. 122101, Nov. 2012, doi: 10.1143/APEX.5.122101.

[232] Y. Aoki, M. Kuwabara, Y. Yamashita, Y. Takagi, A. Sugiyama, and H. Yoshida, “A 350-nm-band GaN/AlGaN multiple-quantum-well laser diode on bulk GaN,” *Appl. Phys. Lett.*, vol. 107, p. 151103, Oct. 2015, doi: 10.1063/1.4933257.

[233] S. Xu *et al.*, “Ordered Nanowire Array Blue/Near-UV Light Emitting Diodes,” *Adv. Mater.*, vol. 22, no. 42, pp. 4749–4753, Nov. 2010, doi: 10.1002/adma.201002134.

[234] K. B. Nam, M. L. Nakarmi, J. Li, J. Y. Lin, and H. X. Jiang, "Mg acceptor level in AlN probed by deep ultraviolet photoluminescence," *Appl. Phys. Lett.*, vol. 83, no. 5, pp. 878–880, Aug. 2003, doi: 10.1063/1.1594833.

[235] Y.-N. Xu and W. Y. Ching, "Calculation of ground-state and optical properties of boron nitrides in the hexagonal, cubic, and wurtzite structures," *Phys. Rev. B*, vol. 44, no. 15, pp. 7787–7798, Oct. 1991, doi: 10.1103/PhysRevB.44.7787.

[236] K. Watanabe, T. Taniguchi, T. Niiyama, K. Miya, and M. Taniguchi, "Far-ultraviolet plane-emission handheld device based on hexagonal boron nitride," *Nat. Photonics*, vol. 3, no. 10, pp. 591–594, Oct. 2009, doi: 10.1038/nphoton.2009.167.

[237] T. Ayari *et al.*, "Wafer-scale controlled exfoliation of metal organic vapor phase epitaxy grown InGaN/GaN multi quantum well structures using low-tack two-dimensional layered h-BN," *Appl. Phys. Lett.*, vol. 108, no. 17, p. 171106, Apr. 2016, doi: 10.1063/1.4948260.

[238] R. Dahal *et al.*, "Epitaxially grown semiconducting hexagonal boron nitride as a deep ultraviolet photonic material," *Appl. Phys. Lett.*, vol. 98, no. 21, p. 211110, May 2011, doi: 10.1063/1.3593958.

[239] W. Orellana and H. Chacham, "Stability of native defects in hexagonal and cubic boron nitride," *Phys. Rev. B*, vol. 63, p. 125205, Mar. 2001, doi: 10.1103/PhysRevB.63.125205.

[240] M. Lu, A. Bousetta, A. Bensaoula, K. Waters, and J. A. Schultz, "Electrical properties of boron nitride thin films grown by neutralized nitrogen ion assisted vapor deposition," *Appl. Phys. Lett.*, vol. 68, no. 5, pp. 622–624, Jan. 1996, doi: 10.1063/1.116488.

[241] V. Wang, R.-J. Liu, H.-P. He, C.-M. Yang, and L. Ma, "Hybrid functional with semi-empirical van der Waals study of native defects in hexagonal BN," *Solid State Commun.*, vol. 177, pp. 74–79, Jan. 2014, doi: 10.1016/j.ssc.2013.09.031.

[242] M. L. Nakarmi, N. Nepal, C. Ugolini, T. M. Altahtamouni, J. Y. Lin, and H. X. Jiang, "Correlation between optical and electrical properties of Mg-doped AlN epilayers," *Appl. Phys. Lett.*, vol. 89, no. 15, p. 152120, 2006.

[243] M. Bosman and V. J. Keast, "Optimizing EELS acquisition," *Ultramicroscopy*, vol. 108, no. 9, pp. 837–846, Aug. 2008, doi: 10.1016/j.ultramic.2008.02.003.

[244] O. Stephan *et al.*, "Doping Graphitic and Carbon Nanotube Structures with Boron and Nitrogen," *Science*, vol. 266, no. 5191, pp. 1683–1685, Dec. 1994, doi: 10.1126/science.266.5191.1683.

[245] M. Jaouen, G. Hug, V. Gonnet, G. Demazeau, and G. Tourillon, "An EELS and XAS Study of Cubic Boron Nitride Synthesized under High Pressure - High Temperature Conditions," *Microsc. Microanal. Microstruct.*, vol. 6, no. 1, pp. 127–139, 1995, doi: 10.1051/mmm:1995113.

[246] A. Bhattacharyya, T. D. Moustakas, L. Zhou, D. J. Smith, and W. Hug, "Deep ultraviolet emitting AlGaN quantum wells with high internal quantum efficiency," *Appl. Phys. Lett.*, vol. 94, no. 18, p. 181907, 2009.

[247] X. Zeng, F. Wang, X. Sun, and J. Li, "Recycling Indium from Scraped Glass of Liquid Crystal Display: Process Optimizing and Mechanism Exploring," *ACS Sustain. Chem. Eng.*, vol. 3, no. 7, pp. 1306–1312, Jul. 2015, doi: 10.1021/acssuschemeng.5b00020.

[248] P. Tao, A. Viswanath, L. S. Schadler, B. C. Benicewicz, and R. W. Siegel, "Preparation and Optical Properties of Indium Tin Oxide/Epoxy Nanocomposites with Polyglycidyl Methacrylate Grafted Nanoparticles," *ACS Appl. Mater. Interfaces*, vol. 3, no. 9, pp. 3638–3645, Sep. 2011, doi: 10.1021/am200841n.

[249] L. Kőrösi *et al.*, “Highly transparent ITO thin films on photosensitive glass: sol–gel synthesis, structure, morphology and optical properties,” *Appl. Phys. A*, vol. 107, no. 2, pp. 385–392, May 2012, doi: 10.1007/s00339-012-6765-1.

[250] M. Thirumoorthi and J. Thomas Joseph Prakash, “Structure, optical and electrical properties of indium tin oxide ultra thin films prepared by jet nebulizer spray pyrolysis technique,” *J. Asian Ceram. Soc.*, vol. 4, no. 1, pp. 124–132, Mar. 2016, doi: 10.1016/j.jascer.2016.01.001.

[251] A. Pakdel, Y. Bando, and D. Golberg, “Nano boron nitride flatland,” *Chem. Soc. Rev.*, vol. 43, no. 3, pp. 934–959, 2014, doi: 10.1039/C3CS60260E.

[252] S. Sonde *et al.*, “Ultrathin, wafer-scale hexagonal boron nitride on dielectric surfaces by diffusion and segregation mechanism,” *2D Mater.*, vol. 4, p. 025052, Mar. 2017, doi: 10.1088/2053-1583/aa6562.

[253] K. Ahmed, R. Dahal, A. Weltz, J.-Q. Lu, Y. Danon, and I. B. Bhat, “Growth of hexagonal boron nitride on (111) Si for deep UV photonics and thermal neutron detection,” *Appl. Phys. Lett.*, vol. 109, no. 11, p. 113501, Sep. 2016, doi: 10.1063/1.4962831.

[254] Y. Shi *et al.*, “Synthesis of Few-Layer Hexagonal Boron Nitride Thin Film by Chemical Vapor Deposition,” *Nano Lett.*, vol. 10, no. 10, pp. 4134–4139, Oct. 2010, doi: 10.1021/nl1023707.

[255] C. L. Tsai, Y. Kobayashi, T. Akasaka, and M. Kasu, “Molecular beam epitaxial growth of hexagonal boron nitride on Ni(1 1 1) substrate,” *J. Cryst. Growth*, vol. 311, no. 10, pp. 3054–3057, May 2009, doi: 10.1016/j.jcrysgro.2009.01.077.

[256] Y.-J. Cho *et al.*, “Hexagonal Boron Nitride Tunnel Barriers Grown on Graphite by High Temperature Molecular Beam Epitaxy,” *Sci. Rep.*, vol. 6, p. 34474, Sep. 2016, doi: 10.1038/srep34474.

[257] T. Q. P. Vuong *et al.*, “Deep ultraviolet emission in hexagonal boron nitride grown by high-temperature molecular beam epitaxy,” *2D Mater.*, vol. 4, no. 2, p. 021023, 2017, doi: 10.1088/2053-1583/aa604a.

[258] S. Nakhaie *et al.*, “Synthesis of atomically thin hexagonal boron nitride films on nickel foils by molecular beam epitaxy,” *Appl. Phys. Lett.*, vol. 106, no. 21, p. 213108, May 2015, doi: 10.1063/1.4921921.

[259] A.-R. Jang *et al.*, “Wafer-Scale and Wrinkle-Free Epitaxial Growth of Single-Orientated Multilayer Hexagonal Boron Nitride on Sapphire,” *Nano Lett.*, vol. 16, no. 5, pp. 3360–3366, May 2016, doi: 10.1021/acs.nanolett.6b01051.

[260] Y. Kobayashi, C.-L. Tsai, and T. Akasaka, “Optical band gap of h-BN epitaxial film grown on c -plane sapphire substrate,” *Phys. Status Solidi C*, vol. 7, no. 7–8, pp. 1906–1908, Jul. 2010, doi: 10.1002/pssc.200983598.

[261] F. Mahvash, S. Eissa, T. Bordjiba, A. C. Tavares, T. Szkopek, and M. Siaj, “Corrosion resistance of monolayer hexagonal boron nitride on copper,” *Sci. Rep.*, vol. 7, p. 42139, Feb. 2017, doi: 10.1038/srep42139.

[262] K. K. Kim *et al.*, “Synthesis of Monolayer Hexagonal Boron Nitride on Cu Foil Using Chemical Vapor Deposition,” *Nano Lett.*, vol. 12, no. 1, pp. 161–166, Jan. 2012, doi: 10.1021/nl203249a.

[263] J.-H. Park *et al.*, “Large-Area Monolayer Hexagonal Boron Nitride on Pt Foil,” *ACS Nano*, vol. 8, no. 8, pp. 8520–8528, Aug. 2014, doi: 10.1021/nn503140y.

[264] A. A. Tonkikh *et al.*, “Structural and electronic properties of epitaxial multilayer h-BN on Ni(111) for spintronics applications,” *Sci. Rep.*, vol. 6, p. 23547, Mar. 2016, doi: 10.1038/srep23547.

[265] H. Wang *et al.*, “Synthesis of Large-Sized Single-Crystal Hexagonal Boron Nitride Domains on Nickel Foils by Ion Beam Sputtering Deposition,” *Adv. Mater.*, vol. 27, no. 48, pp. 8109–8115, Dec. 2015, doi: 10.1002/adma.201504042.

[266] W. Auwärter, H. U. Suter, H. Sachdev, and T. Greber, “Synthesis of One Monolayer of Hexagonal Boron Nitride on Ni(111) from B-Trichloroborazine (ClBNH)3,” *Chem. Mater.*, vol. 16, no. 2, pp. 343–345, Jan. 2004, doi: 10.1021/cm034805s.

[267] A. Preobrajenski, A. Vinogradov, and N. Mårtensson, “Monolayer of h-BN chemisorbed on Cu(111) and Ni(111): The role of the transition metal 3d states,” *Surf. Sci.*, vol. 582, pp. 21–30, May 2005, doi: 10.1016/j.susc.2005.02.047.

[268] J. M. Rondinelli and E. Kioupakis, “Predicting and Designing Optical Properties of Inorganic Materials,” *Annu. Rev. Mater. Res.*, vol. 45, no. 1, pp. 491–518, Jul. 2015, doi: 10.1146/annurev-matsci-070214-021150.

[269] K. Ahmed, R. Dahal, A. Weltz, J. J.-Q. Lu, Y. Danon, and I. B. Bhat, “Effects of sapphire nitridation and growth temperature on the epitaxial growth of hexagonal boron nitride on sapphire,” *Mater. Res. Express*, vol. 4, no. 1, p. 015007, 2017, doi: 10.1088/2053-1591/aa54d5.

[270] F. Tang, T. Parker, G.-C. Wang, and T.-M. Lu, “Surface texture evolution of polycrystalline and nanostructured films: RHEED surface pole figure analysis,” *J. Phys. Appl. Phys.*, vol. 40, no. 23, p. R427, 2007, doi: 10.1088/0022-3727/40/23/R01.

[271] Z. Xu, H. Tian, A. Khanaki, R. Zheng, M. Suja, and J. Liu, “Large-area growth of multi-layer hexagonal boron nitride on polished cobalt foils by plasma-assisted molecular beam epitaxy,” *Sci. Rep.*, vol. 7, p. 43100, Feb. 2017, doi: 10.1038/srep43100.

[272] G. Lu *et al.*, “Synthesis of large single-crystal hexagonal boron nitride grains on Cu–Ni alloy,” *Nat. Commun.*, vol. 6, p. 6160, Jan. 2015, doi: 10.1038/ncomms7160.

[273] L. Song *et al.*, “Large Scale Growth and Characterization of Atomic Hexagonal Boron Nitride Layers,” *Nano Lett.*, vol. 10, no. 8, pp. 3209–3215, Aug. 2010, doi: 10.1021/nl1022139.

[274] Z. Liu *et al.*, “Ultrathin high-temperature oxidation-resistant coatings of hexagonal boron nitride,” *Nat. Commun.*, vol. 4, p. 2541, Oct. 2013, doi: 10.1038/ncomms3541.

[275] I. Stenger *et al.*, “Low frequency Raman spectroscopy of few-atomic-layer thick hBN crystals,” *2D Mater.*, vol. 4, no. 3, p. 031003, 2017, doi: 10.1088/2053-1583/aa77d4.

[276] R. V. Gorbachev *et al.*, “Hunting for Monolayer Boron Nitride: Optical and Raman Signatures,” *Small*, vol. 7, no. 4, pp. 465–468, Feb. 2011, doi: 10.1002/smll.201001628.

[277] S. Reich, A. C. Ferrari, R. Arenal, A. Loiseau, I. Bello, and J. Robertson, “Resonant Raman scattering in cubic and hexagonal boron nitride,” *Phys. Rev. B*, vol. 71, no. 20, p. 205201, May 2005, doi: 10.1103/PhysRevB.71.205201.

[278] I. Boulares, G. Shi, E. Kioupakis, P. Lošťák, C. Uher, and R. Merlin, “Surface phonons in the topological insulators Bi2Se3 and Bi2Te3,” *Solid State Commun.*, vol. 271, pp. 1–5, Mar. 2018, doi: 10.1016/j.ssc.2017.12.012.

[279] J. Serrano *et al.*, “Vibrational Properties of Hexagonal Boron Nitride: Inelastic X-Ray Scattering and Ab Initio Calculations,” *Phys. Rev. Lett.*, vol. 98, no. 9, p. 095503, Mar. 2007, doi: 10.1103/PhysRevLett.98.095503.

[280] J. Meng *et al.*, “Aligned Growth of Millimeter-Size Hexagonal Boron Nitride Single-Crystal Domains on Epitaxial Nickel Thin Film,” *Small*, vol. 13, no. 18, p. n/a-n/a, May 2017, doi: 10.1002/smll.201604179.

[281] T. Q. P. Vuong *et al.*, “Phonon symmetries in hexagonal boron nitride probed by incoherent light emission,” *2D Mater.*, vol. 4, no. 1, p. 011004, 2017, doi: 10.1088/2053-1583/4/1/011004.

[282] S. Baroni, S. de Gironcoli, A. Dal Corso, and P. Giannozzi, “Phonons and related crystal properties from density-functional perturbation theory,” *Rev. Mod. Phys.*, vol. 73, no. 2, pp. 515–562, Jul. 2001, doi: 10.1103/RevModPhys.73.515.

[283] P. Giannozzi *et al.*, “QUANTUM ESPRESSO: a modular and open-source software project for quantum simulations of materials,” *J. Phys. Condens. Matter*, vol. 21, no. 39, p. 395502, 2009, doi: 10.1088/0953-8984/21/39/395502.

[284] J. Deslippe, G. Samsonidze, D. A. Strubbe, M. Jain, M. L. Cohen, and S. G. Louie, “BerkeleyGW: A massively parallel computer package for the calculation of the quasiparticle and optical properties of materials and nanostructures,” *Comput. Phys. Commun.*, vol. 183, no. 6, pp. 1269–1289, Jun. 2012, doi: 10.1016/j.cpc.2011.12.006.

[285] N. Marzari, A. A. Mostofi, J. R. Yates, I. Souza, and D. Vanderbilt, “Maximally localized Wannier functions: Theory and applications,” *Rev. Mod. Phys.*, vol. 84, no. 4, pp. 1419–1475, Oct. 2012, doi: 10.1103/RevModPhys.84.1419.

[286] A. A. Mostofi, J. R. Yates, Y.-S. Lee, I. Souza, D. Vanderbilt, and N. Marzari, “wannier90: A tool for obtaining maximally-localised Wannier functions,” *Comput. Phys. Commun.*, vol. 178, no. 9, pp. 685–699, May 2008, doi: 10.1016/j.cpc.2007.11.016.

[287] J. Noffsinger, E. Kioupakis, C. G. Van de Walle, S. G. Louie, and M. L. Cohen, "Phonon-Assisted Optical Absorption in Silicon from First Principles," *Phys. Rev. Lett.*, vol. 108, no. 16, p. 167402, Apr. 2012, doi: 10.1103/PhysRevLett.108.167402.

[288] G. Shi and E. Kioupakis, "Electronic and Optical Properties of Nanoporous Silicon for Solar-Cell Applications," *ACS Photonics*, vol. 2, no. 2, pp. 208–215, Feb. 2015, doi: 10.1021/ph5002999.

[289] J. D. Caldwell, I. Aharonovich, G. Cassabois, J. H. Edgar, B. Gil, and D. N. Basov, "Photonics with hexagonal boron nitride," *Nat. Rev. Mater.*, vol. 4, no. 8, pp. 552–567, Aug. 2019, doi: 10.1038/s41578-019-0124-1.

[290] M. Han *et al.*, "Characteristics of aluminum nitride films on hexagonal boron nitride buffer layers using various growth methods through metal organic chemical vapor deposition," *J. Cryst. Growth*, vol. 507, pp. 316–320, Feb. 2019, doi: 10.1016/j.jcrysgro.2018.09.018.

[291] D. T. Thanh *et al.*, "Hexagonal boron nitride pattern embedded in AlN template layer for visible-blind ultraviolet photodetectors," *Opt. Mater. Express*, vol. 7, no. 5, pp. 1463–1472, May 2017, doi: 10.1364/OME.7.001463.

[292] W. Auwärter, "Hexagonal boron nitride monolayers on metal supports: Versatile templates for atoms, molecules and nanostructures," *Surf. Sci. Rep.*, vol. 74, no. 1, pp. 1–95, Mar. 2019, doi: 10.1016/j.surfrep.2018.10.001.

[293] L. Weston, D. Wickramaratne, and C. G. Van de Walle, "Hole polarons and \$p\$-type doping in boron nitride polymorphs," *Phys. Rev. B*, vol. 96, no. 10, p. 100102, Sep. 2017, doi: 10.1103/PhysRevB.96.100102.

[294] Y. Sun *et al.*, "Ultrahigh Q microring resonators using a single-crystal aluminum-nitride-on-sapphire platform," *Opt. Lett.*, vol. 44, no. 23, pp. 5679–5682, Dec. 2019, doi: 10.1364/OL.44.005679.

[295] X. Liu *et al.*, "Charge carrier transport properties of Mg-doped Al0.6Ga0.4N grown by molecular beam epitaxy," *Semicond. Sci. Technol.*, vol. 33, no. 8, p. 085005, Jul. 2018, doi: 10.1088/1361-6641/aace97.

[296] E. Cannuccia, B. Monserrat, and C. Attaccalite, "Theory of phonon-assisted luminescence in solids: Application to hexagonal boron nitride," *Phys. Rev. B*, vol. 99, no. 8, p. 081109, Feb. 2019, doi: 10.1103/PhysRevB.99.081109.

[297] L. Museur and A. Kanaev, "Near band-gap photoluminescence properties of hexagonal boron nitride," *J. Appl. Phys.*, vol. 103, no. 10, p. 103520, May 2008, doi: 10.1063/1.2925685.

[298] M. G. Silly *et al.*, "Luminescence properties of hexagonal boron nitride: Cathodoluminescence and photoluminescence spectroscopy measurements," *Phys. Rev. B*, vol. 75, no. 8, p. 085205, Feb. 2007, doi: 10.1103/PhysRevB.75.085205.

[299] P. Jaffrennou, J. Barjon, J.-S. Lauret, B. Attal-Trétout, F. Ducastelle, and A. Loiseau, "Origin of the excitonic recombinations in hexagonal boron nitride by spatially resolved cathodoluminescence spectroscopy," *J. Appl. Phys.*, vol. 102, pp. 116102-116102–3, Dec. 2007, doi: 10.1063/1.2821413.

[300] B. Arnaud, S. Lebègue, P. Rabiller, and M. Alouani, "Huge Excitonic Effects in Layered Hexagonal Boron Nitride," *Phys. Rev. Lett.*, vol. 96, no. 2, p. 026402, Jan. 2006, doi: 10.1103/PhysRevLett.96.026402.

[301] L. Sponza, H. Amara, F. Ducastelle, A. Loiseau, and C. Attaccalite, "Exciton interference in hexagonal boron nitride," *Phys. Rev. B*, vol. 97, no. 7, p. 075121, Feb. 2018, doi: 10.1103/PhysRevB.97.075121.

[302] L. Sponza *et al.*, "Direct and indirect excitons in boron nitride polymorphs: A story of atomic configuration and electronic correlation," *Phys. Rev. B*, vol. 98, no. 12, p. 125206, Sep. 2018, doi: 10.1103/PhysRevB.98.125206.

[303] C. Chen *et al.*, "Emergence of Interfacial Polarons from Electron–Phonon Coupling in Graphene/h-BN van der Waals Heterostructures," *Nano Lett.*, vol. 18, no. 2, pp. 1082–1087, Feb. 2018, doi: 10.1021/acs.nanolett.7b04604.

[304] P.-F. Li and Z.-W. Wang, "Optical absorption of Fröhlich polaron in monolayer transition metal dichalcogenides," *J. Appl. Phys.*, vol. 123, no. 20, p. 204308, May 2018, doi: 10.1063/1.5030678.

[305] L. Wang *et al.*, "Epitaxial growth of a 100-square-centimetre single-crystal hexagonal boron nitride monolayer on copper," *Nature*, vol. 570, no. 7759, p. 91, Jun. 2019, doi: 10.1038/s41586-019-1226-z.

[306] J. S. Lee *et al.*, "Wafer-scale single-crystal hexagonal boron nitride film via self-collimated grain formation," *Science*, vol. 362, no. 6416, pp. 817–821, Nov. 2018, doi: 10.1126/science.aau2132.

[307] T.-A. Chen *et al.*, "Wafer-scale single-crystal hexagonal boron nitride monolayers on Cu (111)," *Nature*, vol. 579, no. 7798, pp. 219–223, Mar. 2020, doi: 10.1038/s41586-020-2009-2.

[308] J. Kim *et al.*, "Principle of direct van der Waals epitaxy of single-crystalline films on epitaxial graphene," *Nat. Commun.*, vol. 5, no. 1, pp. 1–7, Sep. 2014, doi: 10.1038/ncomms5836.

[309] N. Nepal *et al.*, “Epitaxial Growth of III–Nitride/Graphene Heterostructures for Electronic Devices,” *Appl. Phys. Express*, vol. 6, no. 6, p. 061003, Jun. 2013, doi: 10.7567/APEX.6.061003.

[310] Y. Kobayashi, K. Kumakura, T. Akasaka, and T. Makimoto, “Layered boron nitride as a release layer for mechanical transfer of GaN-based devices,” *Nature*, vol. 484, no. 7393, pp. 223–227, Apr. 2012, doi: 10.1038/nature10970.

[311] K. Chung, H. Oh, J. Jo, K. Lee, M. Kim, and G.-C. Yi, “Transferable single-crystal GaN thin films grown on chemical vapor-deposited hexagonal BN sheets,” *NPG Asia Mater.*, vol. 9, no. 7, pp. e410–e410, Jul. 2017, doi: 10.1038/am.2017.118.

[312] S. Gautier *et al.*, “MOVPE growth study of BxGa(1−x)N on GaN template substrate,” *Superlattices Microstruct.*, vol. 40, no. 4–6, pp. 233–238, Oct. 2006, doi: 10.1016/j.spmi.2006.09.021.

[313] S. Azzi, A. Zaoui, and M. Ferhat, “On the importance of the band gap bowing in Boron-based III–V ternary alloys,” *Solid State Commun.*, vol. 144, no. 5–6, pp. 245–248, Nov. 2007, doi: 10.1016/j.ssc.2007.08.017.

[314] X. Li *et al.*, “BAlN thin layers for deep UV applications,” *Phys. Status Solidi A*, vol. 212, no. 4, pp. 745–750, Apr. 2015, doi: 10.1002/pssa.201400199.

[315] T. Takano, M. Kurimoto, J. Yamamoto, and H. Kawanishi, “Epitaxial growth of high quality BAlGaN quaternary lattice matched to AlN on 6H–SiC substrate by LP-MOVPE for deep-UV emission,” *J. Cryst. Growth*, vol. 237–239, Part 2, pp. 972–977, Apr. 2002, doi: 10.1016/S0022-0248(01)02026-7.

[316] A. Haider, S. Kizir, C. Ozgit-Akgun, A. K. Okyay, and N. Biyikli, “Low-temperature sequential pulsed chemical vapor deposition of ternary BxGa1-xN and BxIn1-xN thin film alloys,” *J. Vac. Sci. Technol. A*, vol. 34, no. 1, p. 01A123, Jan. 2016, doi: 10.1116/1.4936072.

[317] S. H. Park and D. Ahn, “Theoretical Studies on TM-Polarized Light Emission for Ultraviolet BAlGaN/AlN Optoelectronic Devices,” *IEEE Photonics Technol. Lett.*, vol. 28, no. 20, pp. 2153–2155, Oct. 2016, doi: 10.1109/LPT.2016.2585497.

[318] G. Orsal *et al.*, “Effect of boron incorporation on growth behavior of BGaN/GaN by MOVPE,” *J. Cryst. Growth*, vol. 310, pp. 5058–5062, Nov. 2008, doi: 10.1016/j.jcrysgro.2008.08.024.

[319] R. Cusco, E. Alarcon-Llado, J. Ibanez, L. Artus, S. Gautier, and A. Ougazzaden, “Phonons in BxGa1-xN/GaN epilayers studied by means of UV Raman scattering,” *Phys. Status Solidi B Basic Res.*, vol. 245, no. 4, pp. 731–734, 2008.

[320] T. Akasaka, Y. Kobayashi, and T. Makimoto, “BGaN micro-islands as novel buffers for growth of high-quality GaN on sapphire,” *J. Cryst. Growth*, vol. 298, pp. 320–324, Jan. 2007, doi: 10.1016/j.jcrysgro.2006.10.033.

[321] L. Williams and E. Kioupakis, “BAlGaN alloys nearly lattice-matched to AlN for efficient UV LEDs,” *Appl. Phys. Lett.*, vol. 115, no. 23, p. 231103, Dec. 2019, doi: 10.1063/1.5129387.

[322] X. Z. Du, J. Li, J. Y. Lin, and H. X. Jiang, “The origin of deep-level impurity transitions in hexagonal boron nitride,” *Appl. Phys. Lett.*, vol. 106, no. 2, p. 021110, Jan. 2015, doi: 10.1063/1.4905908.